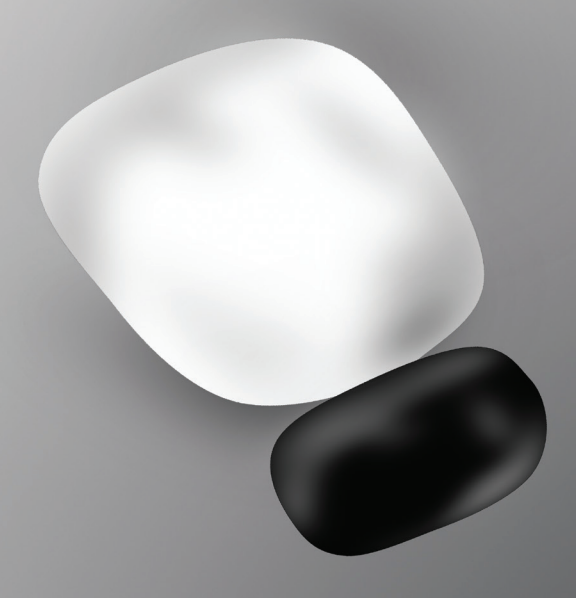
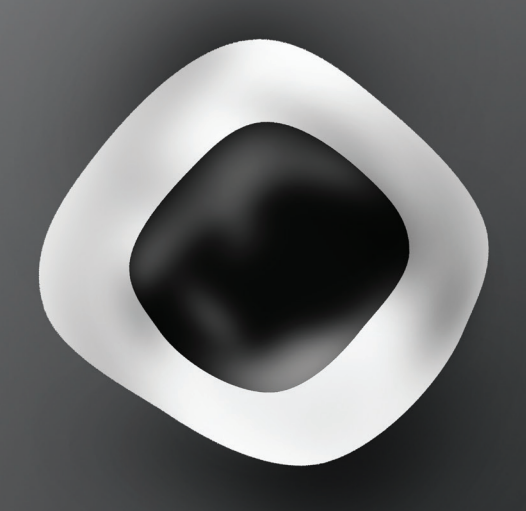


Heteronanocrystal Transformations through *In-situ* Transmission Electron Microscopy



Anıl Ozan Yalçın



Invitation

to the public defence of PhD dissertation

Heteronanocrystal
Transformations
through *In-situ* TEM

by

Anıl Ozan Yalçın

on

28 September 2015 at 10:00
in the Senaatszaal
Aula Congress Centre
Delft University of Technology
(Mekelweg 5, Delft)



Brief presentation at 09:30



Heteronanocrystal Transformations through In-situ Transmission Electron Microscopy

Anıl Ozan Yalçın

Heteronanocrystal Transformations through In-situ Transmission Electron Microscopy

Proefschrift

ter verkrijging van de graad van doctor aan de Technische Universiteit Delft, op gezag van de Rector Magnificus prof. ir. K. Ch. A. M. Luyben; voorzitter van het College voor Promoties, in het openbaar te verdedigen op 28 september 2015 om 10:00 uur

door

Anıl Ozan YALÇIN

Ir. Scheikundige Technologie, Technische Universiteit Eindhoven, Nederland

Geboren te Gediz, Turkije

This dissertation has been approved by the promotor:

Prof. dr. H. W. Zandbergen

Composition of the doctoral committee:

Rector Magnificus chairman

Prof. dr. H. W. Zandbergen Technische Universiteit Delft, promotor

Dr. ir. M. A. van Huis Universiteit Utrecht

Dr. ir. F. D. Tichelaar Technische Universiteit Delft

Independent members:

Prof. dr. S. Bals Universiteit Antwerpen Prof. dr. A. van Blaaderen Universiteit Utrecht

Prof. dr. ir. T. J. H. Vlugt Technische Universiteit Delft Technische Universiteit Delft Prof. dr. L. D. A. Siebbeles

Prof. dr. J. Dik Technische Universiteit Delft, reserve member

Anıl Ozan Yalçın

Heteronanocrystal Transformations through *In-situ* Transmission Electron Microscopy

Keywords: In-situ Transmission Electron Microscopy,

Heteronanocrystals, Thermal Evolution







This work is part of the research programme of the Foundation for Fundamental Research on Matter (FOM), which is part of the Netherlands Organization for Scientific Research (NWO).

Casimir PhD Series, Delft-Leiden 2015-12 ISBN 978-90-8593-220-8 Copyright © 2015 by Anıl Ozan Yalçın Author e-mail: anilozan@gmail.com

Printed by Gildeprint Cover design by Oleksandra Ivashchenko

An electronic version of this dissertation is available at http://repository.tudelft.nl/

To my family Aileme

CONTENTS

1.	In-si	tu thermal annealing of nanostructures	13		
	1.1	Introduction	14		
	1.2	Materials in nanoscale	14		
	1.3	Heat treatment on NCs and HNCs	15		
	1.4	In-situ heating studies of NCs and HNCs via TEM	16		
	Refer	rences	20		
	Thesi	is outline	23		
2.	Experimental techniques				
	2.1	Transmission Electron Microscopy (TEM)	26		
	2.2	TEM specimen holder for <i>in-situ</i> heating experiments	27		
	2.3	Elemental analysis	28		
		2.3.1 Energy Dispersive X-ray Spectroscopy (EDX)	28		
		2.3.2 Electron Energy Loss Spectroscopy (EELS) and			
		Energy Filtered TEM (EFTEM)	31		
	Refer	rences	35		
3.	Zn inner diffusion in CdSe-CdS-ZnS core-multishell system				
	Abstr	ract	37		
	3.1	Introduction	39		
	3.2	Methods	39		
	3.3	Results & Discussion	40		
	3.4	Conclusions			
	References				
	Appendix A				
	A.1	CdSe-CdS-ZnS core-multishell QD synthesis method	49		
	A.2	A.2 Additional Chemi-STEM maps and elemental quantifications			
	References				

4.	Core	Core-shell reconfiguration in				
	Fe _x O/CoFe ₂ O ₄ core/shell system					
	Absti	ract	55			
	4.1	Introduction	57			
	4.2	Methods	58			
		4.2.1 Synthesis of spherical and cubic NCs	58			
		4.2.2 In-situ TEM studies	59			
	4.3	Results	60			
	4.4	Discussion	60			
	4.5	Conclusions	68			
	Refer	rences	69			
	Appe	endix B	71			
5.	Catio	on exchange and solid–solid–vapor (SSV) growth in				
	CdSe	CdSe-PbSe dumbbell system				
	Absti	ract	75			
	5.1	Introduction	77			
	5.2	Results & Discussion	77			
	5.3	Conclusions	84			
	5.4					
	Refer	References				
	Appe	endix C	89			
	C.1	Schematic of the atomistic growth mechanism	89			
	C.2	Synthesis of the PbSe-CdSe nanodumbbells	89			
	C.3	Quantitative results of STEM-EDX elemental maps	9			
	C.4	Force-field MD simulations	91			
		C.4.1 Force field for the Pb-Se-Cd system	91			
		C.4.2 Model construction for the PbSe-CdSe nanodumbbells	93			
		C.4.3 Molecular dynamics simulations results for Model 1, 2, an	d 4 90			
	C.5	Density Functional Theory (DFT) calculations	99			
		C.5.1 Defect energy calculations in PbSe and CdSe	99			
		C.5.2 Energies of PbSe-CdSe mixed phases	10			
	Refer	rences	104			
	Publications					
	Conference presentations					
	Conf	ference posters	100			
	Ackn	nowledgments	107			
	Curr	riculum vitae	109			

SUMMARY

Synthesis of nanocrystals (NCs) and heteronanocrystals (HNCs) has developed very fast particularly in the last decade. Nowadays, various structures and different morphologies of NCs and HNCs can be prepared with a very narrow size distribution. The nanoscale dimensions of these crystals lead to interesting phenomena (e.g. electronic properties) that are not found in their bulk counterparts. Therefore, NC and HNC research is now a hot topic in materials science and applied physics.

Despite having interesting properties, the stability of NCs and HNCs is an issue outside the solution in which they are suspended. This raises a concern for their potential applications. Regarding their thermal stability, a number of studies have been reported showing morphological as well as chemical transformations with changing temperature. In this thesis, the focus is on in-situ heat induced transformations of HNCs and detailed characterization of these transformations through advanced transmission electron microscopy (TEM) techniques.

Two processes were observed through in-situ heat treatment of the CdSe-CdS-ZnS coremultishell system: diffusion and simultaneous evaporation of different species. The structure evolves into a $Cd_xZn_{1-x}Se-Cd_yZn_{1-y}S$ core-shell system through Zn inner diffusion and simultaneous partial evaporation of Cd and S.

A more complex transformation is a temperature induced reconfiguration in the Fe₂O/CoFe₂O₄ core/shell system. In this case, the Fe_xO diffuses out of the core location and segregates at the outside of the CoFe₂O₄ shell. At the same time, the CoFe₂O₄ shell shrinks and fills the core volume. Co diffusion into the Fe_xO structure is also observed with heating.

Furthermore, in-situ heating studies of the CdSe-PbSe dumbbell system (a CdSe nanorod with PbSe NC tips) have shown a novel epitaxial nanowire growth process. Upon heating, PbSe starts to grow into CdSe with simultaneous Cd evaporation. This process proceeds as a cation exchange mechanism, whereby Pb is replacing Cd in CdSe. The crystal structure changes epitaxially at the same time from hexagonal wurtzite (CdSe) to cubic rock-salt (PbSe). Considering that the initial phases of CdSe and PbSe domains are solid and the final evaporation of Cd into the vapor phase, this novel epitaxial growth process is named solid-solid-vapor (SSV) growth.

Observations reported in this thesis clearly show that transformations of HNCs upon heat treatment can differ significantly from one another. These studies can be regarded as first reference points when these HNC systems are considered to be implemented in possible future applications and for future in-situ heat treatment studies of HNCs.

SAMENVATTING

De vervaardiging van nanokristallen (NKen) en heteronanokristallen (HNKen) heeft zich in het laatste decennium versneld ontwikkeld. Tegenwoordig kunnen deze deeltjes met verschillende structuren en morfologieën en een smalle grootteverdeling gemaakt worden, met interessante (bv. elektronische) eigenschappen die niet bestaan in bulk materiaal. Dit maakt het onderzoek naar NKen en HNKen een "hot topic" in het hedendaags materiaalkundig en toegepast fysisch onderzoek.

Het gebrek aan stabiliteit van NKen en HNKen eenmaal uit de vloeistof waarin ze gemaakt zijn, staat potentiële toepassingen mogelijkerwijs nog in de weg. Wat betreft de thermische stabiliteit zijn een aantal studies gepubliceerd waarin zowel morfologische als chemische transformaties met veranderende temperatuur zijn gerapporteerd. In dit proefschrift ligt de nadruk op insitu verhittingsexperimenten van HNKen en de gedetailleerde karakterisatie van de daarmee gepaard gaande transformaties, met geavanceerde transmissie-elektronenmicroscoop (TEM) technieken.

Tijdens TEM in-situ verhittingsexperimenten van het CdSe-CdS-ZnS kern-multischil systeem werden twee processen waargenomen: diffusie en gelijktijdige verdamping van verschillende atoomsoorten. De structuur ontwikkeld zich naar een Cd_xZn_{1-x}Se-Cd_yZn_{1-y}S kern-schil systeem via diffusie van Zn binnen de structuur en gelijktijdige gedeeltelijke verdamping van Cd en S.

Een meer complexe transformatie is de temperatuur geïnduceerde reconfiguratie binnen het Fe,O/CoFe,O₄ kern/schil systeem. In dit geval diffundeert het Fe,O vanuit de kern naar de buitenkant van de CoFe₂O₄ schil. Tegelijkertijd verschrompelt de CoFe₂O₄ schil en vult zo de kern. Co diffusie in de Fe_xO kern is ook waargenomen tijdens verhitting.

Vervolgens lieten in-situ verhittingsexperimenten van het CdSe-PbSe halter systeem (een CdSe nanostaaf met PbSe NK uiteinden) een nieuw epitaxiaal nanodraad groeiproces zien: tijdens verhitting groeit het PbSe in de CdSe nanostaaf met gelijktijdige Cd verdamping. Dit proces vindt plaats als een kation verwisselmechanisme met vervanging van Cd door Pb in CdSe. Tegelijkertijd verandert de kristalstructuur epitaxiaal van hexagonaal wurtziet (CdSe) naar kubisch steenzout (PbSe). Dit nieuwe groeiproces wordt ook wel VVD (vast-vast-damp) groei genoemd, gezien het feit dat in het begin twee vaste fasen CdSe en PbSe bestaan en er uiteindelijk Cd verdampt.

De verschijnselen zoals gerapporteerd in dit proefschrift laten duidelijk zien dat verhittings geïnduceerde transformaties van HNKen significant van elkaar kunnen verschillen. Deze studies kunnen zeer nuttig blijken wanneer de betreffende HNKen overwogen worden in toekomstige toepassingen en ook voor verdere in-situ verhittingsexperimenten van HNKen.

Chapter 1

In-situ thermal annealing of nanostructures

1.1 Introduction

The term "in-situ" derives from Latin with a literal meaning "in place".¹ One can now encounter many scientific studies in the field of applied physics and materials science, where researchers favour using "in-situ" to emphasize that the effect of a particular variable (temperature, gas atmosphere, radiation, etc.) on a specimen has been observed real time. This is of particular importance since in-situ studies give a solid evidence regarding the effect of specific variable on the studied specimen.

As many research areas (colloid science, band-gap engineering, catalysis, interface chemistry, etc.) now focus on nanoscale and even atomic scale, it is also of particular interest to conduct atomic resolution *in-situ* experiments. Transmission Electron Microscopy (TEM) with a wide range of imaging and spectroscopic techniques has been proven to be ideal for this sort investigations, ^{2,3} and incorporation of microelectronic mechanical system (MEMS) technology in the TEM specimen holder design provides minimal specimen drift, thus increasing the success of atomic resolution observations (details of TEM and application of MEMS technology in TEM specimen holder can be found in Chapter 2).⁴⁻⁶

1.2 Materials in nanoscale

By definition, a crystal domain of a material is referred as a nanocrystal (NC) when the size of that domain is not larger than nanometer (nm) range.^{7,8} Materials in NC state can exhibit different properties with respect to their bulk counterparts, making it possible to manipulate the intrinsic properties (such as thermal stability and optical band gap) by adjusting the size of domains. For instance, bulk Fe_xO (x = 0.83-0.95)^{9,10} crystal is stable only above 560 °C. Below this temperature, it decomposes into α-Fe₂O₃, γ-Fe₂O₃ and Fe₃O₄ domains, whereas Fe_xO NCs are stable at room temperature (RT).¹⁰⁻¹² In another example, CdS NCs with varying size of 3-8 nm can melt as low as 573 K, while the bulk melting temperature of CdS is 1678 K.¹³ Besides thermal stability, pressure stability of NC structures can also vary from their bulk counterparts. CdSe can transform reversibly from direct band gap hexagonal wurtzite crystal structure to indirect band gap cubic rock-salt structure upon application of pressure, though CdSe NCs can withstand two to three times higher pressures compared to bulk CdSe until this transformation takes place.^{14,15} Therefore, it can be concluded that bulk phase diagrams of certain materials lose their validity in nanoscale and it is required to construct new studies specifically for the NC state of these structures.^{16,17}

An important research field in nanoscale materials science is semiconductor NCs, better known as quantum dots (QDs). 18 QDs exhibit size dependent optical band gaps. As an example, whole visible spectrum can be covered by tuning the size of CdSe QDs, 19,20 and this makes CdSe QDs appealing for numerous applications such as light emitting diodes (LEDs) and biolabeling.²¹⁻²³

Heteronanocrystal (HNC) synthesis has opened new possibilities in nanoscience. HNCs consist of different nanostructure domains, and these domains are sometimes connected to each other through an interface. With advancements in colloidal synthesis methods, complex morphologies of HNCs can now be synthesized such as nanodumbbell HNCs,²⁴ core/shell HNCs, ^{25,26} tetrapod and octapod shaped HNCs, ²⁷ and binary HNC superlattices. ²⁸ HNCs can exhibit novel combined functional properties of the individual NC constituents and properties of HNCs can be manipulated through adjustments of NC domains.^{29,30} For instance, growing a CdSe shell on PbSe NCs through cation exchange (replacing Pb cations with Cd cations) decreases the size of PbSe domains while the overall structure size is retained. As a result of the changing PbSe NC domain size, the optical properties can be manipulated.²⁹ Moreover, HNC synthesis can be carried out in order to improve the properties of specific species. Coating PbSe NCs with CdSe and forming PbSe/CdSe core/shell HNCs was shown to prolong the air stability of PbSe core together with improved optical properties. ^{26,31}

1.3 Heat treatment on NCs and HNCs

Several studies have shown that properties of NCs and HNCs can be further manipulated through thermal annealing. When NCs and HNCs are considered to be implemented in a possible application, it is important to have a detailed understanding of their thermal stability.

Considering systems with a single NC type, it was reported that annealing PbSe and PbS QD assemblies at 170 °C decreased interparticle distance and as a result, the conductivity of the assemblies increased exponentially.³²

Regarding HNCs, in a study on temperature dependent optical properties of CdSe/ZnS core/ shell QDs,³³ the optical properties deteriorated at 315 K compared to that of at 100 K. The optical properties of CdSe/ZnS core/shell QDs in the similar temperature range (80 K to 300 K) could be enhanced by incorporation of CdS/CdZnS middle layer between CdSe and ZnS (thus overcoming the large lattice mismatch between CdSe and ZnS).³⁴ On the contrary, optical properties of a small lattice mismatch CdTe/CdSe HNCs were found to be improved when the structure was heated from 293 K to 383 K.³⁵ Therefore, it can be stated that each HNC system needs to be studied separately as a potential candidate for possible applications.

Besides optical properties, magnetic properties of HNCs can alter with heat treatment as well. The FePt-MgO binary HNC superlattice exhibits superparamagnetic behavior at room temperature (RT). Upon annealing in vacuum at 650 °C for 30 min and cooling to RT, the structure started to exhibit ferromagnetic behavior due to the phase transformation of FePt NCs into magnetically hard domains.³⁶

As NCs and HNCs are now a hot topic in nanoscience and there is a high demand on the incorporation of these systems in several applications, detailed nanoscale *in-situ* heating studies are crucial for thermal investigation of NC systems as well as HNCs. Number of HNC systems with changing temperature induced properties have been tested already in applications. For instance, annealing TiO₂/PbS NC based heterojunction solar cells at 150 °C led to intermixing (bulk heterojunction) of TiO₂ and PbS with improved carrier transport and energy conversion efficiency.³⁷

1.4 In-situ heating studies of NCs and HNCs via TEM

In-situ High Resolution Transmission Electron Microscopy (HRTEM) can shed light on thermal behavior of NCs. In this part, several *in-situ* heat treatment studies on NCs and HNCs are represented.

Figure 1.1 represents thermal evolution study of single Au NC domain heated from 415 °C to 450 °C,6 whereby the NC changed its morphology with changing temperature. In another study,38 Ag NCs underwent heat induced neck formation and sintering at 200 °C, shown in Figure 1.2.

Thermal stability investigation of HNCs through *in-situ* TEM is much more challenging as HNCs consist of different nanostructure domains. Thermal behavior of each individual NC domain can differ. Moreover, the interfaces between NC domains are generally unstable due to different structural properties of the constituent domains (e.g. lattice mismatch).^{20,39}

Number of *in-situ* heating studies of HNCs have appeared in the literature, in which interesting morphological and chemical transformations of various HNC systems have been shown. In one study,⁴⁰ thermal stability of CdSe-Au HNCs was investigated. CdSe-Au HNCs consisted of CdSe nanorods with Au NC domains along the surface of CdSe nanorods. This HNC system

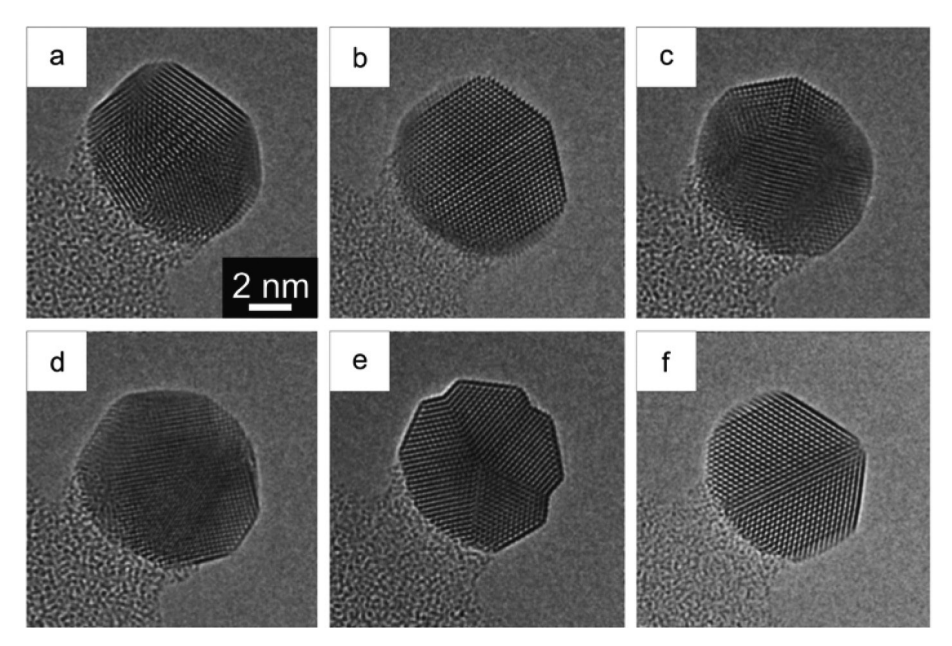


Figure 1.1. Bright Field TEM (BFTEM) images of Au NC during in-situ annealing at temperatures of (a-d) 415 °C and (e and f) 450 °C. The Au NC undergoes morphological and structural evolution with temperature. The scale bar in Figure 1.1a applies to all images. Reprinted from Ref. 6, Copyright 2010, with permission from Elsevier.

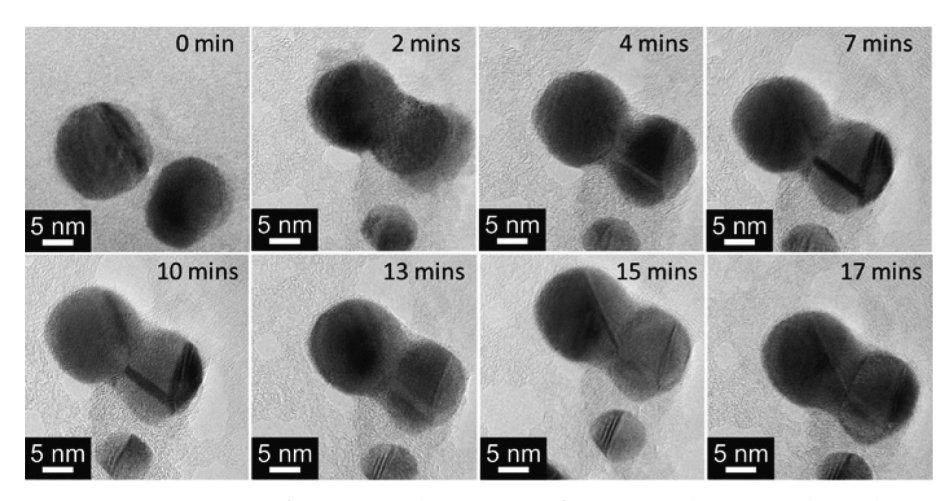


Figure 1.2. BFTEM images of Ag NCs undergoing neck formation and sintering observed in-situ at 200 °C. Darker contrasts on the NCs are twin boundaries. Reprinted from Ref. 38, Copyright 2014, with permission from Elsevier.

underwent a heat induced transformation at 200-250 °C whereby Au nanodomains migrated from lateral CdSe nanorod surfaces to the nanorod tips (Figure 1.3). With this study, it was concluded that the CdSe-Au semiconductor-metal interface quality can be enhanced by in-situ heat treatment on HNCs.

In another in-situ heating study,⁴¹ sandwich morphology CdSe/Cu₃P/CdSe HNC system transformed chemically to Cu₂Se NC domain with simultaneous evaporation of Cd and P at elevated temperatures (Figure 1.4). Note that the initial sandwich morphology was preserved after the transformation (Figure 1.4c).

In-situ heating can bring about more complex transformations with simultaneous chemical and morphological HNC evolution, exemplified with CdS-Au HNC system.⁴² Imaging and elemental map studies of the initial CdS-Au HNC system (Figure 1.5a) showed that the initial structure consisted of a CdS nanorod with Au tips, which was similar to the CdSe-Au HNCs (Figure 1.3). Despite initial morphological and structural similarities between these two systems, the thermal behavior of CdS-Au HNCs was observed to be totally different from CdSe-Au HNCs. Annealing CdS-Au HNCs at 200 °C initially led to breakage of CdS nanorods into smaller domains and formation of a Cd shell around Au NCs. Elemental map studies (Figure 1.5b) revealed that the structure in fact transformed chemically to AuS/Cd core/ shell HNCs.

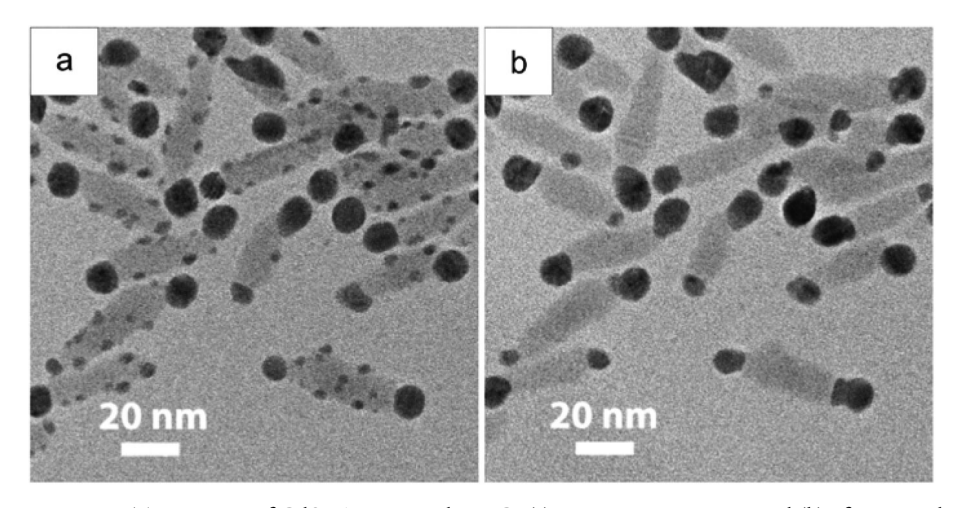


Figure 1.3. BFTEM image of CdSe-Au nanorod HNCs (a) at room temperature and (b) after annealing at 200-250 °C. The initial HNC consisted of CdSe nanorods (light contrast) and Au nanodomains (dark contrast) located along the lateral nanorod surfaces as well as at the tips. With annealing, Au domains migrated to the tips and the CdSe-Au semiconductor-metal interface quality was enhanced. Reprinted with permission from Ref. 40. Copyright 2010 American Chemical Society.

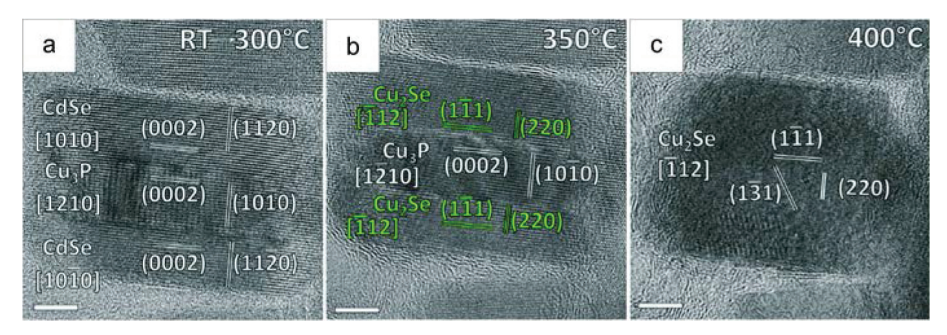


Figure 1.4. BFTEM images of CdSe/Cu₃P/CdSe HNC during *in-situ* thermal evolution (a) from room temperature to 300 °C, (b) at 350 °C and (c) 400 °C. CdSe/Cu₃P/CdSe HNC transformed to Cu₂Se NC together with simultaneous sublimation of Cd and P. All scale bars represent 5 nm. Reprinted with permission from Ref. 41. Copyright 2013 American Chemical Society.

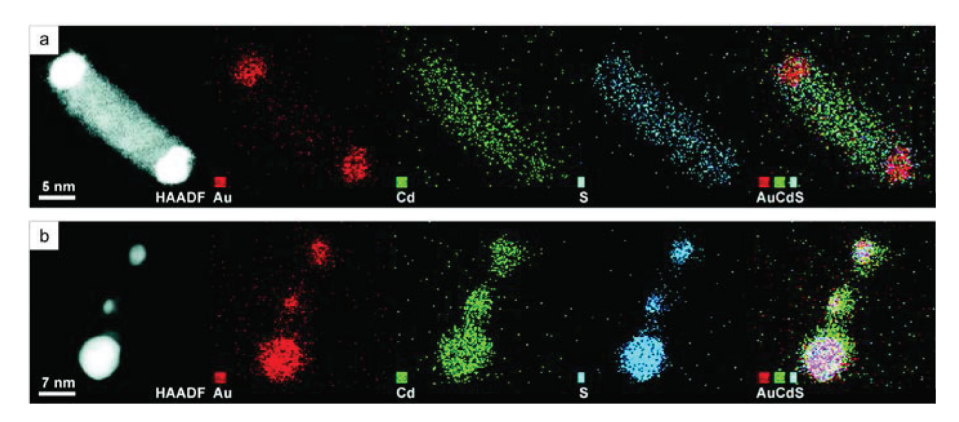


Figure 1.5. High Angle Annular Dark Field Scanning Transmission Electron Microscopy (HAADF-STEM) images of CdS-Au HNCs and corresponding Au, Cd and S elemental maps as well as the overlay of Cd, S and Au elemental maps. (a) The structure was CdS nanorod with Au tips before thermal annealing, (b) the initial structure evolved into smaller nanodomains with thermal annealing. Chemical transformation took place and the structure evolved into AuS/Cd core/shell HNCs. Reprinted with permission from Ref. 42. Copyright 2011 American Chemical Society.

When the varying behavior of nanodomains from their bulk counterparts and the scarce number of reported studies on the thermal stability of HNCs are taken into consideration, it is now evident that the nanoscience literature is lacking detailed in-situ heat treatment investigations on different HNC systems.

References

- Alberts, B.; Bray, D.; Hopkin, K.; Johnson, A.; Lewis, J.; Raff, M.; Roberts, K.; Walter, P. *Essential Cell Biology, Third Edition*; Garland Science: New York, 2010, pp 352.
- 2 Saka, H.; Kamino, T.; Arai, S.; Sasaki, K. MRS Bull. 2008, 33, 93-100.
- 3 Xu, T.; Sun, L. Small 2015, doi: 10.1002/smll.201403236.
- 4 van Huis, M. A.; Kunneman, L. T.; Overgaag, K.; Xu, Q.; Pandraud, G.; Zandbergen, H. W.; Vanmaekelbergh, D. *Nano Lett.* 2008, 8, 3959-3963.
- van Huis, M. A.; Young, N. P.; Pandraud, G.; Creemer, J. F.; Vanmaekelbergh, D.; Kirkland, A. I.; Zandbergen, H. W. *Adv. Mater.* 2009, 21, 4992-4995.
- 6 Young, N. P.; van Huis, M. A.; Zandbergen, H. W.; Xu, H.; Kirkland, A. I. *Ultramicroscopy* 2010, 110, 506-516.
- Houtepen, A. J. Charge injection and transport in quantum confined and disordered systems. Ph.D. Thesis, Utrecht University, June 2007.
- 8 Evers, W. H. Entropy driven and reaction driven self-assembly of colloidal semiconductor nanocrystals. Ph.D. Thesis, Utrecht University, November 2012.
- 9 Pichon, B. P.; Gerber, O.; Lefevre, C.; Florea, I.; Fleutot, S.; Baaziz, W.; Pauly, M.; Ohlmann, M.; Ulhaq, C.; Ersen, O.; Pierron-Bohnes, V.; Panissod, P.; Drillon, M.; Begin-Colin, S. *Chem. Mater.* 2011, 23, 2886-2900.
- 10 Bodnarchuk, M. I.; Kovalenko, M. V.; Groiss, H.; Resel, R.; Reissner, M.; Hesser, G.; Lechner, R. T.; Steiner, W.; Schäffler, F.; Heiss, W. *Small* 2009, 5, 2247-2252.
- 11 Glaria, A.; Kahn, M. L.; Chaudret, B.; Lecante, P.; Casanove, M. -J.; Barbara, B. *Mater. Chem. Phys.* 2011, 129, 605-610.
- 12 Yin, M.; Chen, Z.; Deegan, B.; O'Brien, S. J. Mater. Res. 2007, 22, 1987-1995.
- 13 Goldstein, A. N.; Echer, C. M.; Alivisatos, A. P. Science 1992, 256, 1425-1427.
- 14 Tolbert, S. H.; Alivisatos A. P. Science 1994, 265, 373-376.
- 15 Tolbert, S. H.; Herhold, A. B.; Johnson, C. S.; Alivisatos, A. P. *Phys. Rev. Lett.* 1994, 73, 3266-3269.
- Barnard, A. S.; Young, N. P.; Kirkland, A. I.; van Huis, M. A.; Xu, H. ACS Nano 2009, 3, 1431-1436.
- Baumgardner, W. J.; Yu, Y.; Hovden, R.; Honrao, S.; Hennig, R. G.; Abruña, H. D.; Muller, D.; Hanrath, T. ACS Nano 2014, 8, 5315-5322.
- 18 Yin, Y.; Alivisatos, A. P. *Nature* 2005, 437, 664-670.
- 19 Empedocles, S. A.; Bawendi, M. G. Science 1997, 278, 2114-2117.
- 20 Talapin, D. V.; Mekis, I.; Götzinger, S.; Kornowski, A.; Benson, O.; Weller, H. J. Phys. Chem. B 2004, 108, 18826-18831.
- 21 Samanta, A.; Deng, Z.; Liu, Y. Langmuir 2012, 28, 8205-8215.
- 22 Munro, A. M.; Ginger, D. S. Nano Lett. 2008, 8, 2585-2590.

- 23 Puzder, A.; Williamson, A. J.; Zaitseva, N.; Galli, G. Nano Lett. 2004, 4, 2361-2365.
- Kudera, S.; Carbone, L.; Casula, M. F.; Cingolani, R.; Falqui, A.; Snoeck, E.; Parak, W. I.; Manna, 24 L. Nano Lett. 2005, 5, 445-449.
- 25 Bals, S.; Casavola, M.; van Huis, M. A.; Van Aert, S.; Batenburg, K. J.; Van Tendeloo, G.; Vanmaekelbergh, D. Nano Lett. 2011, 11, 3420-3424.
- Casavola, M.; van Huis, M. A.; Bals, S.; Lambert, K.; Hens, Z.; Vanmaekelbergh, D. Chem. Mater. 26 2011, 24, 294-302.
- Deka, S.; Miszta, K.; Dorfs, D.; Genovese, A.; Bertoni, G.; Manna, L. Nano Lett. 2010, 10, 3770-27
- 28 Overgaag, K.; Evers, W.; de Nijs, B.; Koole, R.; Meeldijk, J.; Vanmaekelbergh, D. J. Am. Chem. Soc. 2008, 130, 7833-7835.
- 29 Grodzińska, D.; Evers, W. H.; Dorland, R.; van Rijssel, J.; van Huis, M. A.; Meijerink, A.; de Mello Donegá, C.; Vanmaekelbergh, D. Small 2011, 7, 3493-3501.
- Sciacca, B.; Mann, S. A.; Tichelaar, F. D.; Zandbergen, H. W.; van Huis, M. A.; Garnett, E. C. 30 Nano Lett. 2014, 14, 5891-5898.
- Sykora, M.; Koposov, A. Y.; McGuire, J. A.; Schulze, R. K.; Tretiak, O.; Pietryga, J. M.; Klimov, 31 V. I. ACS Nano 2010, 4, 2021-2034.
- 32 Baik, S. J.; Kim, K.; Lim, K. S.; Jung, S. M.; Park, Y. C.; Han, D. G.; Lim, S.; Yoo, S.; Jeong, S. J. Phys. Chem. C 2011, 115, 607-612.
- Walker, G. W.; Sundar, V. C.; Rudzinski, C. M.; Wun, A. W.; Bawendi, M. G.; Nocera, D. G. 33 Appl. Phys. Lett. 2003, 83, 3555-3557.
- Jing, P.; Zheng, J.; Ikezawa, M.; Liu, X.; Lv, S.; Kong, X.; Zhao, J.; Masumoto, Y. J. Phys. Chem. C 34 2009, 113, 13545-13550.
- 35 Chin, P. T. K.; de Mello Donegá, C.; van Bavel, S. S.; Meskers, S. C. J.; Sommerdijk, N. A. J. M.; Janssen, R. A. J. J. Am. Chem. Soc. 2007, 129, 14880-14886.
- Dong, A.; Chen, J.; Ye, X.; Kikkawa, J. M.; Murray, C. B. J. Am. Chem. Soc. 2011, 133, 13296-36 13299.
- 37 Ding, B.; Wang, Y.; Huang, P. -S.; Waldeck, D. H.; Lee, J. -K. J. Phys. Chem. C 2014, 118, 14749-14758.
- 38 Asoro, M. A.; Ferreira, P. J.; Kovar, D. Acta Mater. 2014, 81, 173-183.
- 39 Xie, R.; Kolb, U.; Li, J.; Basché, T.; Mews, A. J. Am. Chem. Soc. 2005, 127, 7480-7488.
- 40 Figuerola, A.; van Huis, M.; Zanella, M; Genovese, A.; Marras, S.; Falqui, A.; Zandbergen, H. W.; Roberto Cingolani, R.; Manna, L. Nano Lett. 2010, 10, 3028-3036.
- 41 De Trizio, L.; De Donato, F.; Casu, A.; Genovese, A.; Falqui, A.; Povia, M.; Manna, L. ACS Nano 2013, 7, 3997-4005.
- 42 van Huis, M. A.; Figuerola, A.; Fang, C.; Béché, A.; Zandbergen, H. W.; Manna, L. Nano Lett. 2011, 11, 4555-4561.

Thesis outline

This thesis is composed of a collection of case studies, introducing the reader to *in-situ* heating experiments conducted on various heteronanocrystal (HNC) systems by using advanced transmission electron microscopy (TEM) techniques. Chapter 1 is aimed to present a brief literature overview of *in-situ* heating experiments conducted on nanocrystals (NCs) and HNCs.

TEM is the core characterization tool used in this thesis, and two different TEM imaging techniques were employed in the in-situ studies presented here. These imaging techniques, namely Bright Field TEM (BFTEM) and High Angle Annular Dark Field Scanning Transmission Electron Microscopy (HAADF-STEM) are introduced in Chapter 2. In addition, microelectronic mechanical system (MEMS) based micro-hotplate (where colloidal HNCs are deposited) and the TEM specimen holder used for *in-situ* heating investigations are introduced in this chapter. Elemental studies were conducted through Energy Dispersive X-ray Spectroscopy (EDX) and Electron Energy Loss Spectroscopy (EELS), both of which are explained in this chapter as well. These techniques can provide spectroscopic imaging, in other words elemental maps (such as Energy Filtered TEM, known as EFTEM) and they are also explained with examples.

From Chapter 3 to Chapter 5, three different in-situ heating studies on three different HNC systems are presented. More details on the HNCs such as synthesis methods, quantitative elemental characterization studies, additional images and further details can be found in the appendices (Appendix A, B and C) following each chapter. Note that in-situ thermal evolutions of HNCs in these chapters are ordered from basic to more advanced.

Chapter 3 presents an *in-situ* investigation of CdSe–CdS–ZnS core–multishell quantum dots, whereby diffusion and sublimation of species took place with increasing temperature.

In Chapter 4, the *in-situ* thermal stability investigation of Fe_xO/CoFe₂O₄ core/shell HNCs is presented. The thermal evolution of this HNC system is more advanced that diffusion induced reconfiguration was observed.

Chapter 5 focuses on *in-situ* heat induced chemical transformation of CdSe-PbSe HNCs. In this chapter, a novel epitaxial nanowire growth mechanism is introduced. This growth mechanism progresses via cation exchange and is named as "solid-solid-vapor (SSV) growth".

Chapter 2

Experimental techniques

2.1 Transmission Electron Microscopy (TEM)

Throughout the studies presented in this thesis, transmission electron microscopy (TEM) imaging and spectroscopy techniques were used. This chapter is aimed to give a brief overview of these methods.

In a TEM, the electrons are accelerated from an electron gun by using high tension. In a modern TEM, the microscope is equipped with a field emission gun rather than an LaB6 or W filament source, and this improves the resolution which is crucial for nanoscale studies. The electron beam passes through a condenser lens system before reaching the specimen. Conventionally, the condenser lens system consists of two condenser lenses (C1 and C2), but newer TEMs contain also a third condenser lens C3.2 The C3 lens is used to make the incoming electron beam parallel to the specimen as well as achieving smaller probe sizes in scanning transmission electron microscopy studies.² Different interactions of between the specimen and the electrons give rise to different imaging possibilities such as Bright Field TEM (BFTEM) imaging and Annular Dark Field Scanning Transmission Electron Microscopy (ADF-STEM) imaging.³ Note that specimen thickness is of great importance in TEM studies. For a specimen thicker than couple hundred nanometers, certain part of the electron beam cannot leave the specimen and as a result, the image quality decreases substantially or even no image can be formed.

Figure 2.1 illustrates BFTEM and ADF-STEM imaging methods. In BFTEM imaging, directly transmitted beam from the specimen as well as electrons which are elastically scattered over a very small angle are used. In case of ADF-STEM imaging, electrons which are scattered elastically over a large angle are used (larger than 30 mrads).4 The main difference between BFTEM and ADF-STEM imaging is that the incoming beam in BFTEM is more or less parallel, whereas the beam is focused to a spot so called 'probe' and this probe scans the specimen in ADF-STEM. In BFTEM, the electron beam leaving the specimen is focused and magnified by the objective lens and further magnification is done by the intermediate lens system (consists of number of lenses) and the projector lens. The image is formed on a fluorescent screen and it is also possible to have an image by using a CCD camera. In contrast to BFTEM, the C2 lens is weakly excited or even totally disabled in ADF-STEM imaging. The C3 lens forms a probe on the specimen plane. The probe scans the specimen by employing deflection coils. The elastically scattered electrons are collected by the ADF detector and image is therefore formed. The ADF detector can move along the optical axis and as it gets closer to the specimen (decreasing camera length), the electrons scattered over high angles are collected. In this condition, the imaging method is called as High Angle Annular Dark Field STEM (HAADF-STEM) imaging. Z-contrast (Z being atomic number) imaging can be achieved in this mode as the intensity scales approximately with Z².⁵

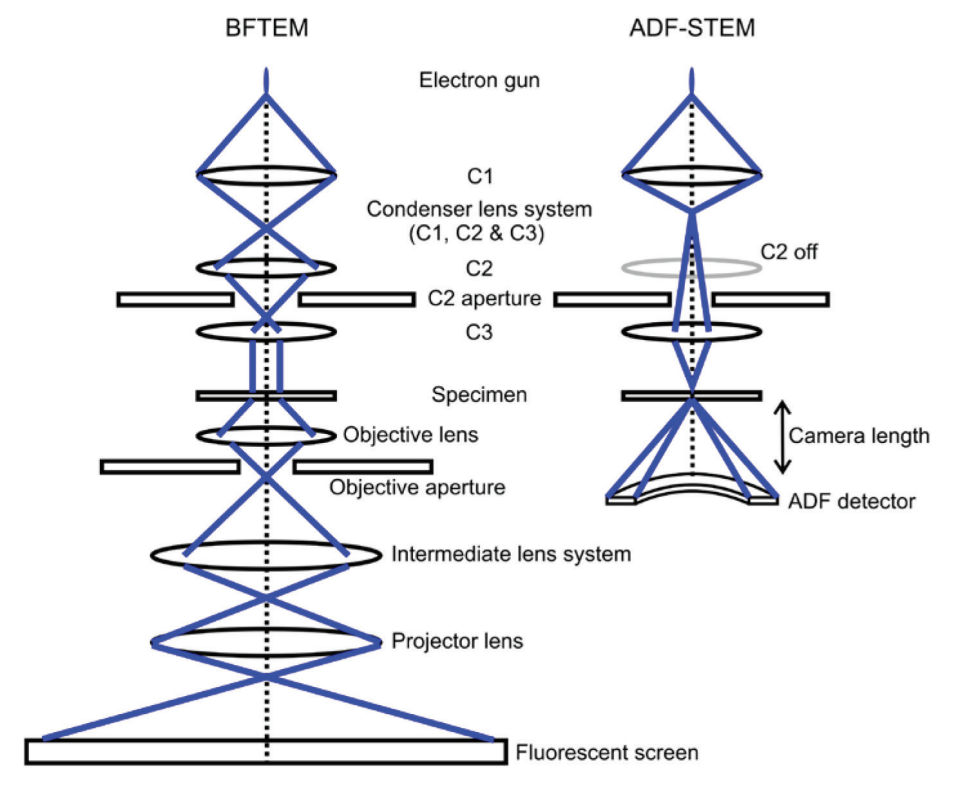


Figure 2.1. Illustration of Bright Field Transmission Electron Microscopy (BFTEM) imaging and Annular Dark Field Scanning Transmission Electron Microscopy (ADF-STEM) imaging techniques. Note that the condenser lens system consists of three lenses, and C2 lens is weakly excited or often disabled in ADF-STEM mode.

BFTEM and HAADF-STEM images of a core/multishell nanostructure with three distinct domains are shown in Figure 2.2. Contrast differences between each domain are clear in both imaging techniques, though impurities on the outer shell are better distinguished in HAADF-STEM imaging.

2.2 TEM specimen holder for *in-situ* heating experiments

In-situ heating experiments presented in this thesis were conducted by using in-house built single-tilt TEM specimen holder. The main advantage of the holder is the achievable resolution of 100 pm at 1000 K, therefore making real time atomic resolution studies possible. An example of the holder is represented in Figure 2.3a. Microelectronic mechanical system (MEMS) microhotplate is mounted in the holder, and this set-up is connected to the in-situ holder via four contact pins (two of the contact pins can be seen in Figure 2.3b). Colloidal heteronanocrystal

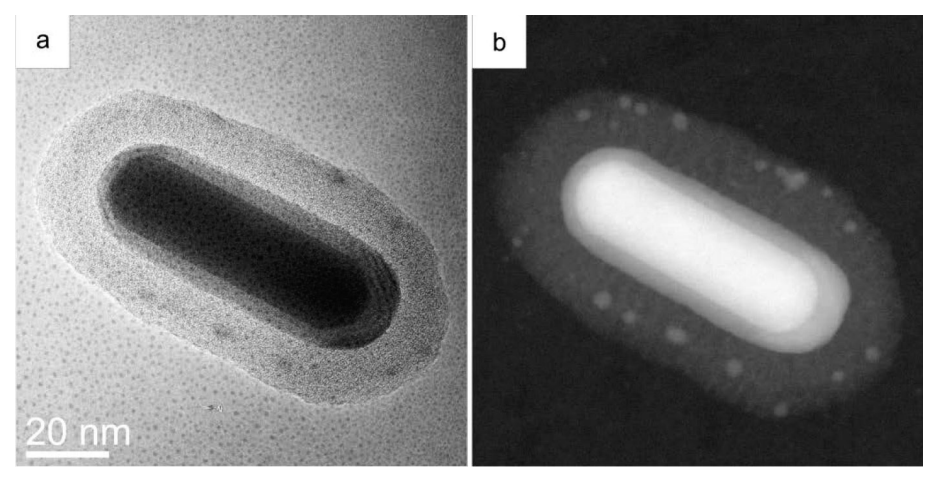


Figure 2.2. BFTEM (a) and HAADF-STEM (b) images of core/multishell nanostructure. The structure is composed of three domains and each domain has distint contrast in both imaging modes, therefore they can be individually distinguished. Note that the impurities on the outer shell are better observed with HAADF-STEM imaging. The scale bar in Figure 2.2a applies also to Figure 2.2b.

solution dropcast onto the MEMS micro-hotplate is heated via embedded planar Pt wire (Figure 2.3c). TEM imaging is conducted along electron transparent 10-15 nm thick SiN support membranes (elongated windows in Figure 2.3d and 2.3e). This set-up is connected to a computer and temperature control is by using a specially designed software.

2.3 Elemental analysis

Elemental characterization studies were carried out by Energy Dispersive X-ray Spectroscopy (EDX), Electron Energy Loss Spectroscopy (EELS) and Energy Filtered TEM (EFTEM).

2.3.1 Energy Dispersive X-ray Spectroscopy (EDX)

EDX is commonly used qualitative as well as quantitative materials characterization method for chemical studies of TEM specimens. This technique lies in the fact that electrons in an element occupy different energy levels (binding energies) represented with K, L and M shells in Figure 2.4. The energy difference between these shells are characteristic for each element. As the electrons in the electron beam are highly accelerated, they can interact with the electrons of the TEM specimen, exciting and kicking out an electron from an inner atomic shell (or shells) of the TEM specimen, and an outer shell electron falls to the inner shell where an electron has been kicked out.⁷ As the energy level the outer shells is much higher than that of the inner shells and is characteristic for each element, the difference in energy is released as an X-ray photon. This characteristic X-ray is collected and characterized by an EDX detector. Several

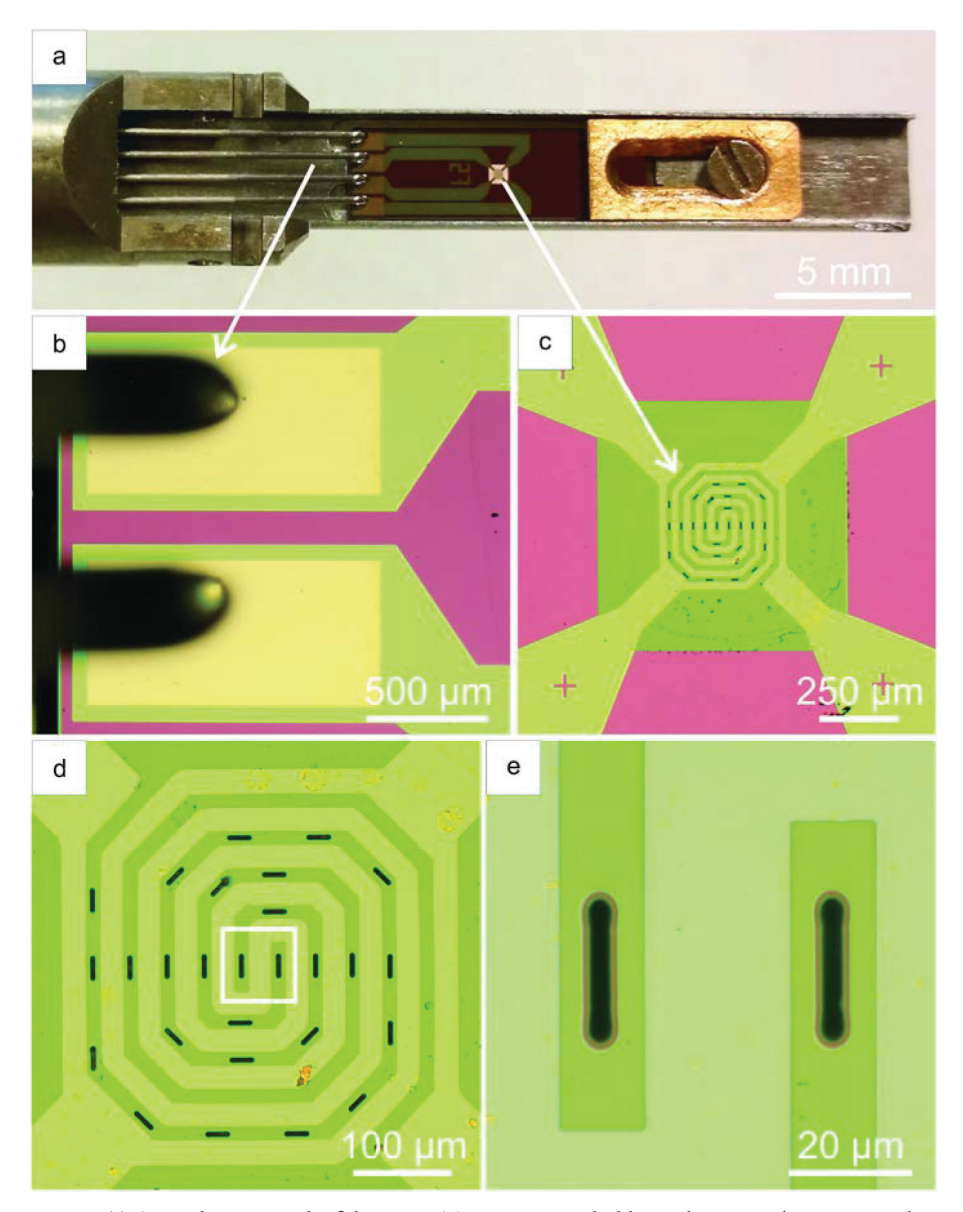


Figure 2.3. (a) Optical micrograph of the in-situ TEM specimen holder with a microelectronic mechanical system (MEMS) micro-hotplate fabricated using silicon-based fabrication technology, (b) Contact pins of the in-situ holder in contact with the MEMS based micro-hotplate (two of the four contact pins in the field of view), (c-e) The center of the micro-hotplate contains an embedded planar Pt wire for local heating. Elongated electron transparent SiN support membranes are 10-15 nm thick, and are located between the windings. The white square depicted in (d) represents the field of view in (e).

characteristic X-rays can be generated from a single element depending on which inner shell an electron is kicked out and from which outer shell an electron falls to the inner shell (depicted with K_{α} , L_{α} and K_{β} in Figure 2.4).

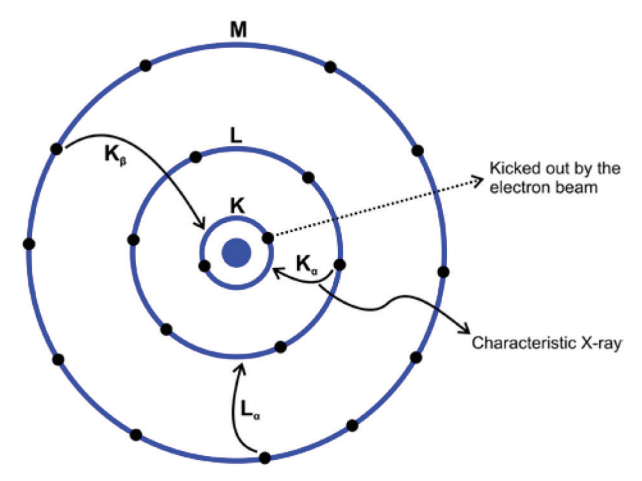


Figure 2.4. Schematic principle of Energy Dispersive X-ray Spectroscopy (EDX). An inner shell electron is excited and kicked-out by the electron beam, and an outer shell electron falls to the inner shell. The energy difference between the shells is released as an X-ray photon, characteristic to each element. The characteristic X-rays are collected and characterized by an EDX detector. Several characteristic X-rays can be detected from a single element resulting from various possible energy level changes (K_{α} , L_{α} and K_{β}).

An example of an EDX spectrum is presented in Figure 2.5. The spectrum was collected from PbSe-CdSe heteronanocrystal system taken from the inset HAADF-STEM image. Note that there are several characteristic X-rays detected for Cd, Se and Pb.

As well as being a spectroscopy technique, it is also possible to obtain elemental distribution of a certain location by using EDX. In this way, one can see from which location(s) characteristic X-rays of an element are generated. Figure 2.6 shows an HAADF-STEM projection of CdSe-PbSe heteronanocrystal system and the corresponding elemental maps of Se, Cd and Pb. EDX elemental maps in Figure 2.6 show that the domains with a bright contrast in the HAADF-STEM image are PbSe and the domains with a dark contrast are CdSe.

Quantitative information can be deduced from an EDX spectrum. Frequently used method to carry out EDX elemental quantification is the Cliff-Lorimer method. Considering a TEM specimen is thin enough so that fluorescence and electron absorption can be neglected, Cliff-Lorimer method defines a relation for two elements (A and B) that the intensities of these elements in the EDX spectrum (I_A and I_B) are proportional to the weight fraction of these elements (W_A and W_B) with the Cliff-Lorimer factor (k_{AB}):⁸

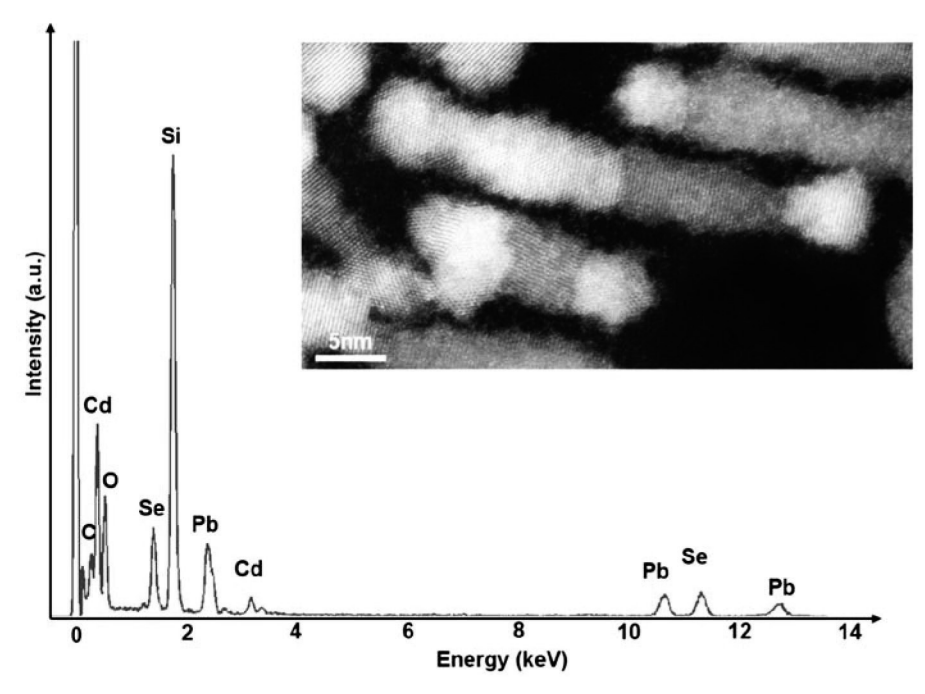


Figure 2.5. Energy Dispersive X-ray Spectrum of a CdSe-PbSe heteronanocrystal system. The inset is the HAADF-STEM image of the heteronanocrystal system where the spectrum was taken. Note that the silicon signal is coming from the SiN membrane that the colloidal solution was dropcast onto, and the oxygen signal is coming from the Pb-oleate molecules present in the solution. The domains with a bright contrast represents PbSe and the domains with a dark contrast represent CdSe.

$$\frac{W_A}{W_B} = k_{AB} \frac{I_A}{I_B} \tag{2.1}$$

Electron Energy Loss Spectroscopy (EELS) and Energy Filtered TEM (EFTEM) 2.3.2

As illustrated in Figure 2.4, the electrons in an element are positioned in shells (K, L, M etc.) with different binding energies to nucleus. While beam electrons pass through a TEM specimen, they interact with elemental electrons. This interaction is an inelastic phenomenon that elemental electrons can absorb certain energy from beam electrons and become excited (kicked out from the shell). As a result, the beam electrons providing this energy to the excited elemental electrons are inelastically scattered. These inelastically scattered electrons can be collected and plotted in a spectrum with respect to their energy loss (eV). This spectrum is called Electron Energy Loss Spectrum (EELS) and loss peaks in the spectrum are used for elemental characterization.

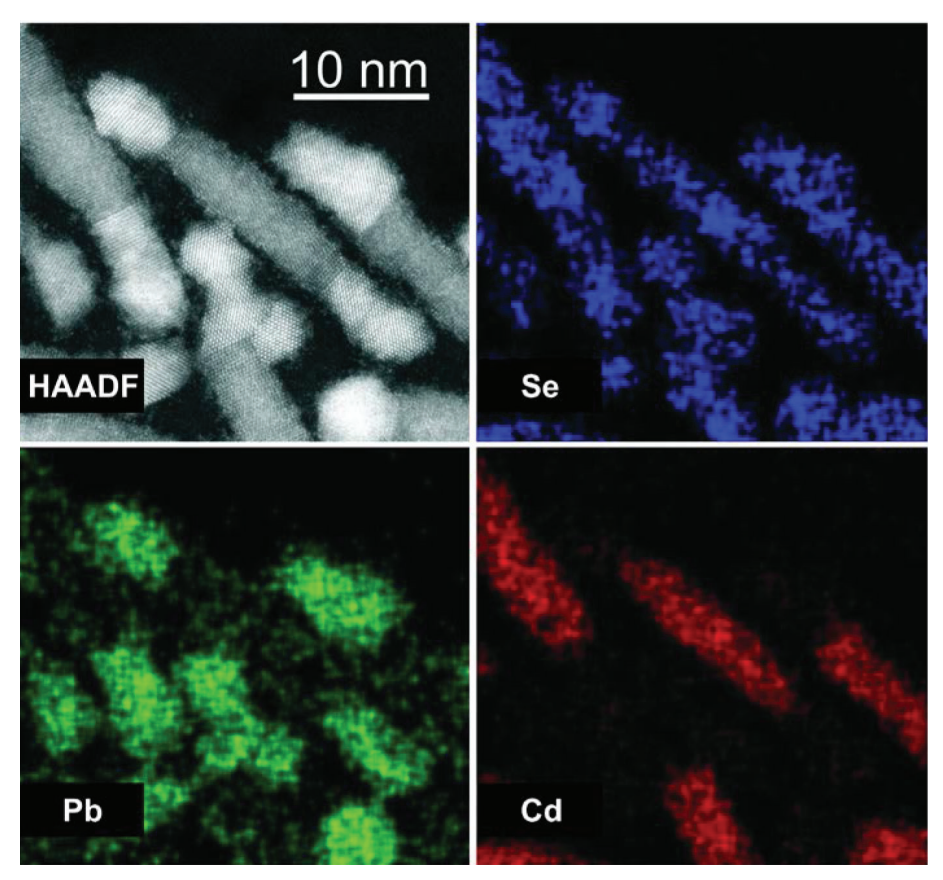


Figure 2.6. HAADF-STEM image of CdSe-PbSe heteronanocrystal system and corresponding Se, Pb and Cd elemental maps obtained by EDX. The scale bar applies to all images. Elemental maps indicate that domains with a dark contrast are CdSe and domains with a bright contrast are PbSe.

Figure 2.7 represents an EEL spectrum of Fe_xO/CoFe₂O₄ core/shell heteronanocrystal system (inset BFTEM image). The peak positioned at 532 eV loss corresponds to the oxygen K-edge, meaning that the oxygen K-shell electrons absorb an energy of 532 eV from the beam to become excited.

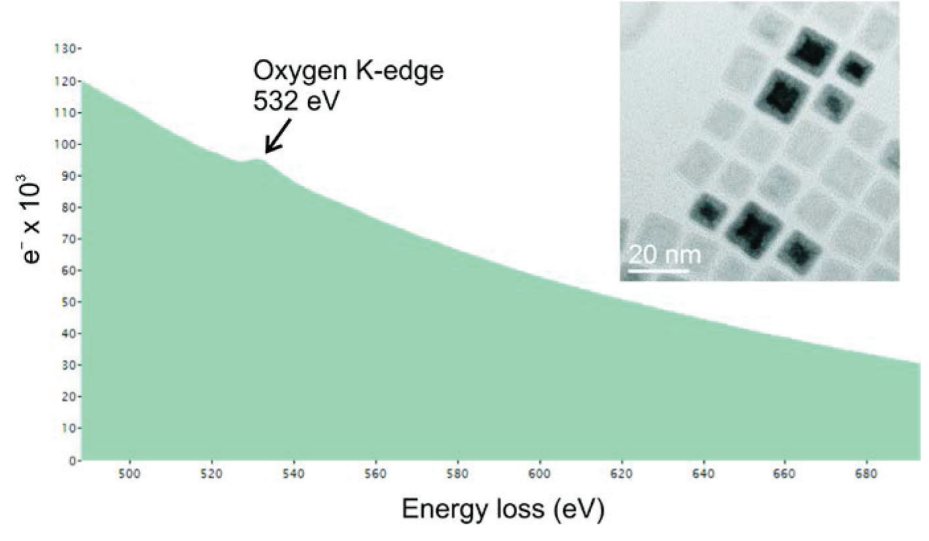


Figure 2.7. Electron Energy Loss (EEL) spectrum of Fe₂O/CoFe₂O₄ core/shell heteronanocrystal system (inset BFTEM image). The oxygen K-edge is at 532 eV energy loss.

Besides a spectroscopic technique, EELS is also used in imaging, so called Energy Filtered TEM (EFTEM), providing spectroscopic elemental maps. In EFTEM imaging, after having the absorption edge of a certain element, the electrons with an energy loss higher than that of the absorption edge (post-edge) and the electrons with an energy loss lower than that of the absorption edge (pre-edges) are collected within a certain energy range by using a slit. Two pre-edges are used to extrapolate the background and the resulting image is subtracted from post-edge, therefore the final elemental map is obtained. As three edges are used to obtain the final map, this method is called three-window method. An example of EFTEM imaging is shown in detail in Figure 2.8. Figure 2.8a is the unfiltered BFTEM image of Fe_xO-CoFe₂O₄ heteronanocrystal system at 530 °C and Figure 2.8b is the corresponding EFTEM Co map obtained by using three-window method. Fe, O domain exhibits dark contrast in the unfiltered BFTEM image and dotted lines were used to clarify this domain in Figure 2.8a and 2.8b. Figure 2.8c shows the two pre-edge and the post-edge spectroscopic images which were used in three-window method for Co mapping. The $L_{2,3}$ edge of Co is at 779 eV and a slit width of 20 eV was used in this EFTEM study. This study showed that Co can diffuse into Fe_xO domains at elevated temperatures.¹⁰

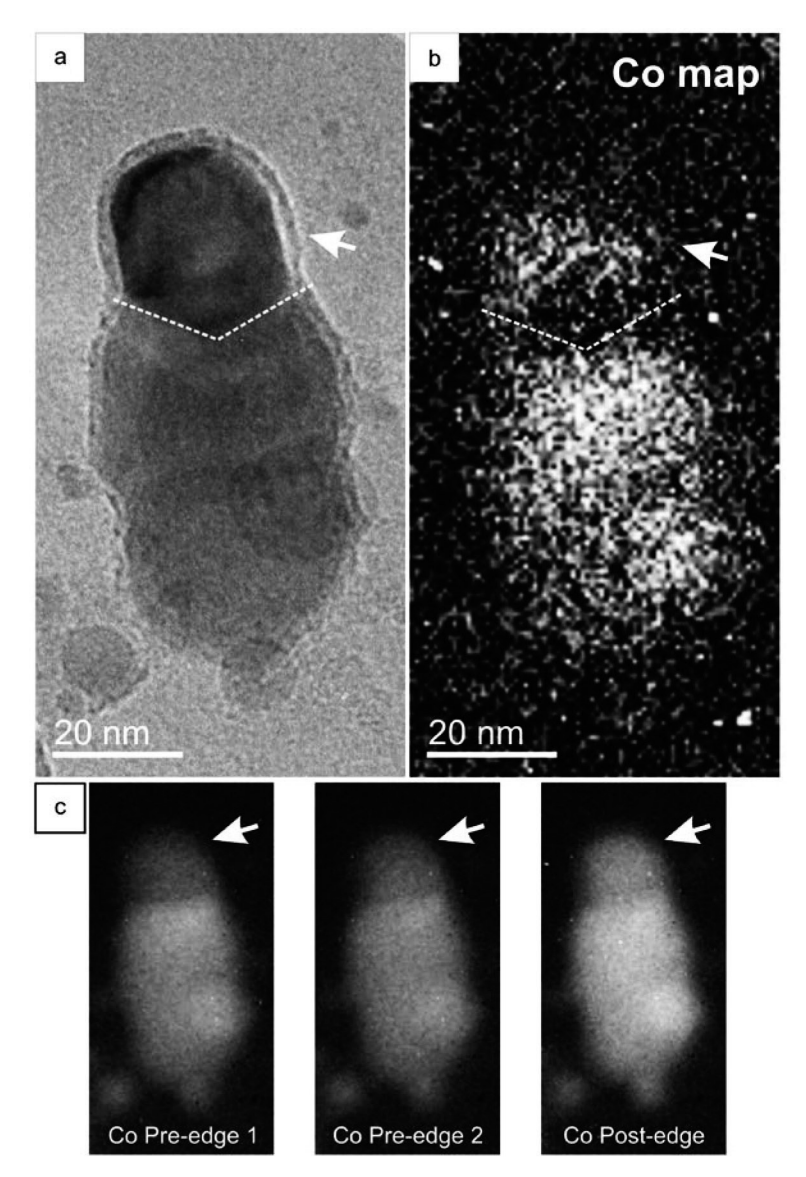


Figure 2.8. Energy Filtered TEM (EFTEM) Co-mapping of Fe_xO -CoFe₂O₄ heteronanocrystal system at 530 °C. (a) Unfiltered BFTEM image, (b) corresponding EFTEM Co map, (c) three-window method to obtain EFTEM Co map. The $L_{2,3}$ edge of Co is at 779 eV and a slit width of 20 eV was used in this EFTEM study. EFTEM study revealed that heated Fe_xO domain can contain Co. The arrows show the Fe_xO domain with the presence of Co.

References

- Williams, D. B.; Carter, C. B. Transmission Electron Microscopy: A Textbook for Materials Science, 1 Second Edition; Springer: New York, 2009; Part 1, pp 73-74.
- 2 Williams, D. B.; Carter, C. B. Transmission Electron Microscopy: A Textbook for Materials Science, Second Edition; Springer: New York, 2009; Part 1, pp 141-146.
- Williams, D. B.; Carter, C. B. Transmission Electron Microscopy: A Textbook for Materials Science, 3 Second Edition; Springer: New York, 2009; Part 1, pp 7-8.
- 4 Weyland, M.; Thomas J. M.; Dunin-Borkowski, R. E.; Midgley, P. A. High spatial resolution tomographic reconstruction from STEM high angle annular dark field (HAADF) images. Inst. Phys. Conf. Ser. 2001, 168, 107-110 (EMAG 2001).
- Yalcin, A. O.; Fan, Z.; Goris, B.; Li, W.-F.; Koster, R. S.; Fang, C.-M.; van Blaaderen, A.; Casavola, 5 M.; Tichelaar, F. D.; Bals, S.; Van Tendeloo, G.; Vlugt, T. J. H.; Vanmaekelbergh, D.; Zandbergen, H. W.; van Huis, M. A. Atomic Resolution Monitoring of Cation Exchange in CdSe-PbSe Heteronanocrystals during Epitaxial Solid-Solid-Vapor Growth. Nano Lett. 2014, 14, 3661-3667.
- van Huis, M. A.; Young, N. P.; Pandraud, G.; Creemer, J. F.; Vanmaekelbergh, D.; Kirkland, A. I.; 6 Zandbergen, H. W. Atomic Imaging of Phase Transitions and Morphology Transformations in Nanocrystals. Adv. Mater. 2009, 21, 4992-4995.
- Williams, D. B.; Carter, C. B. Transmission Electron Microscopy: A Textbook for Materials Science, 7 Second Edition; Springer: New York, 2009; Part 4, pp 605-606.
- 8 Malladi, S. K. In-situ TEM studies: Heat-treatment and Corrosion. Ph.D. Thesis, Delft University of Technology, February 2014.
- Leapman, R. In Transmission Electron Energy Loss Spectrometry in Materials Science and the EELS Atlas, Second Edition; Ahn, C. C., Ed.; John Wiley & Sons: Darmstadt, 2006; pp 83-84.
- 10 Yalcin, A. O.; de Nijs, B.; Fan, Z.; Tichelaar, F. D.; Vanmaekelbergh, D.; van Blaaderen, A.; Vlugt, T. J. H.; van Huis, M. A.; Zandbergen, H. W. Core-shell reconfiguration through thermal annealing in Fe_xO/CoFe₂O₄ ordered 2D nanocrystal arrays. Nanotechnology 2014, 25, 055601.

Chapter 3

Zn inner diffusion in CdSe–CdS–ZnS core–multishell system

Abstract

In this work, we investigate the thermal evolution of CdSe–CdS–ZnS core–multishell quantum dots (QDs) *in-situ* using transmission electron microscopy (TEM). Starting at a temperature of approximately 250 °C, Zn diffusion into inner layers takes place together with simultaneous evaporation of particularly Cd and S. As a result of this transformation, Cd_xZn_{1-x}Se–Cd_yZn_{1-y}S core–shell QDs are obtained.

This chapter is based on the publication:

Yalcin, A.O. et al. Chem. Commun., 2015, 51, 3320-3323.

This publication has featured as the inside front cover of the journal (*Chem. Commun.* Volume 51, Issue 16).



3.1 Introduction

CdSe, a II-VI type semiconductor, is a widely studied nanocrystal (NC) in colloidal science as its emission can cover the whole visible spectrum via size tuning,^{1,2} making CdSe NCs important for several applications such as biolabeling and LEDs.^{3,4} Despite having interesting functional properties, NCs in general suffer from instability, in particular surface oxidation,^{5,6} due to the high surface to volume ratio. In order to increase the stability of CdSe QDs, a wideband gap II-VI semiconductor such as ZnS can be successfully grown onto a CdSe core. The advantage of a wide-band gap ZnS shell is that both electrons and holes are kept confined in the core with increased stability as well as decreased toxicity.⁷⁻¹⁰ However, the lattice mismatch in the CdSe-ZnS core-shell system is about 12%, leading to interfacial strain, thus resulting in the formation of trap sites for charge carriers and increased blinking. 1,8,11-13 In order to overcome this problem, an intermediate layer of CdS with a lattice constant between CdSe and ZnS can be incorporated into the structure. 7,14-16 With this CdS intermediate layer, the interfacial strain is reduced and the optical properties are enhanced.^{7,14-16} We thus speak of CdSe-CdS-ZnS core-multishell QDs.

Although the knowledge on the synthesis of NCs as well as the optical properties of NCs are now advanced, detailed information on thermal and temporal behavior of these structures is limited. In-situ transmission electron microscopy (TEM) coupled with the microelectronic mechanical system (MEMS) technology can shed light on various interesting thermal changes in nanostructures, which can be of critical importance for the implementation of these QDs in devices. For example, in CdSe-CdS dot-in-octapod morphology NCs, heating induces the segregation of pure Cd domains at the side of the octapods.¹⁷ In another work, the Fe_xO-CoFe₂O₄ core-shell system undergoes a heat induced reconfiguration whereby Fe_xO leaves the core location and segregates at the side of CoFe₂O₄ domain while CoFe₂O₄ shrinks and fills the core volume.18

Here, we show the thermal evolution of CdSe-CdS-ZnS core-multishell QDs whereby Zn diffusion into the inner layers of the QDs takes place at elevated temperatures. The structure evolves into Cd_xZn_{1-x}Se-Cd_yZn_{1-y}S core-shell QDs with irregular morphologies.

Methods 3.2

The synthesis of the CdSe-CdS-ZnS colloidal QDs was performed as follows: CdSe QD seeds were synthesized first,19 and then a CdS-ZnS multishell was grown onto CdSe QD seeds via the successive ion layer adhesion and reaction (SILAR) method.⁷ In order to minimize the interfacial strain between the CdS and ZnS shells, a monolayer of CdZnS was grown in between. Details about the synthesis can be found in Appendix A. For *in-situ* heating experiments, 8 μL of colloidal QD solution was deposited on a MEMS based micro-hotplate inside an argonatmosphere glove box. After the evaporation of the solvent, the set-up was mounted on an in-house built low drift heating holder.²⁰ The *in-situ* heating experiments were conducted using two different Cs-corrected FEI Titan microscopes, one of which is equipped with a high-brightness gun and a Chemi-STEM (Scanning Transmission Electron Microscopy) detection system for Energy Dispersive X-ray Spectroscopy (EDX). Both Bright Field TEM (BF-TEM) and High Angle Annular Dark Field STEM (HAADF-STEM) imaging techniques were used in our studies. In order to prevent beam damage while using the high-brightness gun in Chemi-STEM elemental map studies, a relatively low acceleration voltage of 120 kV was employed. Other studies were carried out at an acceleration voltage of 300 kV. A camera length of 115 mm was used in HAADF-STEM studies to limit diffraction effects in this mode.

3.3 Results & Discussion

Figure 3.1a presents an HAADF-STEM projection of several CdSe-CdS-ZnS core-multishell QDs at their initial state at room temperature (RT). Corresponding elemental maps of Se, S, Cd and Zn are displayed in Figure 3.1b-3.1e, and an overlay of the Cd and the Zn map is presented in Figure 3.1f. From the maps, it is clear that the QDs consist of a CdSe core, a CdS intermediate layer and a ZnS outer shell. The Se-map (Figure 3.1b) as well as the empty QD centers in the S-map (Figure 3.1c) indicate the CdSe core region. The overlay of the Cd- and Zn-maps (Figure 3.1f) clearly demonstrate the outer shell. From the elemental quantifications performed on 10 different QDs (Table A.2 in Appendix A), the average cation/anion ratio was found to be 0.99±0.05 throughout the structure. All elemental quantifications were performed using the Cliff-Lorimer method with k-factors as implemented in the Bruker ESPRIT software. Figure 3.1g and 3.1h show high resolution (HR) TEM images of two QDs along [001] and [110] zones respectively. From the HRTEM images and inset Fourier Transforms (FTs), the crystal structure was found to be hexagonal wurtzite. HRTEM images did not show any defects or irregularities throughout the structure, showing that the CdS-ZnS shell was grown epitaxially on CdSe.^{7,15} The FTs do not reveal separate atomic spacings of different layers. It has been reported that in the CdSe-CdS core-shell and the CdSe-CdS-ZnS core-multishell systems, the CdSe core is compressed by the shell domains. 15,21 As a result, the atomic spacings of CdSe are reduced. From the FTs, we observed the atomic spacings close to that of CdS as most of the QD is composed of the CdS intermediate layer and therefore dominating the structural properties of the QDs as a whole.

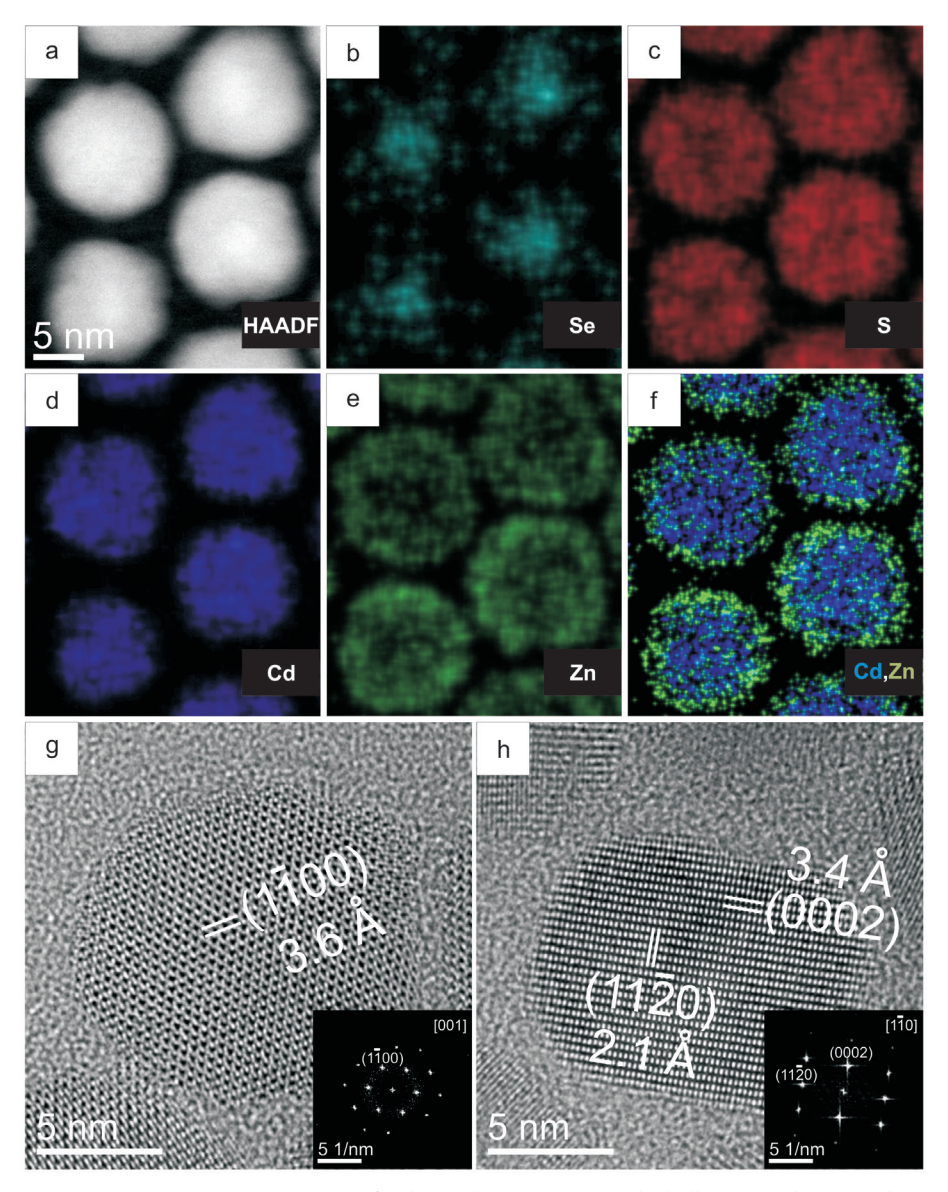


Figure 3.1. (a) HAADF-STEM image of CdSe-CdS-ZnS core-multishell QDs at their initial state at RT. (b-f) Corresponding Se, S, Cd and Zn elemental maps and an overlay of the Cd and Zn elemental maps obtained by EDX mapping. The scale bar in Figure 3.1a applies also to Figure 3.1b-3.1f. (g and h) HRTEM images of two QDs along two different zone axes.

When CdSe-CdS-ZnS core-multishell QDs were heated in the TEM, we observed a morphological and structural change as depicted in Figure 3.2. The initially sphere-like QDs adopted irregular shapes starting at temperatures of 250 °C and higher. Considering the elemental distribution, Figure 3.2 shows that Zn diffused into the inner layers of the QD structure. The high temperature Zn-map (Figure 3.2e) covered the QD structures completely, which was not the case at the initial state (Figure 3.1e) where Zn was only present in the outer shell. Note that chemical mapping was always performed in areas not previously exposed to the electron beam, and the transformation was found to take place on the entire TEM support membrane, indicating that the electron beam did not initiate the transformation. In the literature, Zn diffusion has been observed in CdSe-ZnSe²²⁻²⁴ and Cd_{1-x}Zn_xS-ZnS core-shell structures^{25,26} at elevated temperatures. It has been reported that cations in II-VI semiconductors such as ZnS have a high tendency to diffuse. 27-29 Considering the anions, the Se-map (Figure 3.2b) shows that Se retains its position in the core at high temperature. Moreover, the QD centers in the S-maps (Figure 3.2c) are still dark, indicating that S did not diffuse into the core. Note that besides the change in the structure and morphology, the overall size of the QDs became smaller at elevated temperature due to simultaneous evaporation of cation and anion species. The cation/anion ratio obtained through elemental quantification of 10 different QDs verifies this (Table A.3 in Appendix A). At elevated temperature, the average cation/anion ratio was found to be 0.96±0.08, which is similar to the ratio at the initial state. In order for this to happen, simultaneous sublimation of species (particularly Cd and S) should take place, so that Zn can replace some Cd in CdS and CdSe. Unless the in-diffusing Zn atoms all occupy interstitial sites, the in-diffusion of Zn is accompanied by out-diffusion of part of the Cd atoms and subsequent evaporation. The diffusion process could be either a vacancy-assisted migration mechanism,³⁰ or an interstitial-substitutional migration mechanism.31

From the quantifications, the average Cd content in the whole QD decreased from 38 at.% to 27 at.% and the average Zn content increased from 12 at.% to 22 at.%, suggesting the evaporation of Cd with heating. We mention here that the vapour pressure of pure Cd is two orders of magnitude higher than that of pure Zn in this temperature range,³² but the evaporation from the QD also depends on the bond strengths of the compounds. Cd evaporation from heterogeneous NCs was previously observed when sandwich morphology CdSe–Cu₃P–CdSe NCs were heated.³³ Recently, we also observed Cd evaporation in CdSe-PbSe heterogeneous NCs at temperatures even lower than 200 °C.³⁰ The average atomic percentages of anions (Se and S) in the QDs did not change much with heating. As the average cation/anion ratio after the transformation was found to be as 0.96±0.08 (still close to 1), not only cations but also anions should have evaporated during heating. In summary, as a result of *in-situ* heating, CdSe–CdS–ZnS core–multishell QDs transformed into a two-layer Cd_xZn_{1-x}Se–Cd_yZn_{1-y}S core–shell QDs.

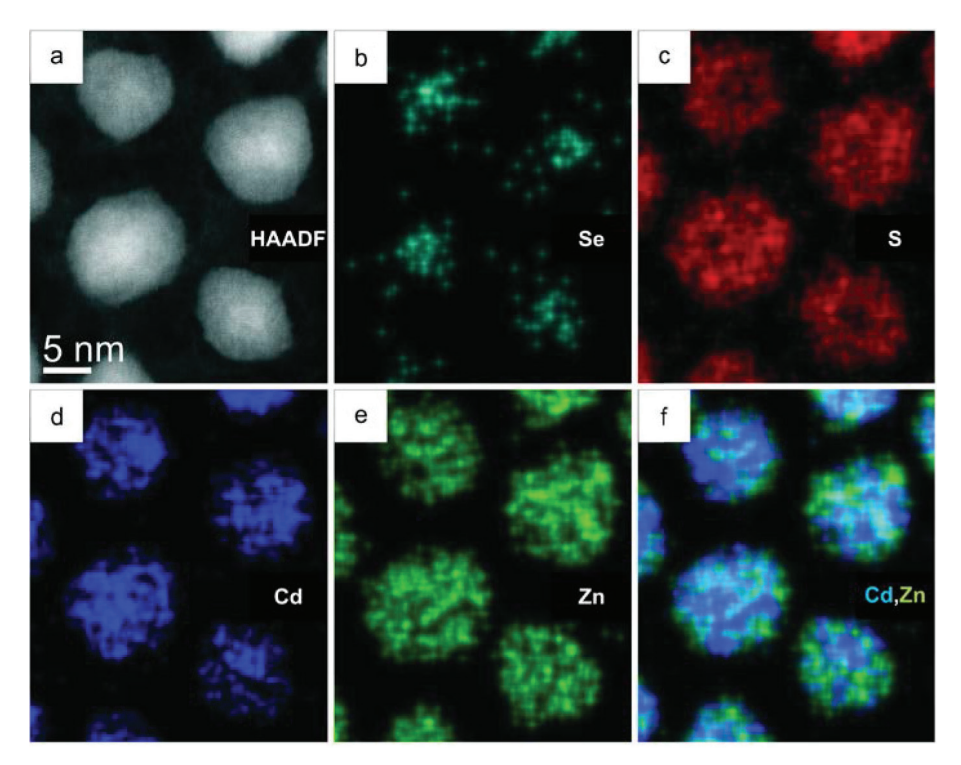


Figure 3.2. (a) HAADF-STEM image of QDs at 275 °C. (b-f) Corresponding Se, S, Cd and Zn elemental maps and an overlay of the Cd and Zn elemental maps obtained by EDX mapping. Elemental maps indicate that CdSe-CdS-ZnS QDs transformed into Cd_vZn_{1-v}Se-Cd_vZn_{1-v}S core-shell structure by Zn diffusion into the inner layers. The scale bar in Figure 3.2a applies to all images.

To monitor the effect of heating on the crystal structure, the evolution of a single QD was followed in high resolution. Figure 3.3 shows high resolution HAADF-STEM images of a single QD at different temperatures until the sublimation at 310 °C. The QD was oriented along the [001] projection (along the c-axis). The FT of each image in Figure 3.3 is placed below each corresponding image. The QD retained the hexagonal wurtzite crystal structure up to the sublimation point. At a temperature of 270 °C (Figure 3.3b), a dark spot in the middle of QD was observed, possibly due to accumulation of radiation damage caused by the focused electron beam during imaging in high resolution. Note that the 'parking position' of the electron probe was far away from the QD in order to limit beam induced damage. With heating, the morphology of the QD changed at first and a significant part of the QD sublimated later.

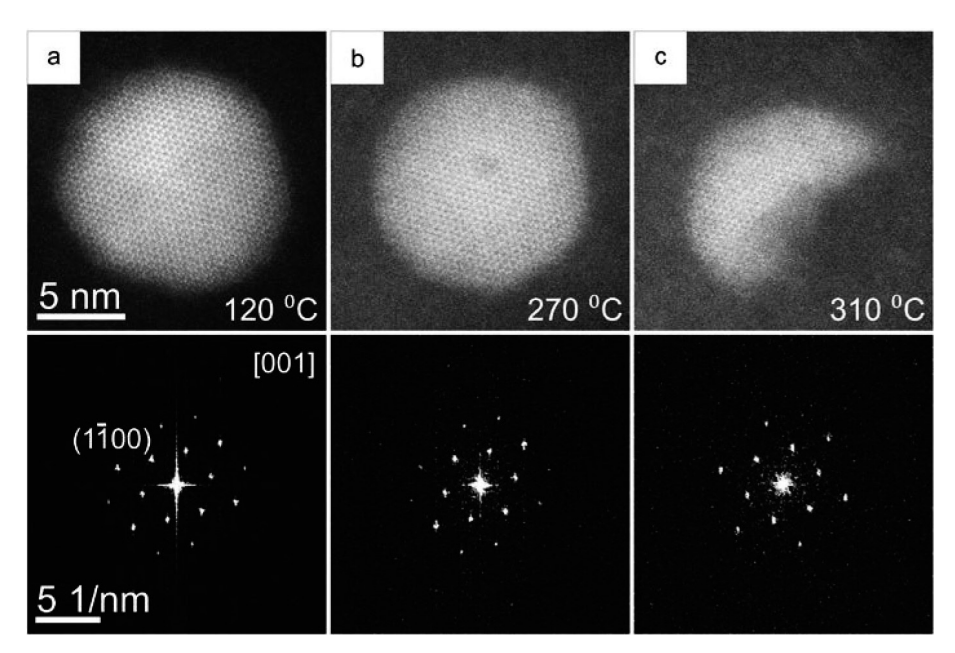


Figure 3.3. High resolution HAADF-STEM study of a QD during thermal evolution at temperatures of (a) 120 °C, (b) 270 °C and (c) 310 °C. The FT of each image is placed below the image. The scale bars in Figure 3.3a and in the corresponding FT apply to all images and FTs.

Interestingly, the radiation damage studies was useful to monitor the mobility of ions in high resolution. Figure 3.4 shows a QD undergoing thermal evolution. The QD was monitored in HAADF-STEM mode along [001] zone. Black dots are placed at the center of each image and the central part of the QD is magnified in the corresponding insets for clarity. At 240 °C (Figure 3.4b), radiation damage depicted with a black arrow started to form similar to the case in Figure 3.3b. With respect to the central black dot, the radiation damage changed location under heat treatment from the south-east side (Figure 3.4b and the corresponding inset) to the north-east (Figure 3.4c and the corresponding inset) and then again the south-east side (Figure 3.4d and the corresponding inset). The changing location of the radiation damage shows that the ions from other locations diffused towards the radiation damaged QD part and repaired the damage. However, as those ions left vacant sites behind, the damage changed location on the QD. Note that the morphology became more irregular with temperature and the decreasing size of the QD was due to simultaneous evaporation.

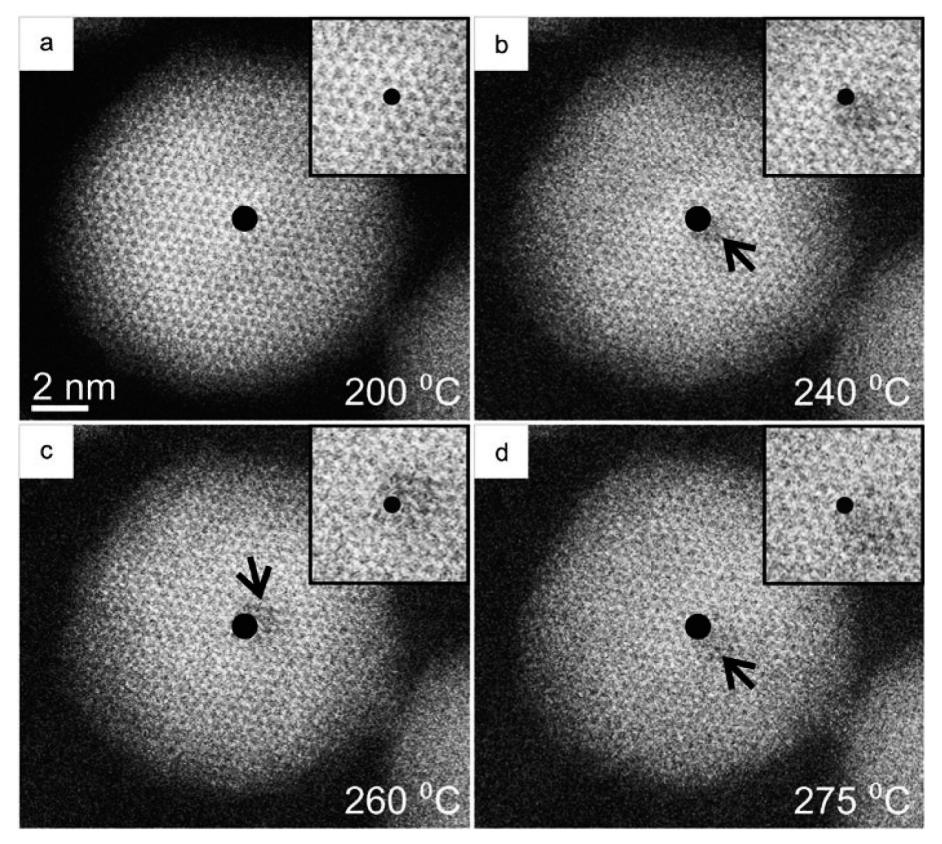


Figure 3.4. In-situ high resolution heat treatment of CdSe-CdS-ZnS core-multishell QD in HAADF-STEM mode at temperatures of (a) 200 °C, (b) 240 °C, (c) 260 °C and (d) 275 °C. The black dots are the center of each image and central part of the images are magnified in the corresponding insets. Due to focused beam in high resolution, radiation damage took place and the damage changed location representing the mobility of species. The scale bar in Figure 3.4a applies to all images.

3.4 **Conclusions**

In this study, we have shown in-situ the thermal evolution of CdSe-CdS-ZnS core-multishell QDs into Cd_xZn_{1-x}Se-Cd_xZn_{1-y}S core-shell QDs by Zn diffusion into the inner layers of the QDs starting from approximately 250 °C. The initially sphere-like morphology of the QDs became irregular with the heat treatment and the QDs became smaller in size due to simultaneous evaporation of cation and anion species (particularly Cd and S). High resolution HAADF-STEM studies revealed that the hexagonal wurtzite crystal structure was retained up to the sublimation point and mobility of ions at elevated temperature was monitored through changing location of the radiation damage on the QD.

References

- D. V. Talapin, I. Mekis, S. Götzinger, A. Kornowski, O. Benson and H. Weller, *J. Phys. Chem. B*, 2004, 108, 18826.
- 2 S. A. Empedocles and M. G. Bawendi, *Science*, 1997, 278, 2114.
- 3 A. Samanta, Z. Deng and Y. Liu, Langmuir, 2012, 28, 8205.
- 4 A. M. Munro and D. S. Ginger, *Nano Lett.*, 2008, 8, 2585.
- 5 B. De Geyter and Z. Hens, Appl. Phys. Lett., 2010, 97, 161908.
- 6 R. C. Somers, M. G. Bawendi and D. G. Nocera, *Chem. Soc. Rev.*, 2007, 36, 579.
- 7 R. Xie, U. Kolb, J. Li, T. Basché and A. Mews, J. Am. Chem. Soc., 2005, 127, 7480.
- 8 S. Xu, H. Shen, C. Zhou, H. Yuan, C. Liu, H. Wang, L. Ma and L. S. Li, *J. Phys. Chem. C*, 2011, 115, 20876.
- 9 H. Shen, S. Wang, H. Wang, J. Niu, L. Qian, Y. Yang, A. Titov, J. Hyvonen, Y. Zhen, and L. S. Li, *ACS Appl. Mater. Interfaces*, 2013, 5, 4260.
- 10 K. Kim, C. J. Han, Y. C. Park, Isnaeni, Y.-H. Cho and S. Jeong, Nanotechnology, 2013, 24, 505601.
- 11 X. Wang, X. Ren, K. Kahen, M. A. Hahn, M. Rajeswaran, S. Maccagnano-Zacher, J. Silcox, G. E. Cragg, A. L. Efros and T. D. Krauss, *Nature*, 2009, 459, 686.
- B. Mahler, P. Spinicelli, S. Buil, X. Quelin, J.-P. Hermier and B. Dubertret, *Nat. Mater.*, 2008, 7, 659.
- 13 H. Shen, H. Wang, C. Zhou, J. Z. Niu, H. Yuan, L. Ma and L. S. Li, *Dalton Trans.*, 2011, 40, 9180.
- 14 X. Wang, W. Li and K. Sun, J. Mater. Chem., 2011, 21, 8558.
- 15 L. Manna, E. C. Scher, L-S. Li and A. P. Alivisatos, J. Am. Chem. Soc., 2002, 124, 7136.
- S. Deka, A. Quarta, M. G. Lupo, A. Falqui, S. Boninelli, C. Giannini, G. Morello, M. De Giorgi, G. Lanzani, C. Spinella, R. Cingolani, T. Pellegrino and L. Manna, J. Am. Chem. Soc., 2009, 131, 2948.
- 17 B. Goris, M. A. van Huis, S. Bals, H. W. Zandbergen, L. Manna and G. Van Tendeloo, *Small*, 2012, 8, 937.
- A. O. Yalcin, B. de Nijs, Z. Fan, F. D. Tichelaar, D. Vanmaekelbergh, A. van Blaaderen, T. J. H. Vlugt, M. A. van Huis and H. W. Zandbergen, *Nanotechnology*, 2014, 25, 055601.
- 19 X. Peng, M. C. Schlamp, A. V. Kadavanich and A. P. Alivisatos, J. Am. Chem. Soc., 1997, 119, 7019.
- 20 M. A. van Huis, N. P. Young, G. Pandraud, J. F. Creemer, D. Vanmaekelbergh, A. I. Kirkland and H. W. Zandbergen, *Adv. Mater.*, 2009, 21, 4992.
- 21 N. Tschirner, H. Lange, A. Schliwa, A. Biermann, C. Thomsen, K. Lambert, R. Gomes and Z. Hens, *Chem. Mater.*, 2012, 24, 311.
- 22 Y.-M. Sung, Y.-J. Lee and K.-S. Park, J. Am. Chem. Soc., 2006, 128, 9002.
- 23 K. G. Sonawane, K. R. Patil and S. Mahamuni, J. Lumin., 2013, 135, 154.
- 24 H. Lee, P. H. Holloway and H. Yang, J. Chem. Phys., 2006, 125, 164711.
- 25 W. K. Bae, M. K. Nam, K. Char and S. Lee, Chem. Mater., 2008, 20, 5307.

- 26 X. Liu, Y. Jiang, F. Fu, W. Guo, W. Huang and L. Li, Mater. Sci. Semicond. Process., 2013, 16, 1723.
- 27 K. Boldt, N. Kirkwood, G. A. Beane and P. Mulvaney, Chem. Mater., 2013, 25, 4731.
- X. Zhong, M. Han, Z. Dong, T. J. White and W. Knoll, J. Am. Chem. Soc., 2003, 125, 8589. 28
- J. Xu, X. Yang, H. Wang, X. Chen, C. Luan, Z. Xu, Z. Lu, V. A. L. Roy, W. Zhang and C-S. Lee, 29 Nano Lett., 2011, 11, 4138.
- A. O. Yalcin, Z. Fan, B. Goris, W.-F. Li, R. S. Koster, C.-M. Fang, A. van Blaaderen, M. Casavola, 30 F. D. Tichelaar, S. Bals, G. Van Tendeloo, T. J. H. Vlugt, D. Vanmaekelbergh, H. W. Zandbergen and M. A. van Huis, Nano Lett., 2014, 14, 3661.
- 31 F. D. Ott, L. L. Spiegel, D. J. Norris and S. C. Erwin, Phys. Rev. Lett., 2014, 113, 156803.
- J. C. Greenbank and B. B. Argent, Trans. Faraday Soc., 1965, 61, 655. 32
- 33 L. De Trizio, F. De Donato, A. Casu, A. Genovese, A. Falqui, M. Povia and L. Manna, ACS Nano, 2013, 7, 3997.

Appendix A

A.1 CdSe-CdS-ZnS core-multishell QD synthesis method

All nanocrystal syntheses were performed in a nitrogen atmosphere and stored in a glovebox and with pre-dried chemicals.

Chemicals:

Cd(Ac)₂ (Sigma-Aldrich, 99%), diethylzinc (Et₂Zn, Sigma-Aldrich, 1.0 M solution in hexane), Oleic acid (OA, Sigma-Aldrich, 90%), octadecene (ODE, Sigma-Aldrich, 90%), octadecene amine (ODA, Sigma-Aldrich, 90%) selenium (Strem Chemicals, 99.99%), sulphur (Alfa Aesar, 99%), trioctylphosphine (TOP, Sigma-Aldrich, 90%), trioctylphosphine oxide (TOPO, Sigma-Aldrich, 99%), were used for the synthesis of QDs.

Solvents:

Acetone (Merck), cyclohexane (Sigma-Aldrich, anhydrous, 99%), hexane (Sigma-Aldrich, anhydrous, 99.8%), methanol (Sigma-Aldrich, anhydrous, 99.8%), toluene (Sigma-Aldrich, anhydrous, 99.8%)

Synthesis of CdSe QD seeds:1

Prior to the synthesis of the CdSe QDs, 2 precursors were synthesized. OA (3.68 g), ODE (25.92 g), and Cd(Ac)₂ (0.64 g) were mixed, heated to 150°C, and kept under vacuum for 2 h to form Cd(OA)₂. Selenium (4.25 g) was dissolved in TOP (22.5 g) at 50 °C, followed by the addition of ODE (35.7 g). CdSe nanocrystal seeds were synthesized in 50 ml three-neck flask using a Schlenk-line. TOPO (1.11 g), ODA (3.20 g), and Cd(OA), precursor (4.9 g) were mixed, heated to 300 °C. When this temperature was reached, the Se-precursor (5.2 g) was added rapidly. The size of the QDs can be tuned via changing the reaction time.

The particles were diluted by adding 1 equivalent of hexane. The QDs were washed by adding 2 equivalents of methanol and collecting the upper hexane layer (coloured) and add 1 equivalent of acetone to precipitate the QDs. Finally, the nanocrystal seeds were re-dissolved in toluene and stored inside a glove box under nitrogen atmosphere.

Typical synthesis of CdSe-CdS-ZnS core-multishell QDs:2

Prior to the synthesis of the CdSe QDs, three precursors were prepared. The zinc precursor solution (0.1 M) was prepared by dissolving Zn(Et), (0.494 g) in oleic acid (5.05 mL) and ODE (19.8 mL) at 310 °C. The cadmium precursor solution (0.1 M) was prepared by dissolving Cd(Ac)₂ (1.10 g) in oleic acid (10.83 g) and ODE (43.20 mL) at 120 °C under vacuum for 2 h. The sulphur precursor solution (0.1 M) was prepared by dissolving sulphur (0.032 g) in ODE (10 mL) at 180 °C. The Cd-, and Zn-precursor Cd/Zn-precursor solutions were kept at about 80 °C, while the sulphur injection solution was allowed to cool to room temperature. For each shell growth, a calculated amount of a given precursor solution was injected with a syringe using standard air-free procedures. CdSe QDs (1·10⁻⁷M of 2.91 nm QDs), ODE (5.0 g) and ODA (1.5 g) were combined and heated up to 150 °C for 1 h to remove all toluene. The reaction temperature was increased to 240 °C and in steps with reaction periods of 30 minutes and precursors were added slowly to grow the cell half-monolayer by half-layer. Table A.1 below summarizes each step of the shell growth process.

Table A.1. Stepwise explanation of shell growth on CdSe QD seeds.

Step	Total # monolayers	Added Precursors	Amount (µL)
1	0.5	Cd + S	105
2	1	Cd + S	125
3	1.5	Cd + S	150
4	2	Cd + S	180
5	2.5	Cd + S	205
6	3	Cd + S	240
7	3.5	Cd + S	270
8	4	Cd + S	305
9	4.5	CdZn + S	345
10	5	CdZn + S	385
11	5.5	Zn + S	430
12	6	Zn + S	475

Following the synthesis of QDs, the reaction mixture was cooled to room temperature and diluted by adding 1 equivalent of hexane. The QDs were washed by adding 2 equivalents of methanol and collecting the upper hexane layer (coloured) and add 1 equivalent of acetone to precipitate the QDs. Finally, the nanocrystal seeds were re-dissolved in cyclohexane and stored inside a glove box under nitrogen atmosphere.

Additional Chemi-STEM maps and elemental quantifications **A.2**

All elemental quantifications were performed using the Cliff-Lorimer method with *k*-factors as implemented in the Bruker ESPRIT software.

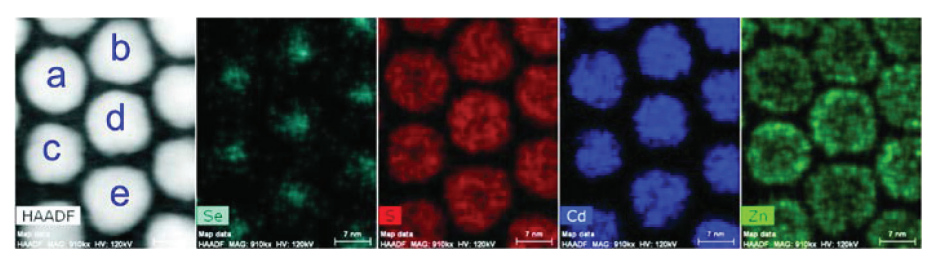


Figure A.1. HAADF-STEM image of CdSe-CdS-ZnS core-multishell QDs and corresponding Se, S, Cd and Zn elemental maps at initial state. Marked QDs were used for elemental quantification.

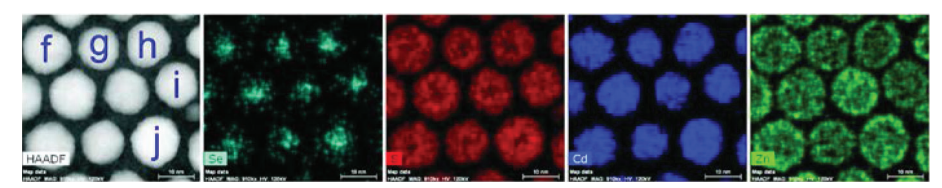


Figure A.2. HAADF-STEM image of CdSe-CdS-ZnS core-multishell QDs and corresponding Se, S, Cd and Zn elemental maps at initial state. Marked QDs were used for elemental quantification.

Table A.2. Elemental quantifications of QDs at initial state depicted with the letters (a-j) in Figure A.1 and A.2.

Atomic percentages					
	Zn	S	Cd	Se	cation/anion
a	11.07	45.39	41.13	2.41	1.09
b	10.57	46.59	39.39	3.45	0.99
С	18.74	46.35	32.91	2.00	1.06
d	14.66	47.91	34.94	2.49	0.98
e	11.18	48.81	37.83	2.17	0.96
f	10.86	48.87	37.83	2.44	0.94
g	10.65	48.85	37.64	2.86	0.93
h	9.68	46.70	40.65	2.98	1.01
i	8.70	49.25	39.69	2.35	0.93
j	10.85	46.41	39.49	3.25	1.01
Average	11.69	47.51	38.15	2.64	0.99
Std. Dev.	2.90	1.37	2.56	0.47	0.05

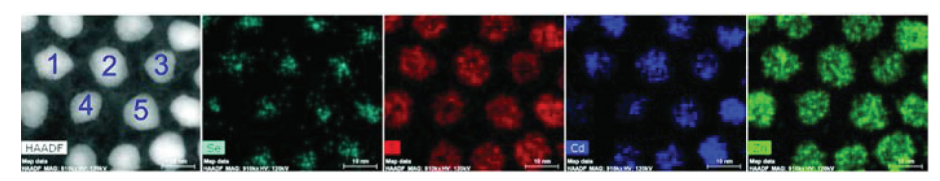


Figure A.3. HAADF-STEM image of QDs at heated state $(Cd_xZn_{1-x}Se-Cd_yZn_{1-y}S$ core-shell QDs) and corresponding Se, S, Cd and Zn elemental maps. Marked QDs were used for elemental quantification.

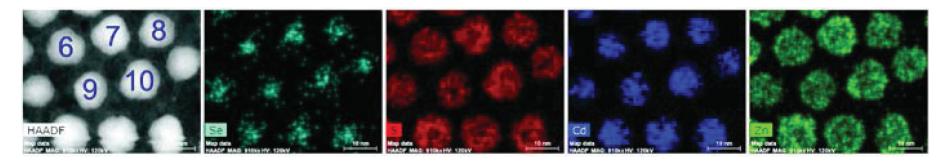


Figure A.4. HAADF-STEM image of QDs at heated state $(Cd_xZn_{1-x}Se-Cd_yZn_{1-y}S$ core–shell QDs) and corresponding Se, S, Cd and Zn elemental maps. Marked QDs were used for elemental quantification.

Table A.3. Elemental quantifications of QDs at heated state depicted with the numbers (1-10) in Figure A.3 and A.4.

Atomic percentages					
	Zn	S	Cd	Se	cation/anion
1	23.91	49.91	21.72	4.46	0.83
2	22.97	48.22	24.70	4.12	0.91
3	27.38	46.61	21.98	4.03	0.97
4	28.16	46.44	21.75	3.65	0.99
5	20.96	44.30	25.44	9.30	0.86
6	19.84	48.91	27.24	4.01	0.88
7	22.90	44.48	28.17	4.45	1.04
8	19.24	46.82	30.18	3.76	0.97
9	17.59	42.90	34.68	4.82	1.09
10	18.82	46.32	31.43	3.43	1.01
Average	22.17	46.49	26.72	4.60	0.96
Std. Dev.	3.57	2.17	4.44	1.70	0.08

References

- X. Peng, M. C. Schlamp, A. V. Kadavanich and A. P. Alivisatos, J. Am. Chem. Soc., 1997, 119, 7019. 1
- 2 R. Xie, U. Kolb, J. Li, T. Basché and A. Mews, *J. Am. Chem. Soc.*, 2005, 127, 7480.

Chapter 4

Core-shell reconfiguration in

Fe_xO/CoFe₂O₄ core/shell system

Abstract

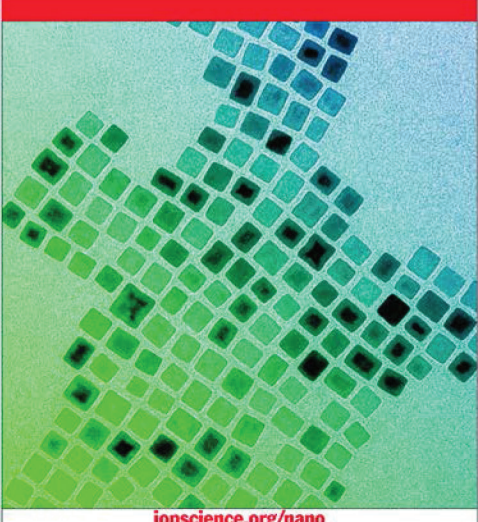
A large variety of single- and multi-component nanocrystals (NCs) can now be synthesized and integrated into nanocrystal superlattices. However, the thermal and temporal stability of these superstructures and their components can be a limiting factor for their application as functional devices. On the other hand, temperature induced reconstructions can also reveal opportunities to manipulate properties and access new types of nanostructures. *In-situ* atomically resolved monitoring of nanomaterials provides insight into the temperature induced evolution of the individual NC constituents within these superstructures at the atomic level. Here, we investigate the effect of temperature annealing on 2D square and hexagonal arrays of Fe_xO/CoFe₂O₄ core/shell NCs by *in-situ* heating in a transmission electron microscope (TEM). Both cubic and spherical NCs undergo a core-shell reconfiguration at a temperature of approximately 300 °C, whereby the Fe_xO core material segregates at the exterior of the CoFe₂O₄ shell, forming asymmetric dumbbells ("snowman-type" particles) with a small Fe_xO domain attached to a larger CoFe₂O₄ domain. Upon continued annealing, the segregated Fe_xO domains form bridges between the CoFe₂O₄ domains, followed by coalescence of all domains resulting in loss of ordering in the 2D arrays.

This chapter is based on the publication:

Yalcin, A.O. et al. Nanotechnology, 2014, 25, 055601.

- This publication has appeared on the journal cover as the featured article (*Nanotechnology* Volume 25, Issue 5).
- This publication has been selected to be featured in the 'Highlights of 2014' collection of the journal, in the 'Materials: synthesis or self-assembly' list.

NANOTECHNOLOGY



iopscience.org/nano

Featured article

Core-shell reconfiguration through thermal annealing in Fe_O/CoFe₂O₄ ordered 2D nanocrystal arrays A O Yalcin, B de Nijs, Z Fan, F D Tichelaar, D Vanmaekelbergh, A van Blaaderen, T J H Vlugt, M A van Huis and H W Zandbergen

IOP Publishing

4.1 Introduction

With the development of colloidal nanoscience, it has become possible to synthesize a plethora of single- and multi-component nanocrystals offering novel applications in chemistry, physics and materials science.¹⁻³ Metallic clusters and nanocrystals have been used in catalysis already for decades, as the NCs have a high density of active surface sites due to their large surface area to volume ratio. Semiconductor nanocrystals are for instance used in optoelectronic applications. Their radius is smaller than the exciton radius, which leads to strong quantum confinement and thereby to size-dependent opto-electrical properties.^{4,5}

In recent years, much effort has been devoted to colloidal heterosystems: systems that have two compounds (or more) and an interface in between. The presence of the two compounds (metals, semiconductors, magnets) together with the interface opens a tremendous amount of new degrees of freedom to tailor the physical properties. Colloidal particles with two semiconductor compounds can show delocalized excitons for which the life time and emission energy can be tailored, which is also important in lasing. 6 Compounds with a metallic/magnetic core and semiconductor shell are important in magneto-transport. Furthermore, FeO_x-type nanoparticles are also used for creating binary nanocrystal superlattices (BNSLs), displaying physical metaproperties. It has been shown that Au/FeO, binary superlattices can be used as catalysts for carbon monoxide (CO) oxidation,8 while magnetotransport properties have been demonstrated in Fe₃O₄/FePt superlattices.⁹

An often undesired property of such nanosystems, though, is their structural instability with respect to heating, even at temperatures far below the melting temperature of the bulk solids. This is of utmost importance as it may form a hurdle towards industrial applications of these systems, such as quantum dot solar cells, and core-shell NCs used for down conversion of light in light emitting diodes (LEDs). On the other hand, this could also be used in a beneficial way to manipulate the properties of such structures, such as in alloy formation at low temperatures, or even to make structures, otherwise not reachable. For example, it was previously shown that heating can transform ill-defined CdSe/Au interfaces in Au-tipped CdSe nanorods with crystallographically well-defined interfaces.¹⁰ Heating can also induce oriented attachment of NCs,11 which provides opportunities for making two dimensional semiconductor supercrystals. 12,13 In other cases, it was demonstrated that a combination of heating and irradiation can transform Au-tipped CdS nanorods into AuS/Cd core-shell NCs,14 and that heat induced transformation of PbSe/CdSe core/shell NCs into attached PbSe/CdSe bi-hemispheres, accompanied by drastic changes in optical properties.¹⁵

Understanding of the driving forces in these temperature induced structural conversions is limited until now. This also holds for the kinetics and atomic-scale motions during these conversions. One way to acquire more knowledge is by studying model systems using time resolved atomic resolution *in-situ* TEM.¹⁶ Here we study Fe_xO/CoFe₂O₄ core-shell nanoparticles as a model system for many complex oxides. It is a relevant system, because FeO_x-type nanoparticles are nowadays frequently used in the fabrication of binary superlattices.^{8,9,17-20} The advantage of this core-shell system is that it can be synthesized both in spherical and cubic morphologies,²¹ yielding hexagonal and square 2D superlattices, respectively. Furthermore, the crystal structures of the core and shell material have a good epitaxial fit by the small difference in lattice parameters.

Within the $Fe_xO/CoFe_2O_4$ core/shell NCs, the Fe_xO core is antiferromagnetic and the $CoFe_2O_4$ shell is ferromagnetic. ^{19,21-24} Magnetic dipolar interactions in these NCs are reported to have little effect on the superlattice formation. ¹⁹ As a bulk phase, the core material Fe_xO (x = 0.83-0.95)^{21,25} is only stable at high temperatures (it decomposes into α - Fe_2O_3 , γ - Fe_2O_3 and Fe_3O_4 below 560 °C), however as a nanocrystal, it is stable at room temperature. ^{21,22,26} The phase is named wüstite, and can be considered a rocksalt phase with a partially occupied cation sublattice. The shell material consists of $CoFe_2O_4$, and has a spinel crystal structure. The oxygen sublattices of Fe_xO and $CoFe_2O_4$ are identical and continuous over the interface, and therefore the $Fe_xO/CoFe_2O_4$ NCs are well-defined, atomically coherent core/shell systems.

Here, we investigate by means of *in-situ* heating experiments inside a transmission electron microscope (TEM) the thermal evolution of two superlattices of Fe_xO/CoFe₂O₄ core/shell NCs, one being a square array of cubic particles and another being a hexagonal array consisting of spherical particles. In both cases, a striking morphological transformation takes place whereby the Fe_xO core leaves the shell structure and segregates at the exterior of the shell.

4.2 Methods

4.2.1 Synthesis of spherical and cubic NCs

For synthesis of the $Fe_xO/CoFe_2O_4$ NCs the method proposed in $Ref.^{27}$ was used. For a typical NC synthesis, a precursor mixture was prepared by combining 8.66 g $FeCl_3 \cdot 4H_2O$ (32 mmol, Sigma Aldrich, 99%) dissolved in 80 ml methanol (Sigma Aldrich, absolute, MeOH) with 2.0 g $CoCl_2$ (16 mmol, Sigma Aldrich, > 98%) dissolved in 40 ml MeOH. 40.2 g oleic acid (Aldrich, 90%, OA) was added to the mixture. Next, 5.12 g sodium hydroxide (Acros Organics pellets, extra pure) dissolved in 320 ml MeOH was slowly added to the mixture. The resulting brown viscous liquid was retrieved by decanting and washed three times with MeOH. The mixture was

dissolved in 80 ml hexane (Aldrich, mixture of isomers), separated using a separatory funnel and washed three times using warm (40 °C) de-ionized water (Millipore Direct-Q UV3). The concentration was determined gravimetrically by drying 1 ml of the solution. The solution was diluted to a concentration of 0.5 mol kg⁻¹ by adding 1.48 g octadecene (Sigma Aldrich, 90%, ODE) for each gram of mixed oleate, and the hexane was removed by evaporation. For a typical synthesis of spherical core shell NCs, 9.6 g precursor solution, 0.76 g OA and 13.70 g ODE were combined and heated to reflux temperature for 40 minutes under nitrogen. The resulting NCs were isolated by adding 20 ml ethanol (100%, ETOH) and 15 ml of hexane and centrifugation at 4000 rpm for 3 hours (using a Hettich Zentrifugen Rotina 46 s), and redispersed in cyclohexane (Sigma-Aldrich, ≥ 99.8%). For a typical synthesis of cubic core shell NCs, 9.6 g precursor solution, 0.76 g OA, 1.46 g sodium oleate (ABCR, 95%) and 12.50 g ODE were combined and heated to reflux temperature for 40 minutes, the resulting NCs were isolated by adding 15 ml of hexane and 20 ml of ETOH and centrifugation at 4000 rpm for 3 hours, and redispersed in cyclohexane. The NC suspensions were stored under Ar atmosphere.

4.2.2 In-situ TEM studies

High resolution TEM (HRTEM) with aberration correction was used for the imaging to resolve the atomic lattices and study the orientation relationship between the various nanoscale domains. High-angle annular dark field scanning transmission electron microscopy (HAADF-STEM) does not suffer from intensity changes caused by diffraction contrast, and was used to distinguish with more certainty between the Fe_vO and CoFe₂O₄ domains. In this imaging mode, the intensity scales with Z² (so-called Z-contrast), where Z is the atomic number of the element. Because of the higher density of the Fe₂O phase with respect to the CoFe₂O₄ phase, the Fe_vO phase appears brighter in the images. Finally, energy-filtered TEM (EFTEM) studies were conducted in order to perform not only density-based imaging, but also chemical mapping of the Co content, whereby the images are energy-filtered by setting an energy window over the characteristic Co peak in the electron energy loss spectrum (EELS).

For TEM studies, 8 µl of solution was dropcast onto a MEMS micro-hotplate (microelectronic mechanical system) inside the glove box. More information about the micro-hotplate and its application in TEM studies can be found in Ref.¹⁶ After the micro-hotplate was mounted in a dedicated TEM specimen holder, this set-up was plasma cleaned for 15 seconds in order to remove excess solution residues. A Cs aberration corrected FEI Titan microscope operating at 300 kV accelerating voltage was used in in-situ heating experiments and in HAADF-STEM imaging. EFTEM studies were carried out with FEI Monochromated Tecnai F20ST.

4.3 Results

Figure 4.1 shows the square (Figure 4.1a) and hexagonal (Figure 4.1b) 2D arrays of cubic and spherical $Fe_xO/CoFe_2O_4$ core/shell NCs respectively. For the superlattice shown in Figure 4.1a, the {100} atomic lattices were aligned with the axes of the 2D array, which was a direct result of the crystallographic {100} facets that were facing each other. In the case of spherical $Fe_xO/CoFe_2O_4$ NCs shown in Figure 4.1b, there was no such facet alignment. Figure 4.2 shows the overall cubic $Fe_xO/CoFe_2O_4$ core/shell NC arrays and HRTEM images of single core/shell NCs. The Fe_xO core has a rock salt structure with some cation deficiencies (x = 0.83-0.95)^{21,25} and the lattice constant varies between 4.255 Å and 4.294 Å depending on the oxidation state. The {200} planar distance of Fe_xO was measured as 2.1 Å, consistent with the rock salt structure. The $CoFe_2O_4$ shell has a spinel crystal structure (lattice constant 8.46 Å). Both structures have a face centered cubic (FCC) oxygen sublattice with a lattice mismatch of only 3%. The {100} surfaces of the NCs were mutually aligned, resulting in a square 2D array.

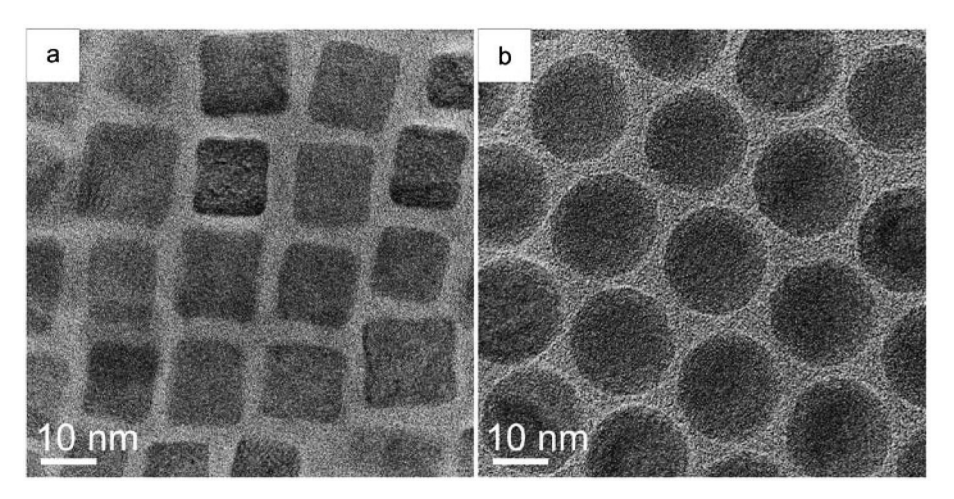


Figure 4.1. TEM images of different types of 2D arrays. (a) cubic $Fe_xO/CoFe_2O_4$ core/shell NCs forming a square 2D array, (b) spherical $Fe_xO/CoFe_2O_4$ core/shell NCs forming a hexagonal 2D array.

As the crystal structures of core and shell materials are similar, an objective aperture was inserted to enhance the diffraction contrast (Figure 4.2a and 4.2b). The Fe_xO core material exhibited darker contrast compared to the $CoFe_2O_4$ shell material in the diffraction contrast images. The diffraction contrast effect is demonstrated more systematically for a single NC in Figure B.1 in Appendix B. In Figure 4.2a and 4.2b, the core and the shell cannot be distinguished in all the nanocubes since the (diffraction) contrast between the shell and the core depends sensitively on the crystal orientation with respect to the electron beam. As the NCs were not all exactly in

the same orientation, the core-shell contrast was not always visible, which was also observed in earlier studies on a very similar system (Fe_xO/Fe₃O₄ wüstite/spinel NCs). ^{25,29}

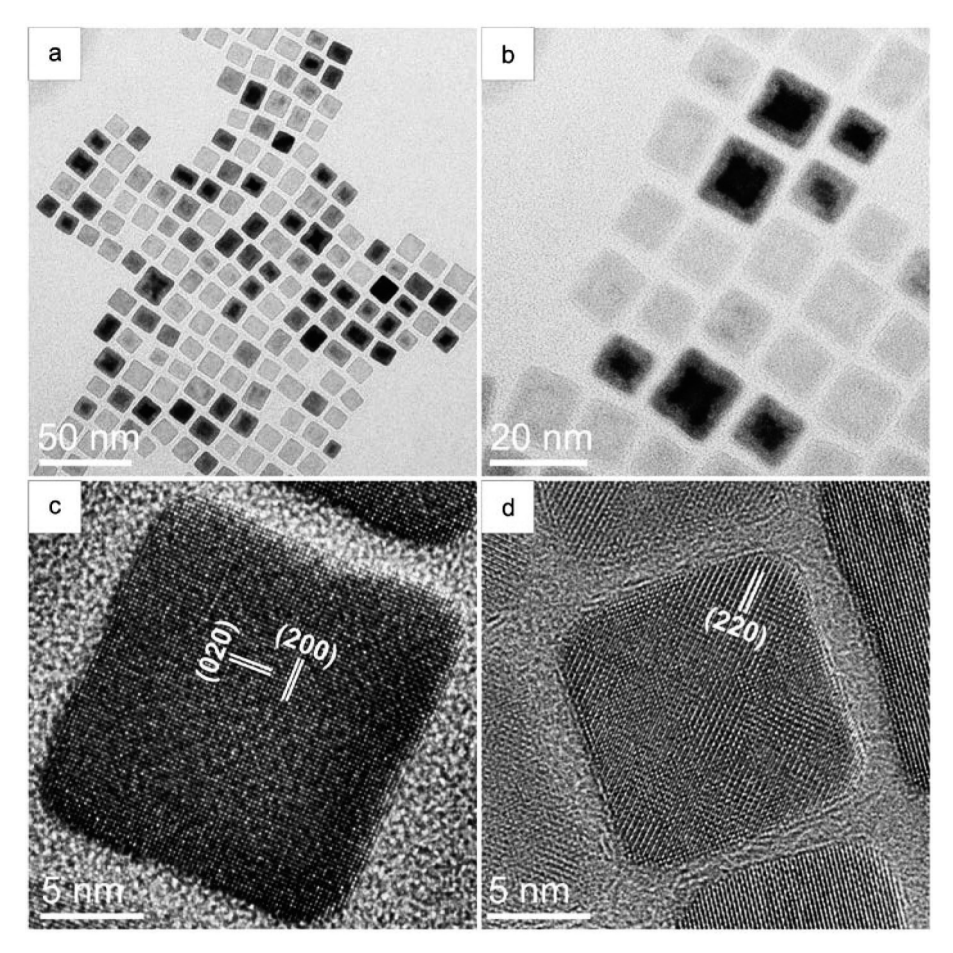


Figure 4.2. (a and b) TEM images (diffraction contrast) of 2D square arrays consisting of cubic Fe₂O/CoFe₂O₄ core/shell NCs. An objective aperture was inserted to enhance the diffraction contrast between the Fe_xO and the CoFe₂O₄ materials. (c and d) HRTEM images of cubic core/shell NCs. The observed lattice spacings were 2.1 Å, corresponding to (200) lattice spacing of the Fe_xO core and 3.0 Å corresponding to (220) lattice spacing of the CoFe₂O₄ shell.

Figure 4.3 shows the square array at 100 °C and 135 °C. It is clear from the images that during heating some NCs changed their alignment with respect to the electron beam, so that in certain cases the core-shell contrast appeared (indicated with white arrow in Figure 4.3a and 4.3b while in other cases it disappeared (indicated with black arrow in Figure 4.3a and 4.3b).

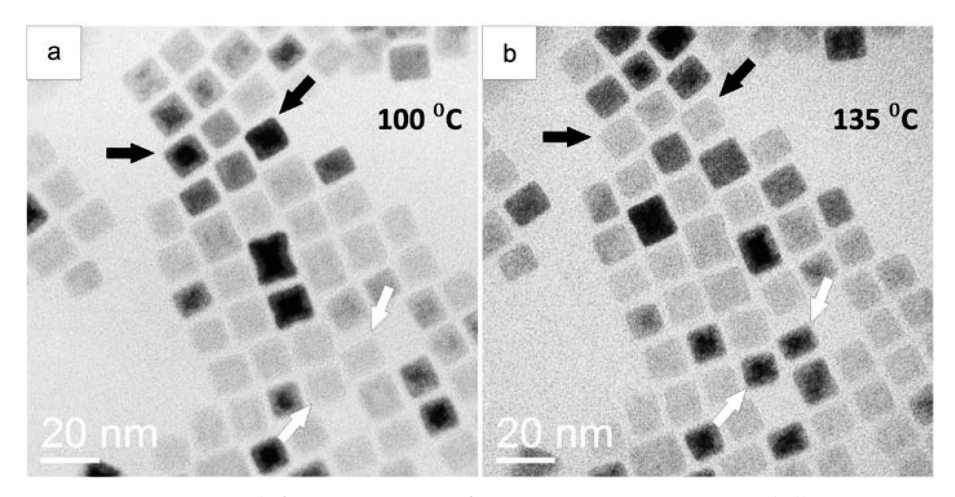


Figure 4.3. TEM images (diffraction contrast) of a square Fe_xO/CoFe₂O₄ core/shell 2D NC array at (a) 100 °C and (b) 135 °C. The black arrows show NCs whereby the core could be distinguished at 100 °C while it could no longer be distinguished at 135 °C. The white arrows show NCs where the opposite occurred.

With a heating rate of 10 degrees/minute, a reconfiguration of the core and shell materials was observed at a temperature of 300 °C, as shown in Figure 4.4. The hexagonal arrays exhibited reconfiguration at a slightly higher temperature (320 °C) than the square arrays. During the reconfiguration, the Fe_xO core material left the CoFe₂O₄ shell in both square and hexagonal NC arrays and segregated at the exterior of the shells, thereby forming asymmetric dumbbells ("snowman-type" particles). Subsequently, Fe_xO domains formed bridges between the CoFe₂O₄ materials as shown in Figure 4.4a. The CoFe₂O₄ shells of cubic NCs also underwent a slight reconfiguration in which they became more rounded at the edges. Eventually also these domains coalesced at higher temperatures, resulting in loss of ordering of the 2D NC arrays. The reconfiguration was observed subsequently at other regions (not previously in the field of view) on the substrate, therefore it can be concluded that the electron beam does not have a strong influence on the reconfiguration or the reconfiguration temperature. More images showing the reconfiguration of NCs at different locations can be found in Figure B.2 and B.3 in Appendix B.

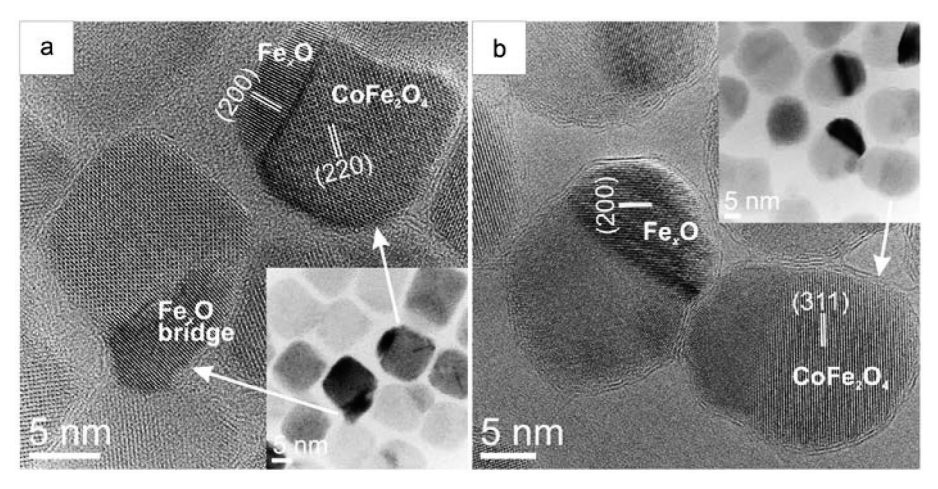


Figure 4.4. TEM images of Fe₂O/CoFe₂O₄ 'initially' core/shell NC arrays. (a) cubic NCs at 335 °C, and (b) spherical NCs at 360 °C. The insets in the images were taken when the objective aperture was inserted (diffraction contrast). The (200) spacing of Fe₂O is 2.1 Å, and (220) and (311) spacings of CoFe₂O₄ are 3.0 Å and 2.55 Å respectively.

High Angle Annular Dark Field Scanning Transmission Electron Microscopy (HAADF-STEM) studies confirmed the reconfiguration of these NCs. In HAADF-STEM studies, collection angle above 30 mrad exhibits Z-contrast imaging and diffraction effects can be minimized.³⁰ Thus, a small camera length (183 mm) was employed to ensure that electrons scattered beyond 30 mrad were used in HAADF-STEM studies. 31,32 In the CoFe₂O₄ structure, 75% of the cation sites are occupied and in the case of Fe.O structure, 83% to 95% of the cation sites are occupied.^{21,25} As a result, the Fe_xO structure exhibited brighter contrast in comparison to CoFe₂O₄ in the HAADF-STEM images. Figure 4.5 shows cubic NCs during heating. The insets show the intensity profiles along the white rectangles in HAADF-STEM images. From room temperature (RT) to 300 °C (Figure 4.5b), the NCs became rounded, showing that the morphology of the CoFe₂O₄ shell also changed. In the NC indicated with a white arrow in Figure 4.5, the Fe_xO contrast was apparent initially (inset in Figure 4.5a) and core-shell contrast was lost with increasing temperature (Figure 4.5b-4.5f). At 350 °C (Figure 4.5d), the Fe_xO -most likely from two cores- formed a bridge with the neighbouring NC. The smooth intensity profiles along the NC at elevated temperatures (Figure 4.5d-4.5f) suggest that the CoFe₂O₄ shell material filled up the core volume during reconfiguration. The NC shape became more irregular at temperatures above 380 °C (Figure 4.5e and 4.5f).

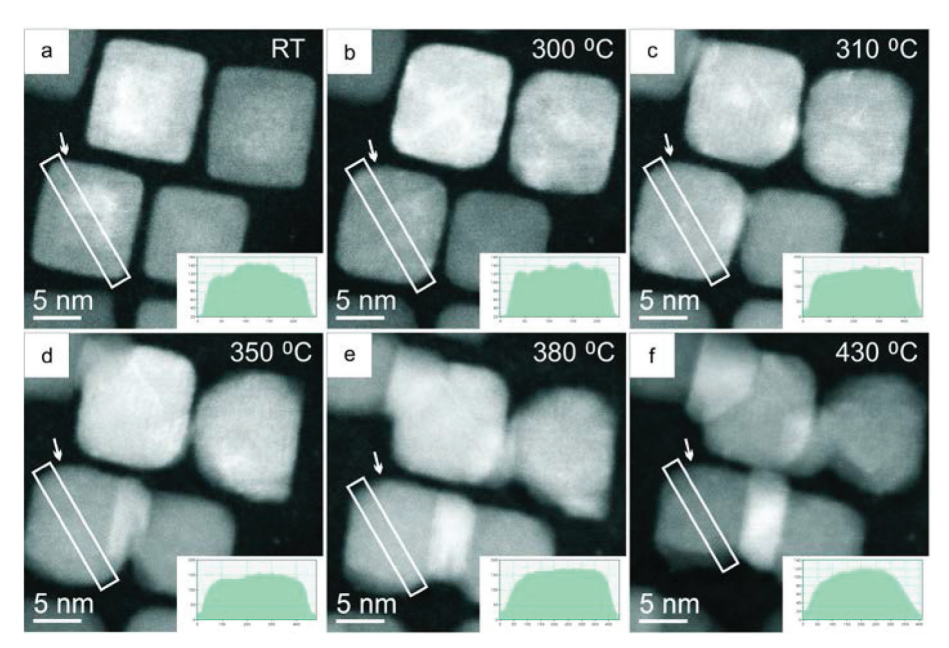


Figure 4.5. HAADF-STEM images of cubic $Fe_xO/CoFe_2O_4$ NCs. The insets are intensity profiles taken from the white rectangles in the images. (a) NCs at room temperature (RT) before reconfiguration. Fe_xO core exhibited brighter contrast compared to $CoFe_2O_4$ shell. (b-f) NCs at 300 °C, 310 °C, 350 °C, 380 °C and 430 °C respectively. The cubic NCs became rounded and the intensity variation at the core region was lost (Figure 4.5b-4.5f), suggesting filling of the core volume by the $CoFe_2O_4$ shell material. The NC shape became more irregular at temperatures above 380 °C (Figure 4.5e and 4.5f). HAADF-STEM images were taken with a camera length of 183 mm and a dwell time of 130 μs.

Energy Filtered TEM (EFTEM) studies in Figure 4.6 showed that heated Fe_xO domains contained Co as well. Prior to the EFTEM experiments, initially spherical NCs were further heated to 530 °C to obtain bigger domains of Fe_xO and CoFe₂O₄. With elemental mapping of Co (L_{2,3} edge at 779 eV), the domains containing Co gave contrast. Figure 4.6a and 4.6c are unfiltered Bright Field Transmission Electron Microscopy (BFTEM) images and Figure 4.6b and 4.6d are the corresponding Co maps respectively. Dotted lines were used to emphasize the Fe_xO domains (dark contrast in unfiltered BFTEM images). The arrows show Fe_xO domains with Co presence (weak contrast in Co maps). In a recent study, Sytnyk *et al.*³³ showed that Co can diffuse in the Fe_xO wüstite structure, which explains the weak contrast of the Fe_xO domains in the Co maps. Note that annealing at an elevated temperature (530 °C) can also play a role in the presence of Co in the Fe_xO domains as temperature enhances the solubility and diffusivity of species.

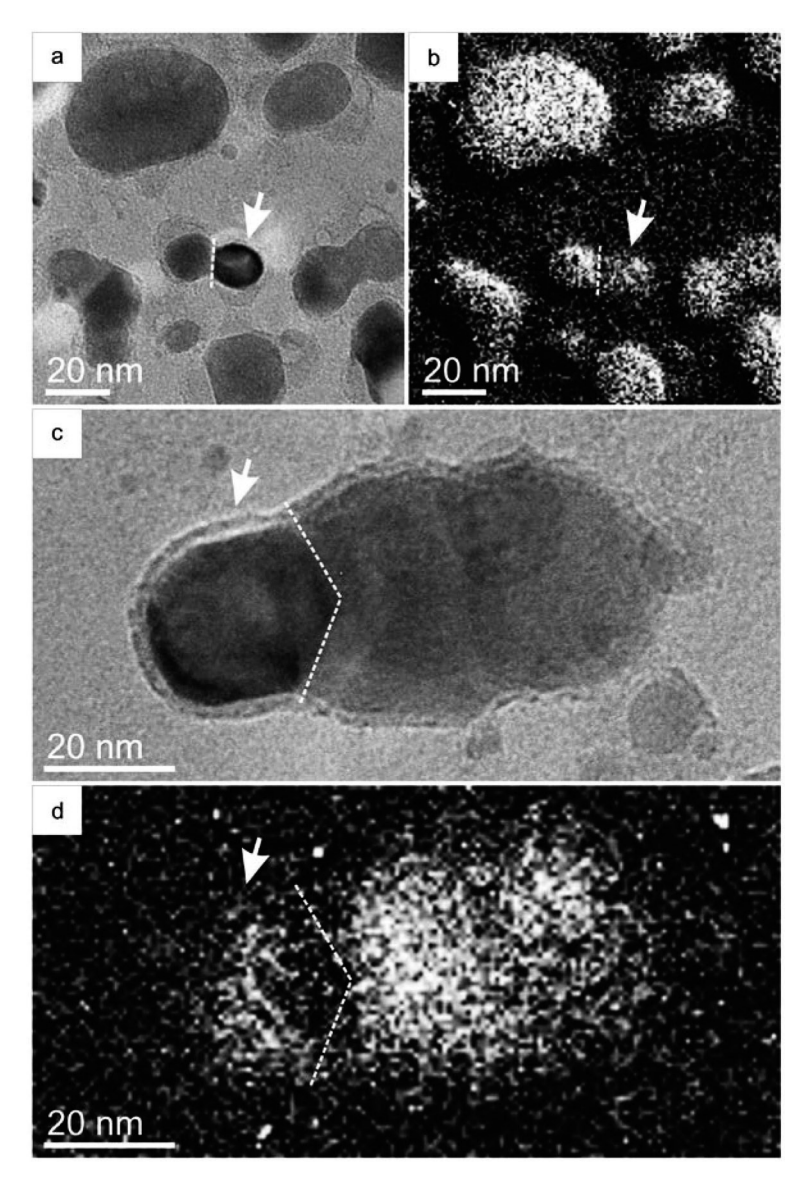


Figure 4.6. EFTEM Co-mapping of initially spherical NCs. The structure was heated to 530 °C to have bigger domains of individual species. Figure 4.6a and 4.6c are unfiltered BFTEM images and Figure 4.6b and 4.6d are the corresponding Co maps of them respectively. L23 edge of Co is at 779 eV. Fe_vO domains exhibited dark contrast in unfiltered BFTEM images. The dotted lines were used to clarify these domains. EFTEM studies revealed that heated Fe_xO domains contained Co. Arrows show the Fe_xO domains with Co presence. A slit width of 20 eV was used in the EFTEM studies.

4.4 Discussion

In the synthesis of the spherical core/shell NCs, oleic acid was used as the main ligand, while in the case of cubic core/shell NCs, a mixture of sodium oleate and oleic acid was used.²¹ It has been reported that the presence of sodium oleate hinders the growth rate in the <100> direction, and as a result the cubic shape is favoured over spherical.²¹ In cubic core/shell NCs, the surfaces consist of {100} facets, and individual NCs can easily align their {100} facets with respect to each other, resulting into the formation of a square 2D array. Spherical NCs with mostly hard interactions tend to form cubic (FCC) and hexagonal superlattices,²⁴ whereby magnetic NCs prefer a hexagonal superlattice,³⁴ but can also form body-centered tetragonal superlattices.³⁵

The reconfiguration in cubic NCs starts at 300 °C and in spherical NCs at a slightly higher temperature (320 °C). Ayyappan et al.36 observed (through mass spectroscopy under Ar atmosphere) that oleic acid ligands remain attached to the CoFe₂O₄ NCs up to a temperature of 420 °C, which is higher than the reconfiguration temperature we found. During reconfiguration, the HAADF-STEM and EFTEM images (Figure 4.5 and 4.6) suggest that Co²⁺ cations diffuse from the shell to the core. Hence, Fe cations (valence Fe²⁺ in Fe_{*}O and Fe³⁺ in CoFe₂O₄) diffuse to the sides of the NC. The excess of Fe cations in the shell material eventually leads to segregation of Fe₂O domains towards the sides of the NCs. As the core and shell materials have FCC anion (oxygen) sublattice with a lattice mismatch of only 3%, 21, 25 the oxygen sublattice at the core remains unaffected initially, although displacements of O atoms do occur later with the formation of the Fe₂O side domains. The ligands attached to the shell material can play a role in the stabilization of the overall shape during initial stages of the reconfiguration, thus only slight rounding at the edges is observed (Figure 4.5b and 4.5c). Further annealing, probably accompanied by loss of the ligands eventually leads to agglomeration (Figure 4.5d-4.5f and Figure 4.6) whereby the 2D ordering in the NC arrays is lost. It is also important to note the presence of Co traces in Fe_vO domains (Figure 4.6) at an elevated temperature (530 °C), which is probably triggered by temperature enhanced diffusivity. The electron beam does not have a substantial effect on the reconfiguration behavior or the reconfiguration temperature as this phenomenon was observed everywhere on the substrate.

It is clear that the asymmetric dumbbell ("snowman-type" particle) arrangement with the Fe_xO domain at the exterior of the $CoFe_2O_4$ shell constitutes a lower energy configuration than the core-shell one present before annealing. As a first approximation (neglecting nanosize effects, edge and corner effects, magnetic effects), the total free energy G of the system can be written as:

$$G = \sum g_i^{bulk} V_i + \sum \gamma_{ij} A_{ij} \tag{4.1}$$

whereby g_i^{bulk} is the Gibbs free energy per unit volume of bulk phase i, and γ_{ij} is the interface energy or surface tension at any interface between media i and j, including solid-solid, solidligand, and any interface with gas or vacuum.

Considering this energy balance in view of the experimentally observed core-shell reconfiguration, we note that (1) a Fe₂O surface is created where it did not exist beforehand; (2) the interfacial area between Fe₂O and CoFe₂O₄ is strongly reduced; and (3) the surface area of CoFe₂O₄ has changed: it decreased at the exterior where the Fe_vO domain is now attached. It seems likely that the decrease in the interfacial area between Fe,O and CoFe,O4 together with the decrease in the surface area of CoFe₂O₄ brings a lower total energy despite the creation of a Fe_xO surface. A very similar transformation was found previously for PbSe/CdSe core/shell particles, which transformed into PbSe/CdSe bi-hemispheres.¹⁵

The core/shell reconfiguration in the NCs as well as the loss of ordering in the 2D arrays raise concerns about the application of these NCs in possible devices. The current results indicate that the thermal stability (and thus also the temporal stability) of these NC arrays is limited. Considering their chemical stability, it has been reported that for a similar structure of cubic Fe₂O/Fe₃O₄ core/shell NCs, air oxidation at room temperature leads to transformation of the Fe_xO wüstite core to the spinel Fe₃O₄ structure.²⁵ In addition, annealing CoFe₂O₄ NCs at 400-500 °C in a gas atmosphere (mixture of 93% Ar and 7% H₂) leads to reduction of NCs to FeCo domains.37

Considering possible implementation of this system in a device/application, the exchange bias effects between antiferromagnetic Fe_xO core and ferromagnetic CoFe₂O₄ shell material are of critical importance. 21,25,33 The Néel temperature (T_N) of Fe_xO lies around 200 K and the blocking temperature (T_B) of Fe_xO/CoFe₂O₄ core/shell NC system can vary between 160-165 K, making this system superparamagnetic at room temperature.^{21,24,38} In fact, the blocking temperature depends on the size of the nanocrystal as well as the volumetric ratios of core and shell material. 25,38 Therefore, the magnetic properties of this system can be manipulated through adjusting the NC size and the core-shell volume fractions. NCs after reconfiguration by thermal annealing can exhibit different exchange bias properties from the original core/ shell system through Fe_xO bridge formation between separate NC domains (Figure 4.4a) as well as through core volume filling by the shell material (Figure 4.5), and therefore the heating of nanocrystal arrays could be explored as a new technique for manipulation of the magnetic properties for future applications.

4.5 Conclusions

The thermal stability of Fe_xO/CoFe₂O₄ core/shell NCs ordered in 2D arrays was investigated by *in-situ* heating experiments using TEM. Square 2D arrays of cubic NCs and hexagonal 2D arrays of spherical NCs were investigated. In both systems, a core-shell reconfiguration takes place at a temperature of approximately 300 °C. HRTEM, HAADF-STEM and EFTEM studies confirm that the Fe_xO core material segregates in a domain outside the CoFe₂O₄ shell, thereby forming anisotropic asymmetric dumbbells ("snowman-type" particles) having a well-defined interface. During reconfiguration, the CoFe₂O₄ shell material fills up the core volume and the cubic NCs become more rounded. Upon continued annealing, the segregated Fe_xO domains form bridges between the CoFe₂O₄ domains, followed by further agglomeration of all domains and loss of ordering in the 2D NC arrays. Annealed Fe_xO domains contain Co traces as well. Most likely, the energy gain associated with the decrease in interfacial area is the driving force behind the transformation.

References

- Yin Y and Alivisatos A P 2005 Nature 437 664-670. 1
- 2 Cozzoli P D, Pellegrino T and Manna L 2006 Chem. Soc. Rev. 35 1195-1208.
- 3 de Mello Donegá C 2011 Chem. Soc. Rev. 40 1512-1546.
- 4 Alivisatos A P 1996 Science 271 933-937.
- 5 Klimov V I, Mikhailovsky A A, Xu S, Malko A, Hollingsworth J A, Leatherdale C A, Eisler H -J and Bawendi M G 2000 Science 290 314-317.
- 6 Klimov V I, Ivanov S A, Nanda J, Achermann M, Bezel I, McGuire J A and Piryatinski A 2007 Nature 447 441-446.
- Lee J S, Bodnarchuk M I, Shevchenko E V and Talapin D V 2010 J. Am. Chem. Soc. 132 6382-6391.
- 8 Kang Y et al. 2013 J. Am. Chem. Soc. 135 1499-1505.
- Dong A, Chen J, Vora P M, Kikkawa J M and Murray C B 2010 Nature 466 474-477. 9
- Figuerola A, van Huis M, Zanella M, Genovese A, Marras S, Falqui A, Zandbergen H W, Cingolani 10 R and Manna L 2010 Nano Lett. 10 3028-3036.
- 11 van Huis M A, Kunneman L T, Overgaag K, Xu Q, Pandraud G, Zandbergen H W and Vanmaekelbergh D 2008 Nano Lett. 8 3959-3963.
- Schliehe C et al. 2010 Science 329 550-553. 12
- Evers W H, Goris B, Bals S, Casavola M, de Graaf J, van Roij R, Dijkstra M and Vanmaekelbergh 13 D 2013 Nano Lett. 13 2317-2323.
- van Huis M A, Figuerola A, Fang C, Béché A, Zandbergen H W and Manna L 2011 Nano Lett. 11 14 4555-4561.
- 15 Grodzińska D, Pietra F, van Huis M A, Vanmaekelbergh D and de Mello Donegá C 2011 J. Mater. Chem. 21 11556-11565.
- 16 van Huis M A, Young N P, Pandraud G, Creemer J F, Vanmaekelbergh D, Kirkland A I and Zandbergen H W 2009 Adv. Mater. 21 4992-4995.
- 17 Talapin D V, Shevchenko E V, Bodnarchuk M I, Ye X, Chen J and Murray C B 2009 Nature 461 964-967.
- 18 Redl F X, Cho K -S, Murray C B and O'Brien S 2003 Nature 423 968-971.
- Bodnarchuk M I, Kovalenko M V, Pichler S, Fritz-Popovski G, Hesser G and Heiss W 2009 ACS 19 Nano 4 423-431.
- 20 Shevchenko E V, Talapin D V, Kotov N A, O'Brien S and Murray C B 2006 Nature 439 55-59.
- Bodnarchuk M I, Kovalenko M V, Groiss H, Resel R, Reissner M, Hesser G, Lechner R T, Steiner 21 W, Schäffler F and Heiss W 2009 Small 5 2247-2252.
- 22 Glaria A, Kahn M L, Chaudret B, Lecante P, Casanove M - J and Barbara B 2011 Mater. Chem. Phys. 129 605-610.
- 23 Vanmaekelbergh D 2011 Nano Today 6 419-437.

- 24 Bodnarchuk M I, Kovalenko M V, Heiss W and Talapin D V 2010 J. Am. Chem. Soc. 132 11967-11977.
- 25 Pichon B P et al. 2011 Chem. Mater. 23 2886-2900.
- 26 Yin M, Chen Z, Deegan B and O'Brien S 2007 J. Mater. Res. 22 1987-1995.
- 27 Kovalenko M V, Bodnarchuk M I, Lechner R T, Hesser G, Schäffler F and Heiss W 2007 *J. Am. Chem. Soc.* 129 6352-6353.
- 28 Song Q and Zhang Z J 2004 J. Am. Chem. Soc. 126 6164-6168.
- 29 Hai H T, Yang H T, Kura H, Hasegawa D, Ogata Y, Takahashi M and Ogawa T 2010 *J. Colloid Interface Sci.* 346 37-42.
- Weyland M, Thomas J M, Dunin-Borkowski R E and Midgley P A 2001 *Inst. Phys. Conf. Ser.* 168 107-110 (EMAG 2001).
- 31 Grieb T, Müller K, Fritz R, Schowalter M, Neugebohrn N, Knaub N, Volz K and Rosenauer A 2012 *Ultramicroscopy* 117 15-23.
- 32 Grieb T, Müller K, Fritz R, Grillo V, Schowalter M, Volz K and Rosenauer A 2013 *Ultramicroscopy* 129 1-9.
- 33 Sytnyk M et al. 2013 Nano Lett. 13 586-593.
- 34 Talapin D V, Shevchenko E V, Murray C B, Titov A V and Král P 2007 Nano Lett. 7 1213-1219.
- Disch S, Wetterskog E, Hermann R P, Salazar-Alvarez G, Busch P, Brückel T, Bergström L and Kamali S 2011 Nano Lett. 11 1651-1656.
- 36 Ayyappan S, Panneerselvam G, Antony M P and Philip J 2011 Mater. Chem. Phys. 130 1300-1306.
- 37 Poudyal N, Chaubey G S, Rong C -B, Cui J and Liu J P 2013 Nanotechnology 24 345605.
- 38 Hai H T, Kura H, Takahashi M and Ogawa T 2011 J. Phys. Conf. Ser. 266 012127.

Appendix B

Appendix B contains TEM images of a single NC showing the core-shell contrast is visible when objective aperture is inserted. Moreover, additional TEM images of reconfigured NCs are included.

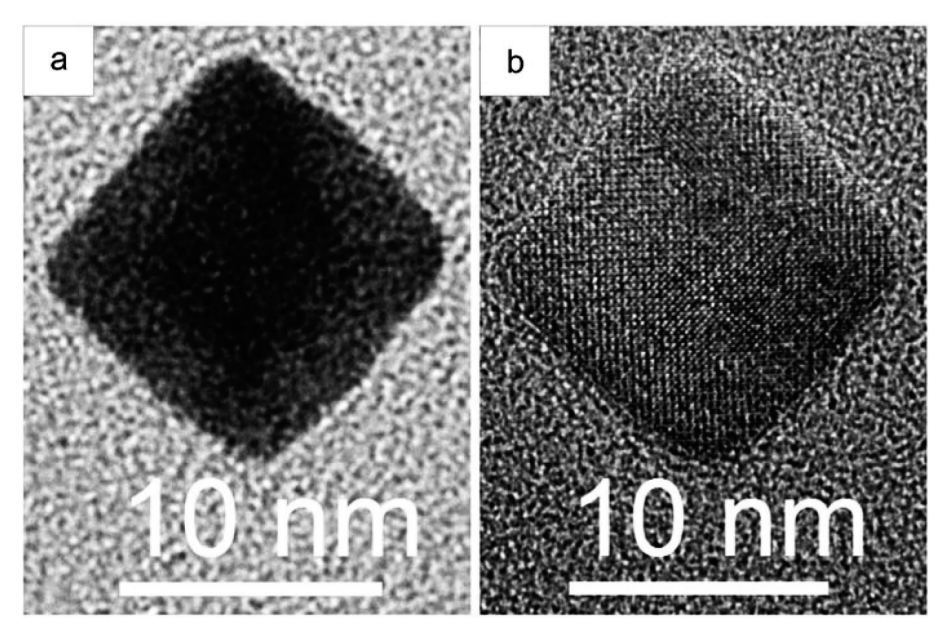


Figure B.1. TEM images of Fe_xO/CoFe₂O₄ core/shell NC with, (a) objective aperture inserted, (b) objective aperture out. The core-shell contrast is better observed with diffraction contrast.

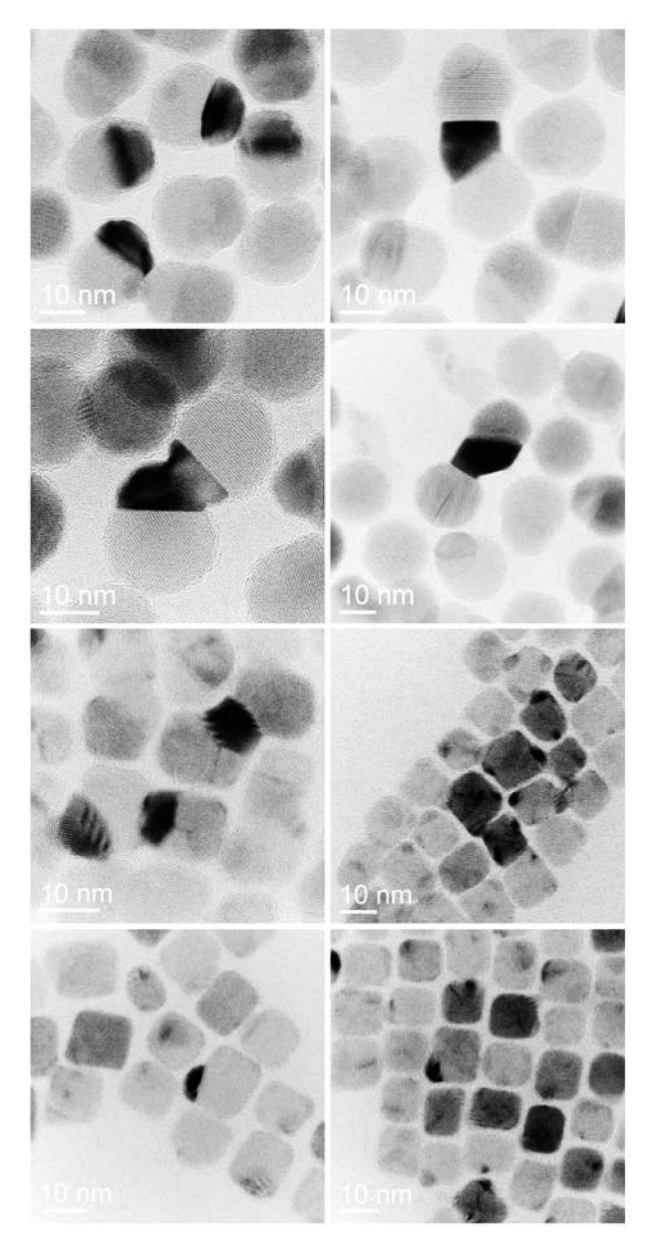


Figure B.2. TEM images (diffraction contrast) of spherical and cubic NCs during temperature annealing. The Fe_xO core (dark contrast in the images) segregates at the exterior of $CoFe_2O_4$ shell and the individual NCs connect through the segregated Fe_xO NCs with each other. As a result, the ordered 2D array is lost.

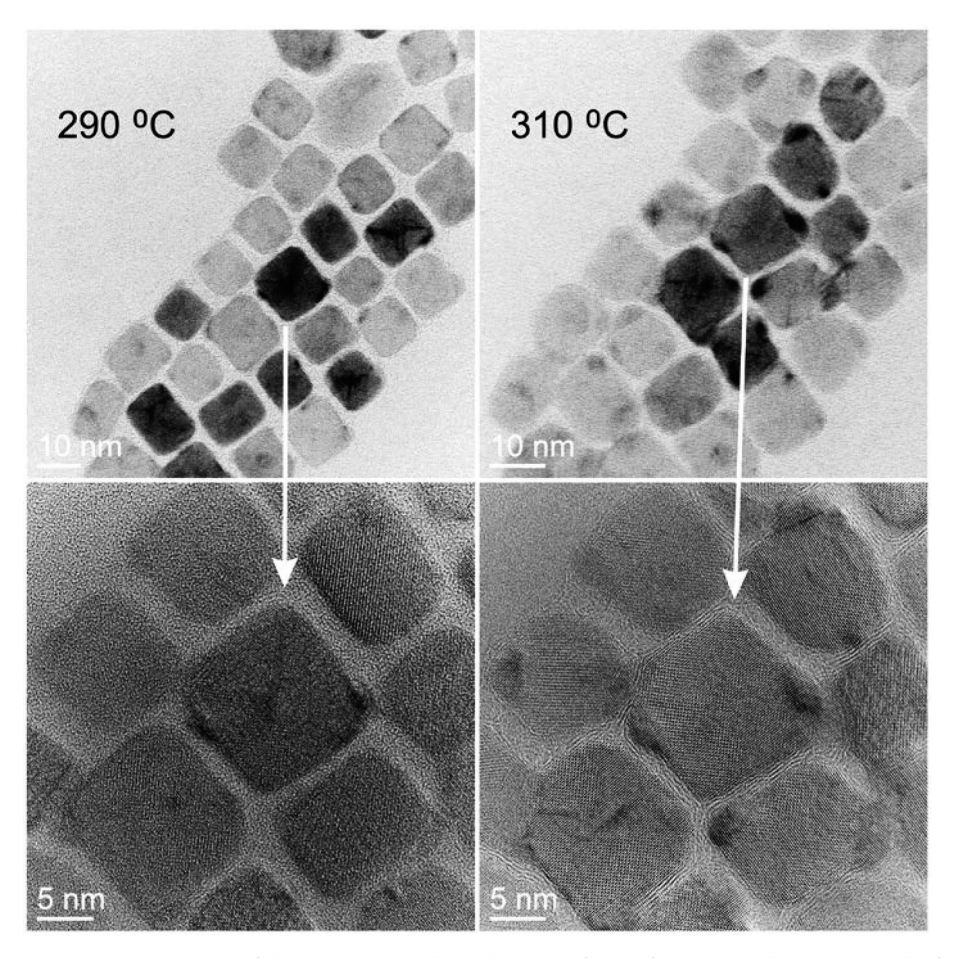


Figure B.3. TEM images of the starting and the end stages of reconfiguration. The images in the first row are with diffraction contrast.

Chapter 5

Cation exchange and solid–solid–vapor (SSV) growth in CdSe-PbSe dumbbell system

Abstract

Here, we show a novel solid–solid–vapor (SSV) growth mechanism whereby epitaxial growth of heterogeneous semiconductor nanowires takes place by evaporation induced cation exchange. During heating of PbSe-CdSe nanodumbbells inside a transmission electron microscope (TEM), we observed that PbSe nanocrystals grew epitaxially at the expense of CdSe nanodomains driven by evaporation of Cd. Analysis of atomic-resolution TEM observations and detailed atomistic simulations reveals that the growth process is mediated by vacancies.

This chapter is based on the publication:

Yalcin, A.O. et al. Nano Lett., 2014, 14, 3661-3667.

This publication has been selected to be featured in ACS (American Chemical Society)
 Editors' Choice.







5.1 Introduction

Both the synthesis and design of heteronanocrystals (HNCs) have undergone a rapid development, whereby PbSe and CdSe NCs are key materials acting as functional building blocks within a wide variety of heterogeneous nanostructures.¹⁻⁸ PbSe-CdSe HNCs are of particular interest as they can exhibit properties different from individual PbSe and CdSe dots. The presence of two semiconductor quantum dots connected via a well-defined interface opens new possibilities for tailoring the opto-electronic properties. 1,4-7,9 Heat treatment of HNCs can induce new interface designs, 5,10-13 exemplified by the transformation of PbSe/CdSe core/shell systems into PbSe-CdSe bihemispheres.⁵ Here, we report an *in-situ* heat induced epitaxial PbSe NC domain growth at the solid-solid PbSe-CdSe nanointerface through cation exchange. We show that Pb replaces Cd at the PbSe/CdSe interface, resulting in growth of the PbSe phase at the expense of the CdSe phase. The incorporated Pb is originating from Pb-oleate present as excess stabilizer at the surface of the mature PbSe/CdSe HNCs.

Vapor-liquid-solid (VLS)¹⁴⁻¹⁶ and vapor-solid-solid (VSS)^{17,18} growth mechanisms are nowadays commonly applied in nanochemistry to epitaxially grow semiconductor nanowires from the elements dissolved in a liquid (VLS) or solid (VSS) domain. In analogy with these growth mechanisms, the currently observed process could be called solid-solid-vapor (SSV) growth as the Cd evaporates, either as neutral Cd atoms or in a molecular complex such as Cd-oleate.

5.2 **Results & Discussion**

Figure 5.1a shows an HAADF-STEM (High Angle Annular Dark Field Scanning Transmission Electron Microscopy) image of CdSe-PbSe dumbbell HNCs, consisting of CdSe nanorods with PbSe tips at both ends. In this imaging mode, the intensity scales with Z^2 , where Z is the atomic number. As Pb has a higher Z than Cd, PbSe NCs exhibit brighter contrast than the CdSe nanorods. When the HNCs were heated to 160 °C with a heating rate of 10 degrees/min and annealed at this temperature for 5 min, the bright contrast corresponding to PbSe was observed not only at the tips but also extended gradually inside the nanorod domain (solid arrows in Figure 5.1b), showing that the PbSe phase grows at the expense of the CdSe phase. When the HNCs were heated to 200 °C with the same heating rate and annealed at this temperature for 5 min, the bright contrast was observed over the entire nanorod in some nanorods (solid arrows in Figure 5.1c). The evolution of this growth was seen to initiate mostly from one PbSe tip domain, though it can also proceed from both PbSe tip domains (dashed arrows in Figure 5.1b and 5.1c).

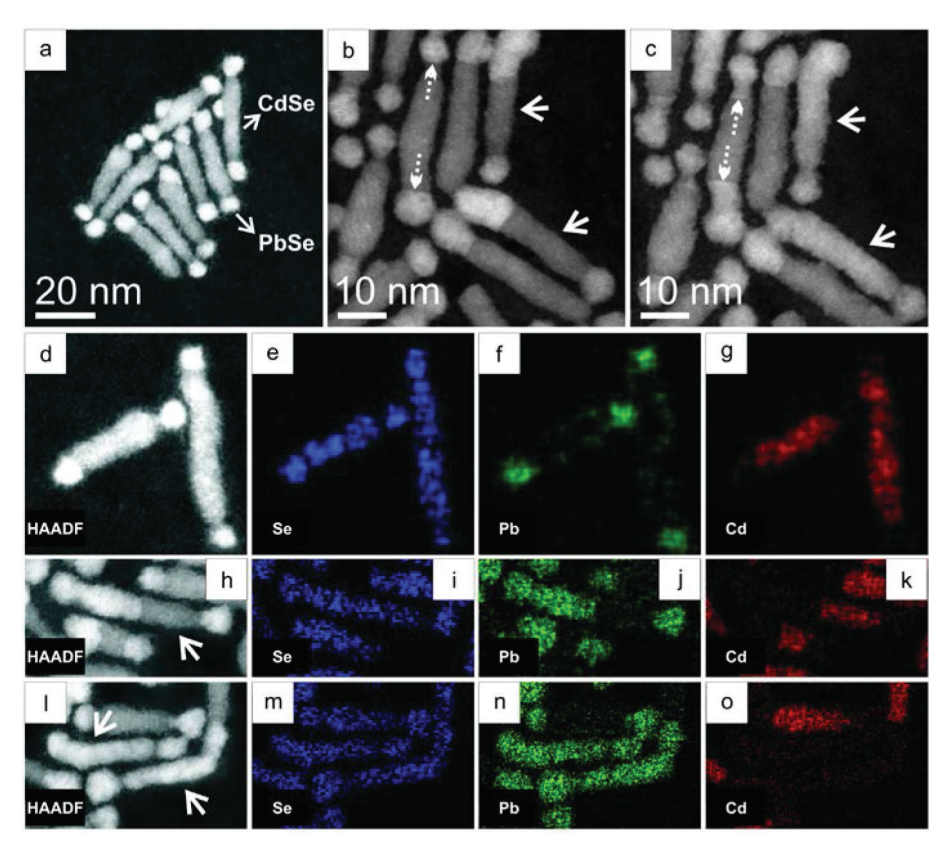


Figure 5.1. HAADF-STEM images and chemical mapping of the nanodumbbells before and after heating. (a) HAADF-STEM image of CdSe-PbSe nanodumbbells. The PbSe tips exhibit brighter contrast than the CdSe nanorods due to Z-contrast. (b and c) Dumbbell HNCs at 160 °C (b) and at 200 °C (c), showing gradual extension of PbSe domains at the expense of CdSe. A heating rate of 10 degrees/min was used in the in-situ studies and the HNCs were annealed at the indicated temperatures for 5 min before imaging. Dumbbell HNCs with solid arrows transformed totally to brighter contrast with heating. This phenomenon occurred mostly from one side, though it can proceed from both PbSe domains as well (dumbbell with dashed arrows in panel c). (d-o) HAADF-STEM images and corresponding STEM-EDX elemental maps of dumbbell heteronanostructures annealed for 5 min at temperatures of (d-g) 100 °C, (h-k) 170 °C, and (l-o) 200 °C. In panels d-g, HNCs are in original dumbbell state with PbSe tips and CdSe nanorod. In panels h-k, a partially transformed nanorod is present. In panels l-o, two PbSe-CdSe HNCs became full PbSe domains. The Se remains in place during the transformation. Note that the contrast is maximized in each individual image; hence, intensities of different mappings cannot be directly compared. Quantitative analyses are provided in Appendix C.

Chemical mapping by means of Energy-Dispersive X-ray Spectrometry (EDX) using a Chemi-STEM detector (see Methods and Appendix C) was performed to provide further evidence of the chemical transition. Figure 5.1d-5.1g shows the initial state of the HNCs at 100 °C with CdSe nanorods and PbSe tips. Figure 5.1f shows that Pb is also present at the lateral surfaces of the CdSe nanorods, pointing to adsorbed Pb-oleate molecules. The dumbbell depicted with an arrow in Figure 5.1h underwent a transformation, after which half the nanorod exhibited a bright contrast. With annealing at 170 °C for 5 min, the elemental maps of this dumbbell in Figure 5.1i-5.1k show that Pb is indeed present in the bright contrast regions and that Cd is absent. We therefore conclude that Cd started to sublimate (as neutral Cd atoms or in a molecular form) and that at the same time, PbSe was formed by Pb incorporation. Upon further heating to 200 °C and 5 min annealing at this temperature, two nanorods (indicated with arrows in Figure 5.1l) exhibited a bright contrast over their entire length. Elemental maps (Figure 5.1m-5.1o) showed that Cd is no longer present and the nanorod completely transformed into PbSe. Disappearance of Cd from a nanostructure was also reported by De Trizio et al.¹² during a heating of sandwich-morphology CdSe/Cu₃P/CdSe HNCs. Note that complete transformation occurred very rarely (in about one per cent of the cases). Further heating of partially cation-exchanged nanodumbbells led to dissociation of the domains. The transformations took place everywhere on the substrate, not only in areas that were previously examined with the electron beam. The field of view was changed frequently in order to avoid beam effects when monitoring the evolution of the HNCs.

As a result of the cation exchange from CdSe to PbSe, the crystal structure transformed epitaxially from hexagonal wurtzite (WZ) to cubic rock-salt (RS). Figure 5.2 shows this transformation at atomic resolution. When the HNC was heated from 160 °C (Figure 5.2a) to 180 °C (Figure 5.2b) with a heating rate of 10 degrees/min, the brighter intensity corresponding to PbSe advanced into the CdSe region. The PbSe RS (200) lattice spacings started to appear along the nanorod domain instead of the CdSe WZ (0002) lattice spacings, as confirmed by the Fourier Transformation (FT) patterns shown next to each image. It is clear that the cation exchange takes place at the PbSe/CdSe interface and propagates epitaxially (layer by layer) along the WZ <0001> direction.

Two types of interfaces were observed: {100}PbSe/{0001}CdSe and {111}PbSe/{0001}CdSe, similar to the interfaces previously reported in the literature for PbSe/CdSe and PbS/CdS HNCs.^{7,19} Sometimes both types of interfaces were observed within one single dumbbell NC. Figure 5.3a shows a HNC with the interfaces of {111}PbSe/{0001}CdSe on the left (Figure 5.3b) and {100}PbSe/{0001}CdSe on the right (Figure 5.3d). It is clear from Figure 5.3 that epitaxial PbSe growth inside CdSe domain via cation exchange can advance from both PbSe/CdSe interfaces.

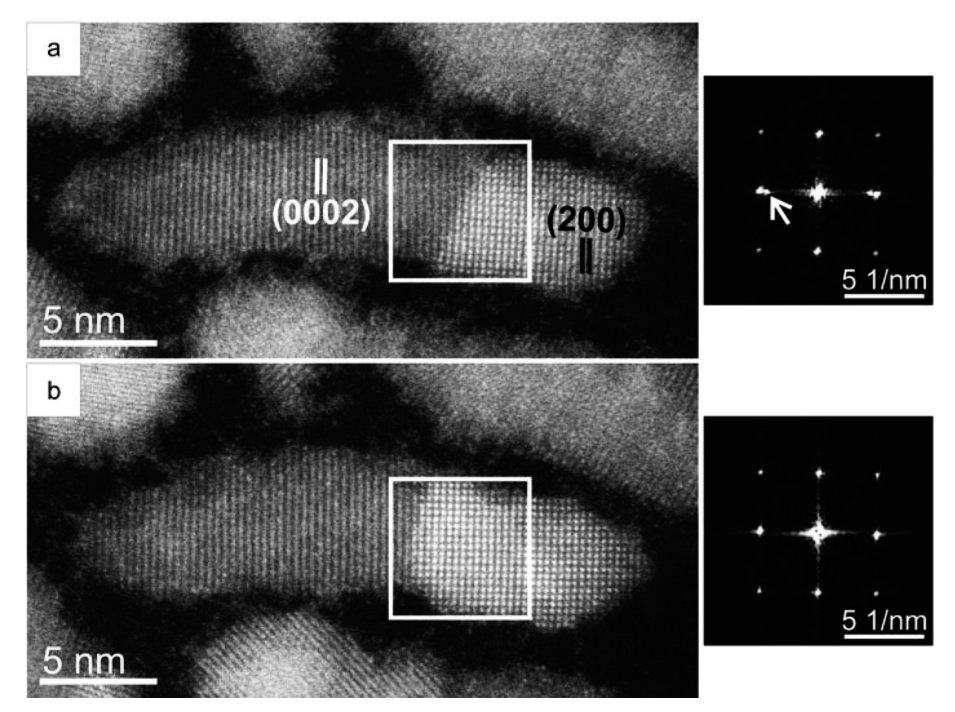


Figure 5.2. Atomic resolution HAADF-STEM images of CdSe-PbSe HNCs. PbSe has cubic rock-salt (RS) crystal structure with a lattice constant of 6.13 Å,²⁰ while CdSe has a hexagonal wurtzite (WZ) crystal structure with lattice parameters a=4.29 Å and c=7.01 Å.²¹ The CdSe WZ (0002) spacing is 3.5 Å and PbSe RS (200) spacing is 3.1 Å. With heating from 160 °C (a) to 180 °C (b) with a heating rate of 10 degrees/min, WZ CdSe nanorods started to transform to RS PbSe. Fourier Transforms (FTs) next to the images were taken from the white squares in each image. The spot depicted with an arrow in the FT of the white square in Figure 5.2a corresponds to WZ CdSe (0002) spacing. It disappeared in the FT of the white square in Figure 5.2b, confirming the WZ to RS transformation.

Considering the source of Pb that is required for the epitaxial PbSe growth in CdSe via cation exchange, we note that PbSe NCs with excess Pb surface atoms (off-stoichiometric) have been reported in the literature. ²²⁻²⁴ Pb atoms (possibly Pb-oleate molecules) are also present along the CdSe nanorods (Figure 5.1f). From the quantification of the elemental maps (see Methods and Table C.1), it was found that the PbSe tips contained an excess of Pb, having a cation/anion ratio of 1.3±0.2. After the transformation, the cation/anion ratio at these PbSe tips reduced to 1.02±0.14. These findings indicate Pb diffusion from PbSe tips towards the PbSe/CdSe interface.

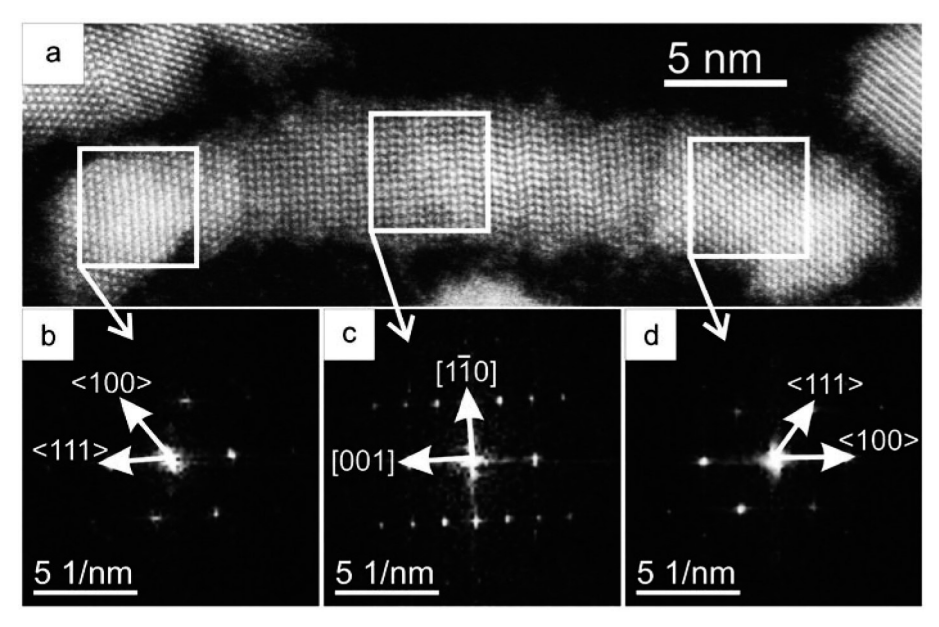


Figure 5.3. (a) HAADF-STEM image of a PbSe-CdSe dumbbell HNC. Stacking faults and a dislocation are present in the WZ CdSe nanorod domain. The interface at the left-hand side is {111}PbSe/{0001}CdSe (Figure 5.3b) whereas the interface at the right-hand side is {100}PbSe/{0001}CdSe (Figure 5.3d).

In the nanorod domains attached to the PbSe tips where cation exchange took place, the cation/anion ratio in the rod was reduced to 0.93±0.11 due to Cd sublimation. That most nanodumbbells were not completely transformed must, hence, be due to the depletion of the source of Pb. The excess Pb atoms at the surfaces of the heteronanointerface diffuse toward the interface to form new layers of PbSe, but this process stops when all excess Pb has been depleted. As mentioned above, a complete transformation of the nanorods occurred only rarely. From an estimate of the number of Pb-oleate molecules that could cover the surface of the nanodumbbells (assuming a high surface density of 5 Pb-oleate molecules per square nanometer), it was found that for the typical dimensions of the nanodumbbells in this study, the number of surface Pb atoms is not sufficient to replace all the Cd atoms in the CdSe domain (the number of Cd sites is at least two times larger). Therefore, when a complete transformation did occur, likely also Pb atoms from neighboring HNCs contributed to the growth of the PbSe domain. This is in agreement with the observation that when the nanodumbbells were lying isolated on the SiN support membrane, the growth process did take place but always resulted in only a partial transformation.

In order to better understand the nanoscopic growth mechanism at the PbSe/CdSe interface, force field based Molecular Dynamics (MD) simulations were performed on HNC models taking into account various possibilities for the PbSe/CdSe interfacial arrangements (details in Methods and Appendix C). Surfactant molecules are not included in the simulation models, and therefore the MD simulations serve only to study the structure and atomic mobility at the PbSe/CdSe interfaces. The isolated nanodumbbell models were equilibrated at 300 K and 500 K for 5 ns sequentially. Figure 5.4a shows the final configuration of a nanodumbbell model after 5 ns at 500 K. This model has both types of the interfaces ({100}PbSe/{0001}CdSe and {111}PbSe/{0001}CdSe) in one HNC.

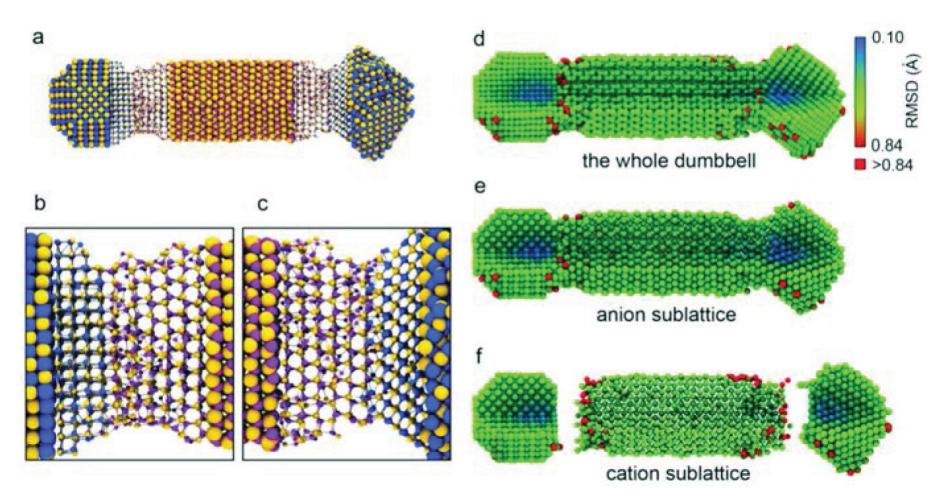


Figure 5.4. Force-field MD simulations of the PbSe-CdSe nanodumbbells. (a) Overview image showing the final configuration of a dumbbell obtained after MD simulation at a temperature of 500 K for 5 ns. The ball-stick presentation was used to show the structure of the interfaces. The yellow, purple, and blue spheres are Se, Cd, and Pb atoms, respectively. (b) Magnified image of the {100}PbSe/{0001} CdSe interface at the left-hand side of the dumbbell, and (c) magnified image of the {0001}CdSe/{111} PbSe interface at the right-hand side of the dumbbell. (d, e and f) The map of the root-mean-squared displacement (RMSD) for each atom for the same PbSe-CdSe dumbbell model at 500 K. (d) The whole PbSe-CdSe dumbbell, (e) the anion sublattice, and (f) the cation sublattice. The dumbbell was cut so that both of the surface and inner atoms can be seen. The pure red atoms correspond to those having a RMSD larger than 0.84 Å.

The nanodumbbell model shown in Figure 5.4 is structurally and morphologically stable at temperatures up to 500 K. The middle part of the CdSe rod and both PbSe tips retain their initial WZ and RS structures, respectively. Structural disorder was mainly found in the CdSe domains near the interfaces. Compared to the {100}PbSe/{0001}CdSe interface, the CdSe domain near the {111}PbSe/{0001}CdSe interface is structurally more ordered. In the latter case, most of the Cd and Se atoms remain at the WZ lattice sites, which is likely due to the fact that the cation-terminated {0001}CdSe surface and the anion-terminated {111}PbSe surface form a continuous polar/polar interface, whereas the lattice mismatch is small. In contrast, the {100} PbSe/{0001}CdSe interface is a nonpolar/polar interface, which leads to stronger distortions in the atomic lattice due to Coulombic interactions. The simulations therefore suggest that the transformation at the {100}PbSe/{0001}CdSe interface will be more efficient than at the {111} PbSe/{0001}CdSe interface, although this could not be confirmed by the experiments as the orientation of the two crystals could be determined only in a limited number of cases. Not only is the atomic structure more disordered in the CdSe domains near the {100}PbSe/{0001}CdSe interfaces (see Appendix C, Figure C.4 for a planar view of the atomic bilayers parallel to the interface), the simulations also show an unusually high mobility of the Cd atoms in the few first atomic layers from the PbSe/CdSe interface, as evidenced by the map of the root mean square displacement (RMSD) for each atom (Figure 5.4d-5.4f). Those atoms with the highest mobility (red atoms) are mostly Cd atoms near the interfaces or on the surface, indicating that the cation exchange occurs only very close to the interface.

The experimental observations and the MD simulations suggest that the transformation is mediated by vacancies in the Cd and Pb sublattices; evaporation of Cd results in Cd vacancies at the CdSe surface. After migration of these Cd vacancies to the PbSe/CdSe interface, Pb atoms can jump into the vacant sites, thereby leaving behind vacancies on the Pb sublattice, which will eventually recombine with excess Pb absorbed at the surface of the PbSe domain. Density Functional Theory (DFT) calculations of defect energies (see Appendix C.5) confirm that upon evaporation of Cd, the defect energetics are ruled by vacancies in CdSe and PbSe. The DFT calculations also show (Table C.5) that the Se-Frenkel defect energy (Se vacancy + Se interstitial) is considerably higher (6.00 for CdSe and 3.80 eV for PbSe) than the Cd-Frenkel and Pb-Frenkel defect energies (3.16 and 3.30 eV, respectively). It is, thus, energetically much more expensive to create defects on the Se sublattice. Because the Se sublattice is not much affected by the cation exchange which takes place on the Pb and Cd sublattice, the crystallographic orientation relation between the CdSe and PbSe nanodomains is retained during the transformation. This is the reason that the growth process is epitaxial in nature.

The most important driving force for the growth process is the evaporation of Cd. It is well known that a chemical reaction can be efficiently driven into one direction by bringing one reaction product in the gas phase. Assuming that the excess Pb originates from Pb-oleate coverage of the HNC and that the Cd evaporates in a molecular form, the chemical reaction can be summarized as follows:

CdSe (s) + Pb-molecule (s)
$$\rightarrow$$
 PbSe (s) + Cd-molecule (g) (5.1)

In the CdSe lattice, the Cd and Se atoms can be modelled as ions. Bader charge analysis (details in Appendix C.5) performed on the electronic charge density obtained from DFT calculations shows that the effective charge of the Cd cation in CdSe bulk is approximately +0.8 e. However, Cd will evaporate only as a neutral species. Because the transition from a charged Cd^{+0.8} ion to a neutral Cd⁰ atom would require the nanocrystal to donate electrons, we consider it more likely that Cd at the surface of the nanocrystal binds to the surfactants (e.g., oleate), followed by evaporation. We mention here that heating in vacuum is an efficient method to detach surfactants from nanocrystals.^{20,25}

5.3 Conclusions

From the available experimental and simulation data, a mechanism can now be deduced to describe the cation exchange. All processes take place close to the interfaces in a fast and volatile manner. The growth mechanism is shown schematically in Figure C.1 of Appendix C, and can be summarized as follows. (i) Cd sublimates from the surface of the CdSe nanodomains, whereby Cd vacancies are formed. (ii) The Cd vacancies occupy positions at the CdSe side of the PbSe/CdSe interface (Figures 5.4 and Figure C.4). (iii) Cation replacement takes place as Pb atoms jump into vacant Cd sites in a layer by layer fashion, resulting in epitaxial growth of RS PbSe at the expense of WZ CdSe. (iv) The jumped Pb atoms leave behind vacancies, which migrate to the PbSe surface. (v) The Pb vacancies at the surface recombine with Pb ions from adsorbed Pb-oleate molecules. The oleate molecule remains adsorbed at the PbSe surface, and possibly migrates to the CdSe domain where it combines with Cd and evaporates as Cd-oleate. (vi) The process is halted when the excess Pb (in the form of Pb-oleate molecules) in the system is depleted.

The atomistic mechanism described here most likely also takes place when HNCs undergo cation exchange in colloidal solutions, whereby instead of evaporating, the metal-molecule complex is dissolved in the solution. In the current solid—solid—vapor (SSV) growth mechanism, one solid phase grows epitaxially at the expense of another solid phase, efficiently driven by evaporation of one element (here, Cd) with simultaneous supply of another element (here, Pb coordinated with a molecule). Our results show that SSV growth can provide an alternative path for growing heterogeneous semiconductor nanowires, especially when the lattices have a partly ionic character, and therefore holds promise for generating new families of heterogeneous nanostructures.

5.4 Methods

The synthesis of PbSe/CdSe dumbbell nanostructures is detailed in Appendix C. TEM specimens were prepared by dropcasting 8 μ L of the NC colloidal solution onto a MEMS micro-hotplate with electron-transparent SiN membranes, which was mounted onto an in-

house built low drift TEM heating holder.²⁵ After dropcasting, the sample was plasma cleaned for 10 s in order to remove deposits from the solution that prevent high-resolution imaging in the TEM. The in situ experiments were performed in a 80-300 FEI Titan microscope equipped with a Chemi-STEM EDX detection system. During HAADF-STEM imaging, the microscope was operated at 300 kV. The camera length used in the experiments equals 91 mm in order to avoid diffraction effects and to guarantee Z-contrast imaging. In HAADF-STEM imaging, the intensity approximately scales with Z^2 . As Pb has a higher Z number than Cd, the PbSe domains appear with higher intensity in HAADF-STEM images in comparison to the CdSe domains.

The Chemi-STEM EDX experiments were performed using the same holder and in the same 80-300 FEI Titan microscope but operated at a lower acceleration voltage of 200 kV to reduce beam damage during mapping. A beam current of approximately 250 pA was used during acquisition. In the quantification of the elemental maps, 18 PbSe NC maps were used to determine the cation/anion ratio at the PbSe tips at the initial state. For the PbSe tips from where cation exchange proceeded, the elemental composition of 10 different PbSe tips was quantified. For the nanorod domains attached to the PbSe tips where cation exchange took place, the elemental composition of 10 different nanorod (transformed)-domains was quantified. Throughout the studies, only 4 totally transformed nanodumbbell domains were observed and they were also quantitatively analysed. Quantitative analyses are provided in Table C.1 in Appendix C. Interested readers can find more details free of charge (additional HAADF-STEM images, chemical maps, representative EDX spectrum) in the supporting information of the publication.

For the force-field MD simulations, a new interaction potential model for the Pb-Cd-Se system was developed. The potential was found to accurately describe physical parameters such as lattice parameters, elastic constants, and the relative stability of phases. Details of the potential model (Appendix C, Table C.2) and a description of the nanodumbbell models are given in Appendix C.4. For simulations of the nanodumbbells, Coulomb and short-range interactions were calculated by taking into account all atom pairs. The equations of motion were integrated using the velocity Verlet algorithm with a time step of 1 fs. Periodic boundary conditions were not used and the nanodumbbell models were isolated in vacuum. Simulations of 5 ns were carried out in the NVT ensemble and 1 ns was used for equilibration.

All density functional theory (DFT) calculations on defect energies and energies of mixed PbSe-CdSe phases were carried out using the first-principles' Vienna Ab Initio Simulation Program (VASP)²⁶ using the projector augmented wave (PAW) method.²⁷ The generalized gradient approximation (GGA) formulated by Perdew, Burke, and Ernzerhof (PBE) was employed for the exchange and correlation energy terms.²⁸ The cutoff energy of the wave functions was 350.0 eV. The cutoff energy of the augmentation functions was about 500.0 eV. The electronic wave functions were sampled on a $4 \times 4 \times 2$ grid using the Monkhorst and Pack method with 8 to 20 k-points depending on different symmetries of supercells (108 atoms). Structural optimizations were performed for both lattice parameters and coordinates of atoms. Different k-meshes and cutoff energies for waves were tested to have a good convergence (<2 meV/atom). Details are given in Appendix C.

References

- Son, D. H.; Hughes, S. M.; Yin, Y.; Alivisatos, A. P. Science 2004, 306, 1009-1012. 1
- 2 Robinson, R. D.; Sadtler, B.; Demchenko, D. O.; Erdonmez, C. K.; Wang, L. -W.; Alivisatos, A. P. Science 2007, 317, 355-358.
- Bals, S.; Casavola, M.; van Huis, M. A.; Van Aert, S.; Batenburg, K. J.; Van Tendeloo, G.; 3 Vanmaekelbergh, D. Nano Lett. 2011, 11, 3420-3424.
- Casavola, M.; van Huis, M. A.; Bals, S.; Lambert, K.; Hens, Z.; Vanmaekelbergh D. Chem. Mater. 4 2012, 24, 294-302.
- Grodzińska, D.; Pietra, F.; van Huis, M. A.; Vanmaekelbergh, D.; de Mello Donegá, C. J. Mater. 5 Chem. 2011, 21, 11556-11565.
- Zhang, Y.; Dai, Q.; Li, X.; Cui, Q.; Gu, Z.; Zou, B.; Wang, Y.; Yu, W. W. Nanoscale Res. Lett. 2010, 6 5, 1279-1283.
- Kudera, S.; Carbone, L.; Casula, M. F.; Cingolani, R.; Falqui, A.; Snoeck, E.; Parak, W. J.; Manna, 7 L. Nano Lett. 2005, 5, 445-449.
- Overgaag, K.; Evers, W.; de Nijs, B.; Koole, R.; Meeldijk, J.; Vanmaekelbergh, D. J. Am. Chem. 8 Soc. 2008, 130, 7833-7835.
- Grodzińska, D.; Evers, W. H.; Dorland, R.; van Rijssel, J.; van Huis, M. A.; Meijerink, A.; de Mello 9 Donegá, C.; Vanmaekelbergh, D. Small 2011, 7, 3493-3501.
- 10 van Huis, M. A.; Figuerola, A.; Fang, C.; Béché, A.; Zandbergen, H. W.; Manna, L. Nano Lett. 2011, 11, 4555-4561.
- Figuerola, A.; van Huis, M.; Zanella, M; Genovese, A.; Marras, S.; Falqui, A.; Zandbergen, H. 11 W.; Cingolani, R.; Manna, L. Nano Lett. 2010, 10, 3028-3036.
- 12 De Trizio, L.; De Donato, F.; Casu, A.; Genovese, A.; Falqui, A.; Povia, M.; Manna, L. ACS Nano 2013, 7, 3997-4005.
- Yalcin, A. O.; de Nijs, B.; Fan, Z.; Tichelaar, F. D.,; Vanmaekelbergh, D.; van Blaaderen, A.; Vlugt, 13 T. J. H.; van Huis, M. A.; Zandbergen, H. W. Nanotechnology 2014, 25, 055601.
- 14 Wagner, R. S.; Ellis, W. C. Appl. Phys. Lett. 1964, 4, 89-90.
- Gudiksen, M. S.; Lauhon, L. J., Wang, J.; Smith, D. C.; Lieber, C. M. Nature 2002, 415, 617-620. 15
- 16 Wang, H.; Zepeda-Ruiz, L. A.; Gilmer, G. H.; Upmanyu, M. Nat. Comm. 2013, 4,
- 17 Persson, A. I.; Larsson, M. W.; Stenström, S.; Ohlsson, B. J.; Samuelson, L.; Wallenberg, L. R. Nat. Mater. 2004, 3, 677-681.
- Campos, L. C.; Tonezzer, M.; Ferlauto, A. S.; Grillo, V.; Magalháes-Paniago, R.; Oliveira, S.; 18 Ladeira, L. O.; Lacerda, R. G. Adv. Mater. 2008, 20, 1499-1504.
- 19 Luther, J. M.; Zheng, H.; Sadtler, B.; Alivisatos, A. P. J. Am. Chem. Soc. 2009, 131, 16851-16857.
- van Huis, M. A.; Kunneman, L. T.; Overgaag, K.; Xu, Q.; Pandraud, G.; Zandbergen, H. W.; 20 Vanmaekelbergh, D. Nano Lett. 2008, 8, 3959-3963.

- 21 Xu, Y. -N.; Ching, W. Y. Phys. Rev. B 1993, 48, 4335-4351.
- 22 Moreels, I.; Lambert, K.; De Muynck, D.; Vanhaecke, F.; Poelman, D.; Martins, J. C.; Allan, G.; Hens, Z. Chem. Mater. 2007, 19, 6101-6106.
- Moreels, I.; Fritzinger, B.; Martins, J. C.; Hens, Z. J. Am. Chem. Soc. 2008, 130, 15081-15086. 23
- 24 Petkov, V.; Moreels, I.; Hens, Z.; Ren, Y. Phys. Rev. B 2010, 81, 241304.
- van Huis, M. A.; Young, N. P.; Pandraud, G.; Creemer, J. F.; Vanmaekelbergh, D.; Kirkland, A. I.; 25 Zandbergen, H. W. Adv. Mater. 2009, 21, 4992-4995.
- Kresse, G.; Hafner, J. Phys. Rev. B 1993, 47, 558-561. 26
- Kresse, G.; Joubert, D. Phys. Rev. B 1999, 59, 1758-1775. 27
- Perdew, J. P.; Burke, K.; Ernzerhof, M. Phys. Rev. Lett. 1996, 77, 3865-3868. 28

Appendix C

C.1 Schematic of the atomistic growth mechanism

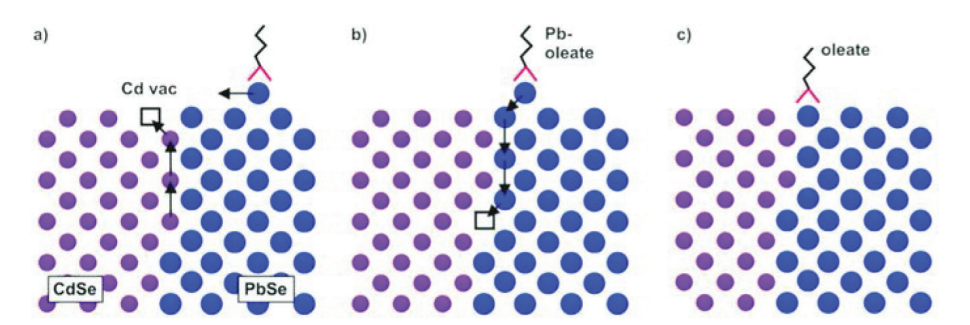


Figure C.1. Schematic depicting the cation exchange process. Only the Cd, Pb atomic species are shown. (a) After a Cd vacancy is formed at the CdSe surface, it will diffuse at the CdSe side of the CdSe/PbSe interface. (b) The cation exchange step takes place when a Pb atoms from the other side of the interface jumps into the vacant Cd site. The Pb vacancy which is thereby formed will diffuse to the PbSe surface, where it recombines with the Pb from an adsorbed Pb-oleate molecule. (c) The oleate molecule remains adsorbed at the HNC surface.

C.2 Synthesis of the PbSe-CdSe nanodumbbells

Chemicals:

Cadmium oxide (CdO, 99.99%), tri-n-octylphosphine oxide (TOPO, 99%), tri-octylphosphine (TOP, 90%), selenium powder (98%), diphenyl ether (DPE, 99%), oleic acid (OLAC, 90%) and lead(II) acetate trihydrate (99.95%) were purchased from Sigma Aldrich; n-tetradecylphosphonic acid (TDPA) and n-hexylphosphonic acid (HPA) were purchased from PolyCarbon Industries.

Synthesis of the CdSe nanorods:

The synthesis of CdSe nanorods was performed according to the procedure published by Gur et al. and Peng et al. In a typical synthesis 0.2 g cadmium oxide, 0.71 g of n-tetradecylphosphonic acid, 0.16 g n-hexylphosphonic acid and 3 g of tri-n-octylphosphine oxide are loaded in 50 ml flask. The mixture is heated to 120 °C in nitrogen atmosphere and then kept at 120 °C under vacuum for one hour. The mixture is successively heated up to 300 °C under nitrogen for about 30 min to allow CdO to dissolve. The mixture is then heated up to 310 °C and 1.5 g of trioctylphosphine (TOP) are injected. When the temperature recovers to 310 °C, a solution of selenium in TOP (0.073 g Se + 0.416 g TOP) is rapidly injected and the reaction is allowed to proceed at a constant temperature of 310 °C for 7 min. The reaction is finally quenched by fast removal of the heating source. The nanoparticle suspension is allowed to cool down and at about 50 °C and 2.5 ml of anhydrous toluene are added. The nanorod suspension is purified by three cycles of precipitation in isopropanol, centrifugation and re-dispersion in toluene.

Synthesis of the CdSe-PbSe heterostructures:

PbSe-tipped CdSe nanorod heterostructured nanocrystals have been synthesized according to the method published by Kudera et al.3 and Carbone et al.4 with slight modifications. A stock solution of lead oleate is prepared by degassing 2 mL diphenyl ether (DPE), 1.5 mL oleic acid and 1.7 mmol Lead (II) acetate for 2 hours at 120 °C. The solution is cooled to room temperature and then transferred and stored in a nitrogen-filled glovebox. For the heterostructure preparation, 5 ml diphenyl ether are degassed under vacuum at 120 °C for about 30 min. The degassed solvent is then allowed to cool down to about 50 °C and 0.3 ml of a suspension of CdSe nanorods are injected under nitrogen atmosphere. The suspension of nanorods in DPE is then heated up to 130 °C under nitrogen atmosphere. Then, a mixture of precursors is prepared in a nitrogen filled glovebox by mixing 0.75 ml of lead oleate stock solution with 0.45 ml TOP and 0.3 ml of a Se-TOP solution (1M). This solution, containing both the Pb and Se precursors in a 1:1 proportion, is then drop-wise injected in the CdSe/DPE suspension at 130 °C via a syringe pump at a rate of 0.1 ml/min. Once all the precursor solution has been injected the temperature is kept at 130 °C for additional 3 min. The suspension is then allowed to cool down to room temperature and it is transferred in the glovebox. The CdSe-PbSe nanocrystals are purified by three cycles of precipitation of the suspension in butanol/methanol, centrifugation and re-dispersion in toluene.

C.3 Quantitative results of STEM-EDX elemental maps

Table C.1. Chemical composition of nanodomains (quantification of STEM-EDX maps using the Cliff-Lorimer method). Interested readers can find more details free of charge (HAADF-STEM images and chemical maps) in the supporting information of the publication.

	Pb (at.%)	Se (at.%)	Cd (at.%)	cation/anion ratio
PbSe tips at initial state	51 ± 6	43 ± 5	6 ± 4	1.3 ± 0.2
PbSe tips from where cation exchange				
proceeded to certain extent	44 ± 3	49 ± 5	7 ± 4	1.02 ± 0.14
Nanorod domains where partial cation exchange took place	42 ± 5	52 ± 2	6 ± 3	0.93 ± 0.11
PbSe tips of nanorods where total cation exchange was observed	46 ± 2	51 ± 3	3 ± 3	0.94 ± 0.10
Nanorod domains where total cation exchange was observed	46 ± 2	51 ± 3	3 ± 3	0.97 ± 0.09

C.4 Force-field MD simulations

Force field for the Pb-Se-Cd system

There are very few of force fields developed for CdSe and PbSe in the literature. One of the most frequently used force fields for CdSe is developed by Rabani⁵ within a Partially Charged Rigid Ion Model (PCRIM) approach.⁶ In this force field model, Lennard-Jones (LJ) potentials were used to describe the short-range interactions and effective charges of ±1.18 e for Cd and Se ions were obtained by empirical fitting. Schapotschnikow et al. developed a force field for PbSe using the same model to study the morphological evolution of PbSe nanocrystals. In this PbSe force field, the effective charges for Pb and Se ions were ±1.29 e, and the parameters of the LJ potential that describe the Se-Se short-range interactions in PbSe were very different from that in the CdSe force field. Therefore, these two force fields cannot be easily combined to describe the Pb-Cd-Se system. To our best knowledge, up to now there was no transferable force field developed for the Pb-Cd-Se system. In this work, a set of transferable pair potentials was derived for the Pb-Se-Cd system. The PCRIM model6 was chosen to describe the interatomic interactions. Interatomic interactions only contain Coulomb interactions and short-range twobody interactions (Buckingham potential):

$$u_{ij}(r_{ij}) = \frac{q_i q_j}{r_{ij}} + Ae^{-\frac{r_{ij}}{\rho}} - \frac{c}{r_{ij}^6}$$
 (C.1)

The first term in this equation is the electrostatic potential, and the second and third terms describe the short-range interactions. r_{ii} is the interatomic distance, q_i is the effective charge, A, ρ , and C are model parameters.

The Bader charge analysis8 was performed on the results of density functional theory (DFT) calculations on CdSe and PbSe bulk phases in order to determine accurate values of the effective charges on the atoms. The Bader charges of the Cd atoms the wurtzite (WZ), zinc blende (ZB), rock salt (RS), and honeycomb (HC) structures are 0.711, 0.725, 0.825, and 0.750 e, respectively, and that of the Pb atoms in the RS, cesium chloride (CsCl), ZB and HC structures are 0.812, 0.813, 0.804, 0.781 e, respectively. The value of the effective charges in the force field model were set as $q = \pm 0.8$ e for both cations and anions. The interatomic short-range interactions between two cations are omitted since the effective ion radii of cations are relatively small. The Buckingham parameters were obtained by fitting to experimental data and DFT simulations. The experimental data includes the lattice parameters, elastic constants, and bulk moduli of CdSe in the WZ and ZB structures and PbSe in the RS structure. The DFT data includes lattice parameters and relative stabilities of four CdSe polymorphs (WZ, ZB, RS, and HC) and four PbSe polymorphs (RS, CsCl, ZB, and HC). The lattice parameters obtained from DFT calculations were normalized be rescaling their volumes, in which the scale factors for CdSe and PbSe polymorphs were respectively the ratios of the volumes of WZ-CdSe and RS-PbSe computed from DFT divided by the experimental value. The ratios of c/a from our DFT calculations remained unchanged. Relaxed fitting was used in the fitting procedure in order to achieve a higher quality of fitting. A cut off radius of 12.0 Å was set for all shortrange interactions and the Ewald summation9 was used to calculate the long-range Coulomb interactions in the bulk phases. All calculations in the fitting procedure were carried out by The General Utility Lattice Program (GULP).¹⁰ The complete parameter set for the Pb-Se-Cd system is listed in Table C.2.

Table C.2. Parameters of the Pb-Se-Cd force field. The effective ion charges q are ±0.8 e. Short-range interactions between cations were not taken into account.

Interactions	Interactions A (eV)		C (eV·Å ⁶)	
Cd-Se	2640000000	0.108	64.4	
Pb-Se	4880000	0.173	211	
Se-Se	5200	0.384	127	

In Table C.3 and C.4, several physical properties of PbSe and CdSe polymorphs calculated from our Pb-Se-Cd force field are listed, together with available experimental results and DFT computations. Note that the data used in fitting procedure is in bold and the normalized lattice parameters are listed in square brackets. To obtain the lattice parameters and root mean square displacement (RMSD) at 300 K, MD simulations were performed for the WZ-CdSe and RS-PbSe structures. In general, the Pb-Se-Cd force field is able to reproduce quite a wide range of physical properties of CdSe and PbSe polymorphs with considerable accuracy.

C.4.2Model construction for the PbSe-CdSe nanodumbbells

Two different PbSe/CdSe interfaces were observed in the dumbbell NCs by HREM: {100}PbSe/{0001}CdSe and {111}PbSe/{0001}CdSe. The former is a non-polar/polar interface and the latter is a polar/polar interface. The polarization of the CdSe rods and PbSe tips cannot be distinguished by the HREM data. Therefore, we assumed that all possible combinations of the four facets existed in the specimen: {100}PbSe/Se-{0001}CdSe (Se sublattice ended CdSe), {100}PbSe/Cd-{0001}CdSe (Cd sublattice ended CdSe), Pb-{(111)}PbSe/Se-{0001} CdSe (Pb sublattice ended PbSe with Se sublattice ended CdSe), Se-{111}PbSe/Cd-{0001}CdSe (Se sublattice ended PbSe with Cd sublattice ended CdSe).

Table C.3. Physical properties of CdSe calculated by lattice statics (LS) and MD simulations, compared to experimental and DFT data. Lattice parameters a and c are in Å; u is the internal coordinate; the elastic constants c_{ij} and bulk moduli B are in $\hat{G}Pa$; the lattice energy E_{latt} and energy difference ΔE are in eV/f.u.; the transition pressure P_T is in GPa; the RMSD ξ is in Å; the surface energy E_{surf} is in J/m². The values in parentheses are MD results at 300 K; the values in square brackets are normalized lattice parameters from DFT calculations; the values in bold are data used for the fit of the force field parameters.

CdSe	Exp.a	PCRIM	DFT ^b			
Wurtzite, space group P6 ₃ mc (No. 186)						
а	4.30	4.32 (4.36)	4.39			
с	7.01	6.94 (7.00)	7.17			
и	0.376	0.379	0.375			
c_{11}	74.1	72.4	80			
c_{12}	45.2	47.9	47			
c_{13}	39.0	41.4	40			
c_{33}	84.3	72.5	92			
c_{44}	13.4	12.3	15			
c ₆₆	14.5	12.2	17			
B	53.1	53.1	60			
$E_{ m latt}$	-	-6.026	-			
$P_{\rm T}$ (WZ \rightarrow RS)	3.0	4.1	2.2			
$oldsymbol{\xi}_{ ext{Cd}}$	0.14	(0.32)	-			
$oldsymbol{\xi}_{Se}$	0.13	(0.29)	-			
$E_{\text{surf}} \{11-\bar{2}0\}$	-	0.26	0.50			
$E_{\rm surf}~\{10{\text}\bar{1}0\}$	-	0.25	0.46			
	Zinc blende, space	group $F\overline{4}3m$ (No. 216)				
а	6.08	6.08	6.21 [6.08]			
c_{11}	66.7	61.6	88.1			
c_{12}	46.3	48.8	53.6			
c_{44}	22.3	20.3	27.4			
B	53.1	53.1	65.1			
$\Delta E_{ m ZB-WZ}$	-	0.014	-0.002			
	Rock salt, space gr	$roup Fm\overline{3}m \text{ (No. 225)}$				
а	-	5.63	5.75 [5.63]			
$\Delta E_{ ext{RS-WZ}}$	-	0.291	0.290			
	Honeycomb, space gr	roup P6 ₃ / mmc (No. 194)				
а	-	4.57	4.66 [4.56]			
С	-	5.63	6.07 [5.94]			
$\Delta E_{ ext{HC-WZ}}$	-	0.149	0.211			

^a The lattice parameters, elastic constants, and bulk moduli of WZ- and ZB-CdSe are reported in Ref. ¹¹; the transition pressure of the WZ-RS transition is reported in Ref. 12; the RMSD of CdSe is reported in Ref. 13.

^b The elastic constants and bulk modulus for WZ- and ZB-CdSe are reported in Ref. ^{14,15}; the transition pressure of the WZ→RS transition is reported in Ref. ¹⁶.

Table C.4. Physical properties of PbSe calculated by lattice statics (LS) and MD simulations, compared to experimental and \overline{DFT} data. Lattice parameters a and c are in A; u is the internal coordinate; the elastic constant c_{ij} and bulk modulus B are in GPa; lattice energy E_{latt} and energy difference ΔE are in eV/f.u.; the transition pressure P_{T} is in GPa; the RMSD ξ is in Å; the surface energy E_{surf} is in J/m². The values in parentheses are MD results at 300 K; the values in square brackets are normalized lattice parameters from DFT calculations; the values in bold are data used for the fit of the force field parameters.

PbSe	Exp."	PCRIM	DFT^b			
Rock salt, space group $Fm\overline{3}m$ (No. 225)						
а	6.12	6.09 (6.13)	6.21			
c_{11}	123.7	129.9	123.6			
c_{12}	19.3	16.5	12.2			
c_{44}	15.9	16.5	17.6			
B	54.1	54.3	49.2			
$E_{ m latt}$	-	-6.079	-			
$P_{\rm T}$, (RS \rightarrow CsCl)	16.0	15.6	18.8			
$\xi_{ ext{Pb}}$	0.13	(0.27)	-			
$\xi_{ m Se}$	0.12	(0.24)	-			
$E_{\rm surf} \{100\}$	-	0.29	0.18			
$E_{\rm surf} \{110\}$	- 0.49		0.32			
(Cesium chloride, spac	e group $Pm\overline{3}m$ (No. 221)	1			
a -		3.71	3.77 [3.72]			
$\Delta E_{ ext{CsCl-WZ}}$	-	0.528	0.478			
	Zinc blende, space	group F43m (No. 216)				
a (Å)	-	6.84	6.89 [6.80]			
$\Delta E_{ m ZB-WZ}$	$\Delta E_{ m ZB-WZ}$ -		0.374			
	Honeycomb, space gr	oup P6 ₃ / mmc (No. 194)				
а	-	5.18	5.21 [5.14]			
С	-	6.05	6.23 [6.15]			
$\Delta E_{ ext{HC-WZ}}$	$\Delta E_{ ext{HC-WZ}}$ -		0.320			

^a The lattice parameters, elastic constants, and bulk moduli of RS-PbSe are reported in Ref. ¹⁷; the transition pressure of the RS→CsCl transition is reported in Ref. ¹⁸; the RMSD of PbSe is reported in Ref. 19.

Four nanodumbbell models were constructed (Figure C.2) mimicking the structures, morphologies, and the interfaces of the nanodumbbells observed experimentally. Model 1 has two non-polar/polar interfaces and Model 2 has two polar/polar interfaces. Both model 3 and 4 have one non-polar/polar interface and one polar/polar interface, but their polarizations are anti-parallel. All nanodumbbell models were made of a WZ-CdSe rod and two RS-PbSe tips.

^b The elastic constants and bulk modulus for RS-PdSe is reported in Ref. ²⁰; the transition pressure of the RS→CsCl transition is reported in Ref. 21.

A CdSe rod consists of 3219 CdSe pairs with a length of about 11.0 nm and a diameter of about 4.2 nm, and a PbSe tips consists of 1381 PbSe pairs with a diameter of about 4.5 nm. We tailored the CdSe rod and the PbSe tips to mimic the "necks" of the CdSe rods at the PbSe/ CdSe interfaces and the morphology of the PbSe tips observed experimentally (see Figure 5.1). The CdSe rods are identical in the four models while the PbSe tips have slightly differences in morphology and surface. The surfaces {1010} CdSe, {1120} CdSe, {100} PbSe and {110} PbSe are exposed most to vacuum. These are the most stable surfaces in WZ-CdSe and RS-PbSe with the lowest surface energies. Initially, the orientations of the CdSe rods and the PbSe tips with different types of interfaces were set as same as the nanodumbbell in Figure 5.3, and the initial distance between the PbSe and CdSe interfaces was set as ~3.0 Å.

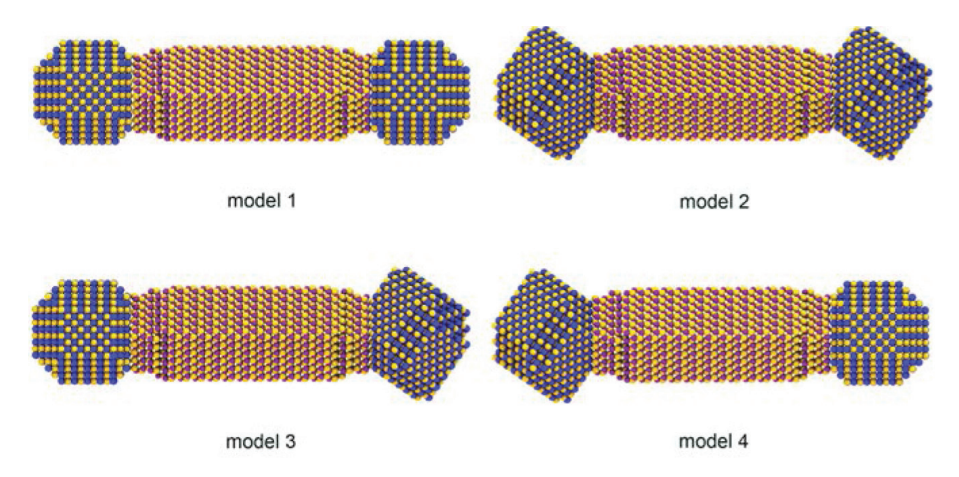


Figure C.2. Four PbSe-CdSe dumbbell configurations (models 1, 2, 3, and 4) having different PbSe/ CdSe interfaces. The yellow, purple, and blue spheres are Se, Cd, and Pb atoms, respectively.

Molecular dynamics simulations results for Model 1, 2, and 4

For the MD simulations, Coulombic and short-range interactions were calculated by taking into account all atom pairs using the newly developed force field potential set given above in Table C.2. Figure C.3 shows the final configurations of the PbSe/CdSe nanodumbbell model 1, 2, and 4 after MD simulations at 500 K for 5 ns.

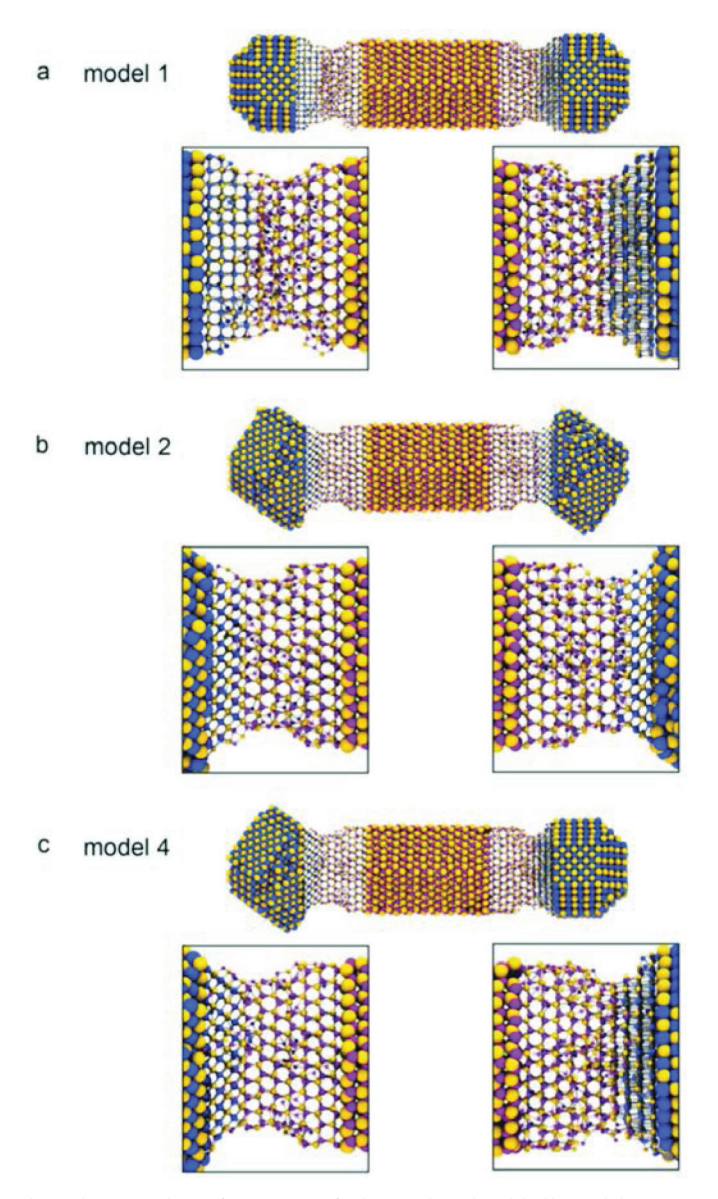


Figure C.3. (a, b and c) Final configuration of PbSe-CdSe dumbbell model 1, 2, and 4 after MD simulations at a temperature of 500 K for 5 ns. The ball-stick presentation was used to show the structure of the interfaces. The yellow, purple, and blue spheres are Se, Cd, and Pb atoms, respectively. Interfaces are magnified for closer inspection.

Figure C.4 shows the {001}PbSe and {0001}CdSe atomic bilayers parallel to the PbSe/CdSe interface at the left-hand side of model 3 shown in Figure 5.4. Figure C.5 shows the maps of rootmean-squared displacement (RMSD) for each atom in the model 1, 2, and 4. Similar results as nanodumbbell model 3 were obtained: All models are structurally and morphologically stable at temperatures up to 500 K in a simulation time of 5 ns. Structural disorder of the surface atoms in the CdSe domains was found near the polar/polar interfaces; stronger structural disorder was found in the CdSe domains near the non-polar/polar interfaces. Cd atoms near the interfaces have an abnormally high mobility compared to the other atoms. According to our simulations, the structural disorder in the CdSe domains and the high mobility of Cd atoms are strongly influenced by the heterostructural interfaces.

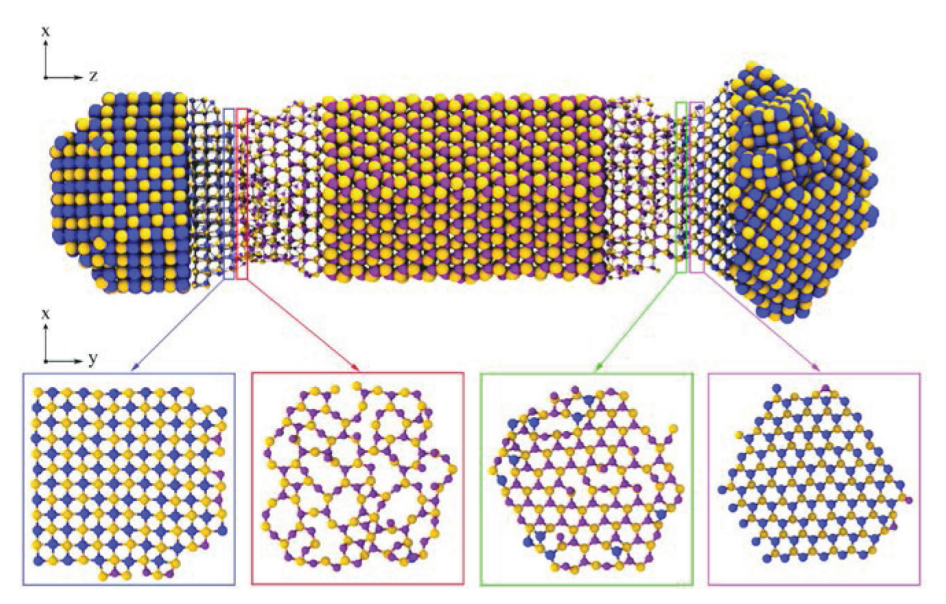


Figure C.4. Details of the PbSe/CdSe interfaces for model 3, shown in Figure 5.4a-c. The yellow, purple, and blue spheres are Se, Cd, and Pb atoms, respectively. Bottom: planar views of the first (001) PbSe bilayers, and the first (0001)CdSe bilayers at the interfaces. The first (0001)CdSe bilayers contain vacancies, which likely enhances the atomic mobility in these layers. It is clear that the number of vacancies at the non-polar/polar PbSe/CdSe interface (left-hand side) is larger than in the number of vacancies in the polar/polar PbSe/CdSe interface (right-hand side).

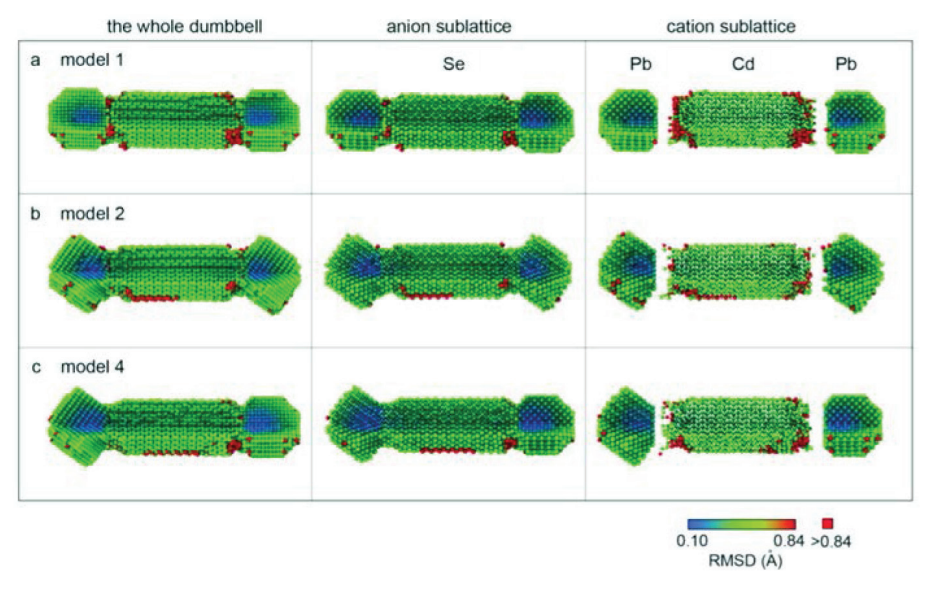


Figure C.5. (a, b and c) The map of the root-mean-squared displacement (RMSD) for each atom for the PbSe-CdSe dumbbell model 1, 2, and 4 at 500 K. The columns from left to right are the whole PbSe-CdSe dumbbells, the anion sublattices, and the cation sublattices, sequentially. The dumbbells are cut so that both of the surface and inner atoms can be seen. The pure red atoms correspond to those have a RMSD larger than 0.84 Å.

C.5 Density Functional Theory (DFT) calculations

C.5.1 Defect energy calculations in PbSe and CdSe

All calculations were carried out using the first-principles' Vienna Ab initio Simulation Program (VASP)^{22,23} employing density functional theory (DFT) within the Projector-Augmented Wave (PAW) method.²⁴ The generalized gradient approximation (GGA) formulated by Perdew, Burke, and Ernzerhof (PBE)²⁵ was employed for the exchange and correlation energy terms. The cut-off energy of the wave functions was 350.0 eV. The cut-off energy of the augmentation functions was about 500.0 eV. The electronic wave functions were sampled on a 4×4×2 grid using the Monkhorst and Pack method with 8 to 20 k-points depending on different symmetries of super-cells (108 atoms). Structural optimizations were performed for both lattice parameters and coordinates of atoms. Different k-meshes and cut-off energies for waves were tested to have a good convergence (< 2 meV/atom).

In order to have a better comparison and to exclude the differences of configurational entropies caused by different cell-sizes and number of atoms, the FCC lattice of WZ PbSe was transferred into a hexagonal cell with the relationships: $a_h = 3/\sqrt{2} \ a_c$, $c_h = 2\sqrt{3} \ a_c$, here $(a_c$ is the lattice parameter of the cubic face, a_h , c_h are the lattice parameters of the hexagonal cells). In this way, one hexagonal super-cell (from FCC lattice) contains 54 Pb and 54 Se atoms, with dimensions of $3a_h \times 3a_h \times 2c_h$. A super-cell for the HCP CdSe cell is built by $a_h^* = 3 a_h$, $c_h = 3 a_c$, which contains the same amounts of Cd and Se atoms but in a different order of stacking. Point defects including Schottky defects, Frenkel defects, and the substitutional Pb-Cd defect were considered in this study. If there were two point defects in the supercell, the defect sites were placed as far as possible from each other within the supercell, in order to avoid artificial interaction between the defect sites.

The Schottky defect is composed of one cation vacancy and one anion vacancy. We calculated two configurations: the Schottky dimer and Schottky pair. In the dimer, the cation vacancy and the anion vacancy are occupying adjacent lattice sites: the two vacancies are bound. In the Schottky pair, the two vacancy species are separated (as much as possible within the periodic supercell). The formation energy is defined as

$$E_f = E(M_{53}Se_{53}) - \frac{53}{54}E(M_{54}Se_{54})$$
 (C.2)

Here, the perfect cell is used as the reference phase.

A Frenkel defect is a defect whereby one atom has left its lattice site in the cell, therefore it consists of one vacancy and one interstitial of the same atomic species. Both cation and anion Frenkel defects are included. The formula for the Frenkel defect formation energy is:

$$E_f = E(M_{54}Se_{54})_{Frenkel} - E(M_{54}Se_{54})_{Perfect}$$
 (C.3)

which is simply the energy difference between the defective cell and the perfect cell.

The (Cd,Pb) substitutional defect energy is the energy required to swap a Pb atom with a Cd atom; the Cd atom occupies a Pb site in the PbSe lattice and the Pb atom occupies a Cd site in the CdSe lattice. The formation energy is defined with respect to the perfect CdSe and PbSe supercells as follows:

$$E_f = E(Cd_{53}PbSe_{54}) + E(CdPb_{53}Se_{54}) - [E(Cd_{54}Se_{54}) + E(Pb_{54}Se_{54})] \quad (C.4)$$

with $E(Cd_{53}PbSe_{54})$ and $E(CdPb_{53}Se_{54})$ the energy of super-cells containing one substituted cation atom, and $E(Cd_{54}Se_{54})$ and $E(Pb_{54}Se_{54})$ the energy of perfect super-cells. The results are shown in Table C.5.

Table C.5. Defect energies (in eV) in MSe (M=Cd,Pb) calculated using DFT-GGA-PBE. A Schottky defect consists of a cation vacancy and an anion vacancy, while a Frenkel defect consists of a vacancy and an interstitial atom of the same species.

Defect		Formation energy $E_{ m defect}$ (eV)		
		CdSe	PbSe	
Schottky pair	$V_M + V_{Se}$	4.82	1.52	
Schottky dimer	$\{V_{M}V_{Se}\}$	2.02	1.24	
Frenkel cation	$V_M + M^i$	3.16	3.30	
Frenkel anion	$V_{Se} + Se^{i}$	6.00	3.80	
Substitutional cation	$[Cd]_{Pb}+[Pb]_{Cd}$	0.	98	

From Table C.5, it becomes clear that PbSe is a typical Schottky material, as the Schottky defect energies are much lower than the Frenkel defect energies. Consequently, only vacancies, and no interstitial atoms will be present. In CdSe, the lowest defect energy is for the Schottky dimer, however the dimer is likely not mobile and will therefore not participate in the cation exchange. The second-lowest energy is that of the Cd Frenkel defect (Cd vacancy and Cd interstitial). As the "Cd interstitial" evaporates into the vacuum, the Cd vacancy is left behind and is then available to mediate the cation exchange, as depicted schematically in Figure C.1.

Finally we would like to make a few remarks on the interpretation of the defect energy calculations. The defect energies listed in Table C.5 are for defects in bulk CdSe and PbSe at thermal equilibrium. The absolute values of the defect energies in Table C.5 are rather high. The equilibrium atomic concentration of defects can be evaluated as $f_{\text{defect}} = \exp(-E_{\text{defect}}/k_{\text{B}}T)$ where k_{B} is the Boltzmann constant and T is the temperature in K. Therefore, a defect energy of 1.24 eV for the Schottky dimer in PbSe leads to an atomic fraction of $f_{\text{VPbSe}} = 7.1 \times 10^{-15}$ at a temperature of 443 K. Considering that the number of atoms in the nanodumbbells is approximately 30000, thermodynamically the number of vacancies to be expected is zero. It is clear also from the high mobility of the Cd atoms near the interface shown in Figure 5.4 that bulk defect calculations cannot be directly applied to nanoscale materials with surfaces and interfaces: the formation energies of defects at surfaces and interfaces is apparently an order of magnitude lower than in the bulk.

C.5.2 Energies of PbSe-CdSe mixed phases

In order to investigate the energetics of mixing into more detail, the DFT-PAW-GGA-PBE approach as implemented in the VASP code²²⁻²⁵ was also applied to mixed PbSe-CdSe phases. The formation energy (for a temperature of 0 K and a pressure of 0 Pa) was defined with respect to the lowest-energy phases: RS PbSe and WZ CdSe as:

$$\Delta E\{Pb_xCd_{1-x}Se\}_{RS/WZ} = E\{Pb_xCd_{1-x}Se\}_{RS/WZ} - xE\{PbSe\}_{RS} - (1-x)E\{CdSe\}_{WZ} \quad (C.5)$$

Here ΔE and E are expressed in eV per formula unit, while x is the atomic fraction of Pb atoms amongst the cations. The result for 0 K is shown in Figure C.6. At this temperature, all formation energies are positive, indicating complete phase separation.

At elevated temperatures, configurational entropy becomes a contributing term in the Gibbs free energy. The $(Cd_{1-x}Pb_x)$ Se phases can be considered as an CdPb alloy on the metal sublattice. For a random model the configurational entropy is $S = -k_B\{x\ln(x) + (1-x)\ln(1-x)\}$, where k_B is the Boltzmann constant. The Gibbs free energy G(T) at p=0 Pa for $(Cd_{1-x}Pb_x)$ Se is then evaluated as

$$G(T) = E(0) - TS = E(0) + Tk_B\{xln(x) + (1-x)ln(1-x)\}$$
 (C.6)

where E(0) is the formation energy at 0 K. For temperatures up to 500 K, the contribution of TS to the Gibbs free energy is always less than 0.03 eV (of the order of kT) and does not change the characteristics of the relative stability shown in Figure C.6.

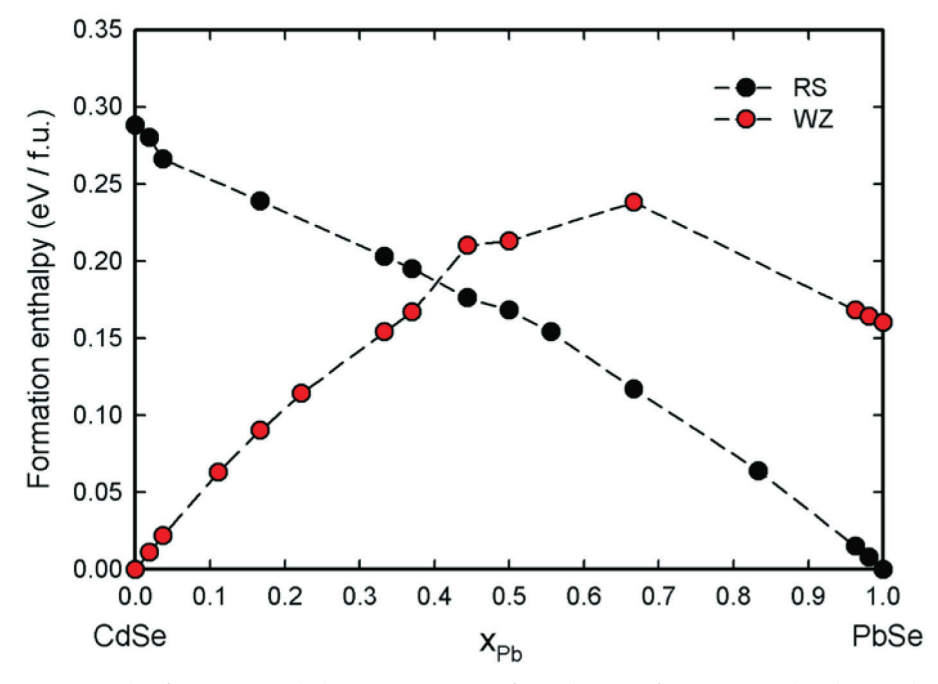


Figure C.6. The formation enthalpy ΔE (meV per formula unit) for various $(Pb_xCd_{1-x})Se$ phases. Red circles show the energies of the WZ-based structures, black spheres the energies of the RS-based structures. Lines are drawn to guide the eye.

From Figure C.6 it follows that below a Pb cation concentration of 40 at.%, the WZ phase is favored, while above that concentration the RS phase is favored. However, because formation enthalpy is positive for the entire compositional range (not only at 0 K but also for temperatures up to 500 K), mixing is not favorable and phase separation into RS PbSe and WZ CdSe will always occur. This is in good agreement with the MD simulations (Figure 5.4, C.3-C.5) and with the experiments, where only a low degree of mixing was observed (Table C.1).

Table C.6. Calculated results for ternary (Cd_{1.x}Pb_x)Se phases using DFT-GGA approach. The lattice parameters and formation energy ΔE are calculated for a range of compositions with of values of the Pb cation concentration $0 \le x \le 1$, both for the rock salt (RS) phase and the wurtzite (WZ) phase.

RS			WZ				
x	a (Å)	E (eV/f.u.)	ΔE (eV/f.u.)	a / c (Å)	cla	E (eV/f.u.)	ΔE (eV/f.u.)
0.00	5.736	-5.361	+0.288	4.381 / 7.155	1.633	-5.651	0.00
0.0185	5.744	-5.418	+0.280	4.390 / 7.169	1.633	-5.688	+0.011
0.0370	5.771	-5.480	+0.266	4.402 / 7.182	1.632	-5.723	+0.022
0.1111	-	-	-	4.429 / 7.249	1.637	-5.873	+0.063
0.1667	5.830	-5.839	+0.239	4.464 / 7.262	1.637	-5.988	+0.090
0.2222	-	-	-	4.517 / 7.203	1.595	-6.106	+0.114
0.3333	5.893	-6.302	+0.203	4.566 / 7.224	1.582	-6.351	+ 0.154
0.3704	5.915	-6.402	+0.195	4.581 / 7.267	1.586	-6.433	+0.167
0.4444	5.956	-6.614	+0.176	4.611 / 7.178	1.557	-6.581	+0.210
0.5000	5.979	-6.774	+0.168	4.597 / 7.146	1.554	-6.840	+0.213
0.5556	6.003	-6.921	+0.154				
0.6667	6.066	-7.243	+0.117	4.844 / 7.242	1.495	-7.122	+0.238
0.8333	6.134	-7.723	+0.064				
0.9630	6.188	-8.104	+0.015	5.201 / 6.227	1.197^{a}	-7.951	+0.168
0.9815	6.197	-8.159	+0.008	5.191 / 6.231	1.200a	-8.003	+0.164
1.000	6.206	-8.214	0.000	5.212 / 6.233	1.196ª	-8.054	+0.160

^a Relaxation into a metastable structure wherein the atoms have 5-fold coordination.

References

- 1 Gur, I.; Fromer, N. A.; Geier, M. L.; Alivisatos, A. P. Science 2005, 310, 462-465.
- Peng, Z. A.; Peng, X. J. Am. Chem. Soc. 2002, 124, 3343-3353.
- 3 Kudera, S.; Carbone, L.; Casula, M. F.; Cingolani, R.; Falqui, A.; Snoeck, E.; Parak, W. J.; Manna, L. *Nano Lett.* 2005, 5, 445-449.
- 4 Carbone, L.; Kudera, S.; Giannini, C.; Ciccarella, G.; Cingolani, R.; Cozzoli P. D.; Manna, L. J. Mater. Chem. 2006, 16, 3952-3956.
- 5 Rabani, E. J. Chem. Phys. 2002, 116, 258.
- 6 Tsuneyuki, S.; Tsukada, M.; Aoki, H.; Matsui, Y. Phys. Rev. Lett. 1988, 61, 869.
- 7 Schapotschnikow, P.; van Huis, M. A.; Zandbergen, H. W.; Vanmaekelbergh, D.; Vlugt, T. J. H. Nano Lett. 2010, 10, 3966-3971.
- 8 Bader, R. F. W. Atoms in Molecules A Quantum Theory; Oxford University Press: Oxford, 1990.
- 9 Ewald P. P. Ann. Phys. 1921, 369, 253-287.
- 10 Gale, J. D.; Rohl, A. L. Mol. Simul. 2003, 29, 291-341.
- 11 Sadao, A. Properties of Group-IV, III-V and II-VI Semiconductors; Wiley: New York, 2005.
- 12 Yu, W. C.; Gielisse, P. J. Mater. Res. Bull. 1971, 6, 621-638.
- 13 Yoshiasa, A.; Koto, K.; Maeda, H.; Ishii, T. Jpn. J. Appl. Phys. 1997, 36, 781-784.
- Sarasamak, K.; Limpijumnong, S.; Lambrecht, W. R. L. Phys. Rev. B 2010, 82, 035201.
- 15 Deligoz, E.; Colakoglu, K.; Ciftci, Y. *Physica B* 2006, 373, 124-130.
- 16 Sarasamak, K.; Kulkarni, A. I.; Zhou, M.; Limpijumnong, S. Phys. Rev. B 2008, 77, 024104.
- 17 Landolt-Börnstein, Semiconductors, Group IV Elements, IV-IV and III-V Compounds. Landolt-Börnstein, New Series, 41; Springer: Berlin, 2005.
- Ovsyannikov, S. V.; Shchennikov, V. V.; Manakov, A. Y.; Likhacheva, A. Y.; Ponosov, Y. S.; Mogilenskikh, V. E.; Vokhmyanin, A. P.; Ancharov, A. I.; Skipetrov, E. P. *Phys. Status Solidi B* 2009, 246, 615-621.
- 19 Noda, Y.; Masumoto, K.; Ohba, S.; Saito, Y.; Toriumi, K.; Iwata, Y.; Shibuya, I. *Acta Cryst.* 1987, C43, 1443-1445.
- 20 Zhang, Y.; Ke, X.; Chen, C.; Yang, J.; Kent, P. R. C. Phys. Rev. B 2009, 80, 024304.
- 21 Bencherif, Y.; Boukra, A.; Zaoui, A.; Ferhat, M. Mater. Chem. Phys. 2011, 126, 707-710.
- 22 Kresse, G.; Hafner, J. Phys. Rev. B 1993, 47, 558.
- 23 Kresse, G.; Furthmüller, J. J. Comput. Mat. Sci. 1996, 6, 15-50.
- 24 Kresse, G.; Joubert, D. Phys. Rev. B 1999, 54, 1758.
- 25 Perdew, J. P.; Burke, K.; Ernzerhof, M. Phys. Rev. Lett. 1996, 77, 3865.

PUBLICATIONS

 Heat-induced transformation of CdSe–CdS–ZnS core–multishell quantum dots by Zn diffusion into inner layers

Yalcin, A.O. et al. Chem. Commun., 2015, 51, 3320-3323.

- This paper has featured as the inside front cover of the journal (*Chem. Commun.* Volume 51, Issue 16).
- This paper was given a 'Gold for Gold' voucher by the Royal Society of Chemistry (RSC), enabling this work to be published as an Open Access article.
- Atomic Resolution Monitoring of Cation Exchange in CdSe-PbSe Heteronanocrystals during Epitaxial Solid–Solid–Vapor Growth

Yalcin, A.O. et al. Nano Lett., 2014, 14, 3661-3667.

- This paper has been selected to be featured in ACS (American Chemical Society) Editors' Choice. ACS Editors' Choice articles aim to exemplify the Society's commitment to improving people's lives through the transforming power of chemistry. One new peer-reviewed research article from any ACS journal is selected to be freely available every day; the selection of these articles is based on recommendations by the scientific editors of ACS journals from around the world. The articles in ACS Editors' Choice will remain open access.
- Core–shell reconfiguration through thermal annealing in Fe_xO/CoFe₂O₄ ordered 2D nanocrystal arrays

Yalcin, A.O. et al. Nanotechnology, 2014, 25, 055601.

- This paper has appeared on the journal cover as the featured article (*Nanotechnology* Volume 25, Issue 5).
- This paper has been selected to be featured in the 'Highlights of 2014' collection of the journal, in the 'Materials: synthesis or self-assembly' list.
- A transferable force field for CdS-CdSe-PbS-PbSe solid systems

Fan, Z. et al. J. Chem. Phys., 2014, 141, 244503.

- This paper has appeared on the journal cover as the featured article (*J. Chem. Phys.* Volume 141, Issue 24).
- From Sphere to Multipod: Thermally Induced Transitions of CdSe Nanocrystals Studied by Molecular Dynamics Simulations

Fan, Z. et al. J. Am. Chem. Soc., 2013, 135, 5869-5876.

- New Ab Initio Based Pair Potential for Accurate Simulation of Phase Transitions in ZnO Wang, S. et al. J. Phys. Chem. C, 2014, 118, 11050-11061.
- Transformation of Ag Nanowires into Semiconducting AgFeS₂ Nanowires Sciacca, B. *et al. J. Am. Chem. Soc.*, 2015, 137, 4340-4343.

CONFERENCE PRESENTATIONS

- Heat-induced transformations in heteronanocrystals: From reconfiguration to a novel epitaxial solid-solid-vapor growth *Invited Speaker* at the Zing Nanocrystals Conference, Punta Cana, Dominican Republic (13-16 July 2014).
- Temperature-induced core-shell reconfiguration of Fe_xO/CoFe₂O₄ nanocrystals in ordered 2D nanocrystal arrays 18th International Microscopy Congress (IMC 2014), Prague, Czech Republic (7-12 September 2014).
- Real-time observation of in-situ cation exchange in CdSe-PbSe nanodumbbells during epitaxial solid-solid-vapor growth Dutch Microscopy Society (NVvM) 2014 Materials Science Meeting, Utrecht, The Netherlands (2 December 2014).

CONFERENCE POSTERS

- Real-time observation of in-situ cation exchange in CdSe-PbSe nanodumbbells during epitaxial solid-solid-vapor growth 18th International Microscopy Congress (IMC 2014), Prague, Czech Republic (7-12 September 2014).
- Core-shell reconfiguration through thermal annealing in Fe₂O/CoFe₂O₄ ordered 2D nanocrystal arrays Dutch Microscopy Society (NVvM) Materials Science 2013 Meeting, Utrecht, The Netherlands (19 November 2013).
- In-situ high resolution TEM study of CdSe nanorod sublimation Physics@FOM Veldhoven 2013, Veldhoven, The Netherlands (22-23 January 2013).
- *In-situ* high resolution TEM study of CdSe nanorod sublimation 15th European Microscopy Congress (EMC 2012), Manchester, United Kingdom (16-21 September 2012).

ACKNOWLEDGMENTS

If one looks at the published versions of the chapters presented in this thesis, it is not that difficult to notice that I have been very lucky that a lot of people have helped me getting over my PhD. At the beginning, we started as a project group consisting of Henny W. Zandbergen, Marijn A. van Huis, Frans D. Tichelaar, Thijs J.H. Vlugt, Zhaochuan Fan and me. Being part of this group was a big chance that they all have done everything they could to keep Fan and me on the right track. Henny gave me all the freedom to work on the systems that I wanted to work on. I was told by several previous PhDs of him that he is particularly critical in the very first written manuscript, which I believe I also experienced. This I find a useful way to teach fresh PhD candidate how to construct a manuscript in a nice manner. Besides his deep knowledge and experience in TEM, I have always felt that he wants his PhDs to do what it makes them happy. I find myself privileged to have had the chance to work with him. Having Frans involved in the project has been important for me. His help with TEM and critical input on our works as well as his friendly approach have always helped me during stressful times. I would like to thank Thijs and Fan that our experimental results have become more meaningful with their simulations. They have been very flexible to adjust the parameters in their simulations to represent the experimental conditions as much as possible. I would like to thank Thijs also for his fast replies on our manuscripts. I wanted to have Fan as my paranymph at my defence, but he is moving to Utah for his postdoc, and I wish him all the best in the future. I want to thank Marijn as the last as he has put the most effort on my works. Besides teaching me how to conduct in-situ experiments and checking manuscripts over and over, he has always been very understanding and helpful when I had difficult times with the project. I am also particularly happy to have Henny, Marijn, Frans and Thijs all in the defence committee.

During my PhD, we have had close collaborations with Debye Institute of NanoMaterials Science. I would like to thank Relinde J.A. van Dijk-Moes, Marianna Casavola, Bart de Nijs, Rik S. Koster, Wun-Fan Li, Chang-Ming Fang, Daniël Vanmaekelbergh and Alfons van Blaaderen for their input on my works. I have had the opportunity to collaborate with Bart Goris, Sara Bals and Gustaaf Van Tendeloo from EMAT, and I would like to thank them for their help in TEM. I want to thank Sara Bals and Alfons van Blaaderen also for accepting to be in my defence committee. I also want to thank Laurens D.A. Siebbeles and Joris Dik for their presence in the defence committee.

During the last four years, we have had many people at HREM group. I do not want to miss any names here, so I want to thank everyone for this nice atmosphere in the group. Marijke, thank you a lot for everything, HREM is very lucky to have you!! Frans en Jouk, bedankt voor de vertalingen van de samenvatting en de proposities naar het Nederlands.

In the third year of my PhD, I decided to join PromooD (TU Delft PhD Representatives Organization) and I have met very nice people there. Thank you all so much for our nice board dinners and the events that we have organized together.

I am also lucky to be surrounded with nice friends in the Netherlands. As they know me well, none of them will be offended that I am not mentioning any names here. I just do not want to miss out anyone. Thank you all for nice memories ©.

PromooD brought me someone and she is constantly making everything joyful for me. Sasha, having you by my side with your care and love, knowing that you just want me to be happy, I am looking forward to our new chapter in Utrecht ©.

I have been outside Turkey for more than six years now. Sometimes I feel sad that I am not spending as much time as I want with my family. You have been incredibly understanding and always supporting. There have been several particular moments that made me realize that I am missing a lot in life, like seeing Rüzgar (nephew) reading for the first time and seeing Güneş (niece) speaking. These make me question my priorities in life regularly. I always feel your love and care. Regardless of distance, part of me is always with you. Altı seneden fazladır Türkiye dışında yaşıyorum ve ailemle istediğim kadar vakit geçirememek üzücü olabiliyor. Her zaman anlayışlı ve destekleyici oldunuz. Türkiye'de olduğum anlarda hayatta bazı şeyleri ıskaladığımı görüyorum, örneğin Rüzgar'ın okuduğunu ve Güneş'in konuştuğunu ilk defa gördüğümde... Böyle anlar bana hayattaki önceliklerimi sorgulatıyor. Sevginizi hep hissediyorum ve mesafelere rağmen bir parçam hep sizinle...

CURRICULUM VITAE

Anıl Ozan Yalçın

born on December 11, 1985 in Gediz, Turkey

2011 - 2015 PhD in Applied Physics and Materials Science

> Delft University of Technology (TU Delft), The Netherlands Thesis title: "Heteronanocrystal Transformations through In-situ

Transmission Electron Microscopy".

2009 - 2011 MSc (Ir.) in Chemical Engineering

> Eindhoven University of Technology (TU/e), The Netherlands Special master's track: Polymers & Composites (Materials

Science)

Graduated with Great Appreciation.

Graduation Project: "The Pb-free Movement: Soldering for High-

Temperature Applications".

2005 - 2009 BSc in Materials Science & Engineering

> Minor Honors Degree in Chemistry Sabancı University, Istanbul, Turkey

Graduated with High Honors.

Graduation Project: "Dielectric and Thermal Characterization of Mixed Oxides Related to $La_xSr_{1-x}Ga_yMg_{1-y}O_{3-\delta}$ (LSGM) based

Solid Oxide Fuel Cell (SOFC)".

